New techniques for noble gas geochronometry and thermochronometry

Thesis by
Stephen Ellis Cox

In Partial Fulfillment of the Requirements for the
degree of
Doctor of Philosophy

CALIFORNIA INSTITUTE OF TECHNOLOGY
Pasadena, California

2017
Defended 19 December 2016

Stephen Ellis Cox
ORCID: 0000-0002-8819-887X

Acknowledgements

This dissertation is dedicated to Lindsey Margaret Hedges, 1962-2016. Lindsey's tireless work in support of isotope geochemistry at Caltech, her penchant for dry humor, and her ubiquitous presence in the halls of the Geological and Planetary Sciences division are sorely missed.

I thank my parents, John and Janet Cox, and my sister, Angela Cox, for their continued love, patience, and support as I have pursued a PhD to the detriment of many other obligations. I thank my grandfather, Joe Cox, for inspiring and encouraging me to take the academic path. And I thank Anna Maria Montes for daily love, coffee, and company as I have worked to complete this undertaking.

I thank my advisor, Ken Farley, for trusting me to take apart important things in the lab to learn how they work, for collaborating on this work and helping me keep my head above the trees, for encouraging me to pursue interesting projects

rather than easy ones, and for providing the necessary political support to make instrument development possible. I thank Don Burnett for teaching me things about nuclear chemistry that almost no one else remembers, and for always making time to explain them to me again. I thank George Rossman for serving as my academic advisor and for reminding me of the importance of coursework. I thank John Eiler for valuable consultation both as a member of my committee and as a fount of knowledge about the history and practice of isotope geochemistry.

In addition to my committee, I thank the faculty at Caltech, in the GPS division and elsewhere, and I thank the Caltech staff for keeping the institute running. Specifically, I thank Heather Steele, Janice Grancich, Marcia Hudson, Dian Buchness, Liz Boyd, Kim Klotz, and Julie Lee in the GPS division.

I also thank Sidney Hemming and the faculty, staff, and students at Columbia University for introducing me to geology and academic research, and Pete Reiners for early inspiration in my noble gas geochemistry journey. Finally, I thank my many friends at Caltech, in Los Angeles, and in the other cities where I have lived for support, encouragement, and inspiration over the years.

Abstract

Noble gases were among the first species measured by mass spectrometry and interrogated for geochemical information about the solid Earth. The analytical challenge of measuring them has driven technological development in the field, and new applications have in turn followed from new developments. In the first chapter, I present developments that bolster an existing technique, the (U–Th)/Ne system, by verifying the theoretical underpinnings of the method and by exploring its application in several minerals. In the second chapter, I show that the hematite (U–Th)/Ne system is a sound geochronometer for use in the upper crust and a potent thermochronometer for exploring mid-crustal processes. In the third chapter I show significant advances toward using a quadrupole ion trap as a noble gas mass spectrometer, including the first static vacuum measurements. This technique provides new opportunities for low abundance noble gas measurements through its ultra low dark noise time of flight measurement approach and its high resolution, high mass range scanning capabilities. The quadrupole ion trap can measure lower concentrations of rare species like ^{3}He and ^{21}Ne on Earth, allowing us to make more precise determinations of cosmogenic exposure ages, and it can measure species with much higher resolution than is currently possible on most spaceflight instruments, allowing us to perform measurements on planetary surfaces and in deep space that are currently reserved to terrestrial laboratories. Finally, in the fourth chapter I demonstrate that an old, largely abandoned technique, (U–Th)/He geochronometry, has useful applications now that we fully understand its limitations.

Published Content and Contributions

Cox, S. E., K. A. Farley, and D. J. Cherniak (2015). "Direct measurement of neon production rates by (α,n) reactions in minerals". In: *Geochimica et Cosmochimica Acta* 148, pp. 130–144. DOI: 10.1016/j.gca.2014.08.036.
S.E.C. designed the research project, participated in ion implantation, performed laboratory measurements, and wrote the manuscript.

Cox, S., K. Farley, and S. Hemming (2012). "Insights into the age of the Mono Lake Excursion and magmatic crystal residence time from (U-Th)/He and ^{230}Th dating of volcanic allanite ". In: *Earth and Planetary Science Letters* 319-320, pp. 178–184. DOI: 10.1016/j.epsl.2011.12.025.
S.E.C. designed the research project, conducting field sampling, performed laboratory measurements, and wrote the manuscript.

Table of Contents

Acknowledgements . . . iii
Abstract . . . v
Published Content and Contributions . . . vi
Table of Contents . . . vii
List of Illustrations . . . x
List of Tables . . . xii
Chapter I: Direct Measurement of Neon Production Rates by (α,n) Reactions in Minerals . . . 1
1.1 Introduction . . . 2
1.1.1 The production of neon by uranium and thorium decay . . . 4
1.1.2 Physical quantities used to predict neon production rates . . . 10
1.1.3 Neon-21 production rates measured by alpha particle implantation . . . 13
1.1.4 A natural test of the ^{21}Ne production rate and preliminary ^{22}Ne production rate from Durango apatite . . . 14
1.1.5 Samarium-147 and cosmogenic neon . . . 15
1.2 Experimental . . . 16
1.2.1 Sample selection and preparation . . . 16
1.2.2 Alpha particle implantation . . . 17
1.2.3 Neon . . . 18
1.2.3.1 Neon mass spectrometry . . . 18
1.2.3.2 Neon-21 measurement by isotope dilution and sample–standard bracketing . . . 20
1.2.4 Helium . . . 22
1.3 Results . . . 24
1.3.1 Neon and helium in synthetic targets . . . 24
1.3.2 Neon, helium, uranium, and thorium in Durango fluorapatite 26
1.4 Discussion . . . 26
1.4.1 Comparison with predicted production rates . . . 26
1.4.2 Durango fluorapatite systematics . . . 28
1.4.3 Neon production rates in other uranium- and thorium-bearing minerals based on validated cross section . . . 30
1.4.3.1 Zircon, xenotime, thorite, and coffinite . . . 31
1.4.3.2 Titanite and baddeleyite . . . 32
1.4.3.3 Uraninite, thorianite, and the implications of micro-inclusions . . . 32
1.4.3.4 Hematite, goethite, and magnetite . . . 33
1.4.3.5 Calcite and aragonite . . . 34
1.5 Conclusions . . . 34

Chapter II: Ne Diffusion in Polycrystalline Hematite and Single Crystal Corundum . . . 45
2.1 Introduction . . . 46
2.2 Samples and Methods . . . 48
2.3 Results . . . 51
2.3.1 Helium in corundum . . . 52
2.3.2 Neon in corundum . . . 53
2.3.3 Neon in hematite . . . 54
2.4 Discussion . . . 57
2.4.1 Polydomain Ne diffusion in hematite and (U–Th)/Ne geochronometry . . . 57
2.4.2 Hematite (U–Th)/Ne thermochronometry . . . 59
2.4.3 Ionic Porosity Model . . . 62
2.4.4 Comparison to computation models . . . 66
2.5 Conclusions . . . 67
Chapter III: Noble Gas Mass Spectrometry with a Quadrupole Ion Trap . . . 87
3.1 Introduction . . . 87
3.1.1 History of noble gas mass spectrometry . . . 87
3.1.2 History and future of extraterrestrial mass spectrometry . . . 91
3.1.3 History of the quadrupole ion trap . . . 93
3.1.4 Theory of operation of the quadrupole ion trap . . . 96
3.2 Hardware, calibration, and measurement schemes . . . 104
3.2.1 Mass spectrometer hardware . . . 104
3.2.1.1 Ion trap electrodes . . . 104
3.2.1.2 Ion source . . . 107
3.2.1.3 Ion detection . . . 109
3.2.1.4 Inductors . . . 110
3.2.1.5 RF electronics . . . 112
3.2.1.6 Lens, timing, and ion counting electronics . . . 116
3.2.1.7 Vacuum hardware and sample handling . . . 116
3.2.2 Control software . . . 117
3.2.2.1 Overview of JPL software . . . 117
3.2.2.2 Caltech Labview software . . . 118
3.2.3 The RF circuit . . . 121
3.2.3.1 Finding resonance . . . 122
3.2.3.2 Effects of resonance on mass spectra . . . 124
3.2.4 RF ramp structure and timing . . . 128
3.3 Demonstrated capabilities and development targets . . . 129
3.3.1 Sensitivity, background noise, Ar consumption, Ar rise rate, and mass resolution . . . 130
3.3.2 Ongoing work . . . 136
3.4 Conclusions . . . 140
Chapter IV: Insights Into the Age of the Mono Lake Excursion and Magmatic Crystal Residence Time from (U–Th)/He and ^{230}Th Dating of Volcanic Allanite . . . 144

4.1 Introduction 144
4.2 Geologic Background 146
4.2.1 The age of Ash 15 in the Wilson Creek Formation 146
4.2.2 (U–Th)/He dating of juvenile materials 148
4.2.3 Magmatic crystal residence time from ^{238}U-^{230}Th disequilibrium 150
4.3 (U–Th)/He and ^{230}Th Dating Methods 150
4.3.1 Sampling and Allanite Separation 150
4.3.2 (U–Th)/He Analysis 153
4.3.3 ^{230}Th ages of Ash 15 allanite 157
4.4 Results 159
4.4.1 Ash 15 eruption age 159
4.4.2 Allanite magma residence time 159
4.5 Discussion and Conclusions 162

List of Illustrations

Number *Page*

1.1 Calculating ^{21}Ne yield from alpha particles 9

1.2 Comparison of measured ^{21}Ne yields per alpha particle in quartz with predictions 24

1.3 Comparison of measured ^{21}Ne yields per alpha particle in barium tungstate with predictions 25

1.4 Apatite Ne concentrations 27

1.5 Relationship between age and effective uranium concentration 31

2.1 Large diffusion cell 69

2.2 He diffusion in corundum 70

2.3 Ne diffusion in corundum 71

2.4 Ne diffusion in hematite 72

2.5 ln(r/r$_0$ plot for Ne diffusion in hematite 73

2.6 Model run showing the transformation of simulated ^{3}He diffusion domains into ^{21}Ne domains 74

3.1 The Mathieu stability diagram 103

3.2 QIT photo 105

3.3 Oscilloscope trace showing a 1.404 MHz sine wave on QIT 115

3.4 The effects of resonance on the QIT mass spectrum 125

3.5 Jitter of the ^{40}Ar peak during ten seconds of analysis 127

3.6 QIT Dynamic Background 130

3.7 Sensitivity of the QIT measured on a ^{40}Ar standard 132

3.8 Mass resolution of ^{40}Ar at 1.404 MHz 134

3.9 Mass resolution of ^{4}He at 4.180 MHz 136

4.1 Ash 15 at the South Shore outcrop 151

4.2 Allanite SEM image. 152

4.3 ESEM-EDX spectrum of an allanite crystal 153

4.4 Eruption and magma crystallization ages for Ash 15 allanite 161

List of Tables

Number *Page*

1.1 Neon and helium data in implanted quartz and barium tungstate . . . 39

1.2 Neon isotope data of Durango fluorapatite 40

1.3 Helium and Ne/He data for Durango fluorapatite 41

1.4 Uranium, thorium, and (U–Th)/Ne age data for Durango fluorapatite . 42

1.5 Helium and (U–Th)/He age data for part of the third dataset 43

1.6 Calculated ^{21}Ne and ^{22}Ne production rates 44

2.1 All results from He and Ne diffusion experiments. 75

4.1 (U–Th)/He data and calculated helium eruption ages 169

4.2 ^{230}Th excess data and calculated disequilibrium crystallization ages. . 170

Chapter 1

Direct Measurement of Neon Production Rates by (α,n) Reactions in Minerals

Abstract

The production of nucleogenic neon from alpha particle capture by ^{18}O and ^{19}F offers a potential chronometer sensitive to temperatures higher than the more widely used (U–Th)/He chronometer. The accuracy depends on the cross sections and the calculated stopping power for alpha particles in the mineral being studied. Published ^{18}O(α,n)^{21}Ne production rates are in poor agreement and were calculated from contradictory cross sections, and therefore demand experimental verification. Similarly, the stopping powers for alpha particles are calculated from SRIM (Stopping Range of Ions in Matter software) based on a limited experimental dataset. To address these issues we used a particle accelerator to implant alpha particles at precisely known energies into slabs of synthetic quartz (SiO_2) and barium tungstate ($BaWO_4$) to measure ^{21}Ne production from capture by ^{18}O. Within experimental uncertainties the observed ^{21}Ne production rates compare favorably to our predictions using published cross sections and stopping powers, indicating that ages calculated using these quantities are accurate at the ~3% level. In addition, we measured the ^{22}Ne/^{21}Ne ratio and (U–Th)/He and (U–Th)/Ne ages of Durango fluorapatite, which is an important model system for this work because it contains both oxygen and fluorine. Finally, we present ^{21}Ne/^{4}He production rate ratios for a variety of minerals

of geochemical interest along with software for calculating neon production rates and (U–Th)/Ne ages.

1.1 Introduction

Alpha particles produced by the decay of uranium and thorium series nuclides interact with light elements in minerals to produce the three stable isotopes of neon. Nuclides created by such secondary nuclear reactions are termed nucleogenic, and can be produced by alpha particle capture and also by capture of neutrons emitted by alpha particle capture. Wetherill (1954) was the first to recognize production of nucleogenic neon, from (α,n), (α,p), and (n,α) reactions in minerals containing uranium and thorium. Neon produced by these reactions is also readily apparent in crustal well gases (Kennedy et al., 1990). Yatsevich and Honda (1997), who were primarily interested in the neon budget of Earth's mantle and atmosphere, proposed the use of nucleogenic neon as a chronometer. They established that the reaction $^{18}O(\alpha,n)^{21}Ne$ dominates the nucleogenic production of neon in crust and mantle, and that the reaction $^{24}Mg(n,\alpha)^{21}Ne$ is insignificant in comparison. In addition, using published neutron capture cross section measurements they arrived at a mean bulk crustal production rate ratio $^{21}Ne/^{4}He = 4.5 \times 10^{-8}$, which is consistent with current estimates and measurements for U- and Th-bearing minerals, yet is much higher than earlier estimates (Kyser and Rison, 1982). Using similar data, Leya and Wieler (1999) calculated the production rate of ^{21}Ne and ^{22}Ne in specific minerals of geochemical interest, such as apatite and zircon. Gautheron et al. (2006) modeled the production rate of $^{18}O(\alpha,n)^{21}Ne$ on the basis of a different analysis of

the published cross section data and arrived at production rates that differed by up to ∼10% from those of Leya and Wieler (1999). They also presented (U–Th)/Ne age determinations on several apatite and zircon samples using these production rates and considered the consequences for dating of the spatial separation of parent nuclides from both helium and neon daughter products due to alpha ejection and the energy dependence of the neon production rate.

The (U–Th)/Ne geochronometer is potentially useful in rapidly cooled samples and as a chronometer of the minimum age of mineral formation. In the former case, one simply assumes that the rock cooled so quickly that diffusive loss of neon has been negligible for its entire history, and in the latter case, one acknowledges that diffusive loss may have occurred and accounts for this possibility in the geologic interpretation. For example, Farley and Flowers (2012) applied (U–Th)/Ne dates as a minimum age for the formation of a hematite specimen from the Grand Canyon.

As discussed by Gautheron et al. (2006), (U–Th)/Ne ages can also be used for thermochronometry. Ideally a thorough understanding of the temperature dependence of neon diffusion supports such an application. However, because laboratory diffusivity measurements are usually made under environmental conditions (temperature, pressure, chemical activity) much different from the natural setting, care is required in interpreting the laboratory data. This is especially true for some phases of interest for (U–Th)/Ne dating, such as apatite, because phase modification via volatile loss in a high temperature vacuum chamber is possible (Nadeau et al., 1999). As an alternative approach, approximate closure temperatures for neon can

be obtained by comparison of neon ages to those of other thermochronometers in the same rock (Gautheron et al., 2006).

1.1.1 The production of neon by uranium and thorium decay

In the (U–Th)/He system, multiple parents (uranium-238, uranium-235, and thorium-232) decay through chains in which they emit a series of alpha particles with discrete energies. Samarium-147 is also an alpha emitter, but because it produces just one alpha particle and because of its very low energy, this nuclide contributes little to nucleogenic production. The vast majority of alpha particles come to rest as ^{4}He atoms, but a small number (fewer than one in ten million) react with other elements in a mineral to form nuclear reaction products. A particularly important reaction is ^{18}O(α,n)^{21}Ne, which produces measurable neon in many oxide and silicate minerals (Yatsevich and Honda, 1997; Leya and Wieler, 1999; Gautheron et al., 2006; Farley and Flowers, 2012). The reaction ^{19}F(α,n)^{22}Ne is even more productive per alpha particle, but is important only in minerals that contain significant fluorine, such as apatite, titanite, or fluorite (Solé and Pi, 2006). Although only limited data exist, all analyzed minerals are more retentive of neon than of helium (Shuster and Farley, 2005; Tournour and Shelby, 2008a; Tournour and Shelby, 2008b; Behrens, 2010; Cherniak, Thomas, et al., 2014). This suggests the possibility of using measured neon concentrations in minerals as a chronometer like (U–Th)/He, but retentive to higher temperatures (Yatsevich and Honda, 1997; Leya and Wieler, 1999; Gautheron et al., 2006). However, a known rate of neon production is critical for any chronometric application, and existing estimates based on neutron production

measurements are not in sufficient agreement for high-precision geochronology (Leya and Wieler, 1999; Gautheron et al., 2006). In this paper we take a different approach than previous workers to establishing ^{21}Ne production rates. We measure the neon itself in target phases exposed to energetic alpha particles of precisely known energy. This work is analogous to the oxygen gas target experiments of Hünemohr (1989) but undertaken on solid phases. We also present new high precision U-Th-He-Ne data on Durango apatite, which confirm the validity of our ^{21}Ne results in a natural system and also provide a production rate estimate for the ^{22}Ne reaction from alpha capture by ^{19}F.

For (U–Th)/Ne chronometry, we are primarily interested in the two reactions ^{18}O(α,n)^{21}Ne and ^{19}F(α,n)^{22}Na(β+)^{22}Ne (simplified as ^{19}F(α,n)^{22}Ne hereafter due to the insignificance of the 2.6 year ^{22}Na decay over geologic time). These reactions occur at a rate proportional to the number of alpha particles emitted and to the concentration of the target nuclide (^{18}O or ^{19}F) in the mineral. Furthermore, the rate of these reactions also depends on the cross section of the target nuclide for alpha particles and the chemical composition of the host mineral. Below, we describe the physical controls on this reaction and how they are measured or calculated in order to arrive at a nucleogenic neon production rate.

Neon isotope production from (n,α) reactions on Mg can be safely ignored for minerals that do not contain large amounts (wt. %) of Mg. For example, O is about three times as productive of neon as Mg, so these production pathways only become significant at the 1% level for Mg/O > 0.03 (in the case of ^{21}Ne). Magnesium is even

less productive of neon than F, so these production pathways become significant at the 1% level for Mg/F > 0.07 (in the case of ^{22}Ne). In minerals that include magnesium as a stoichiometric constituent, these reactions must be considered in the neon budget.

The rate of a given nuclear reaction depends on the nuclear properties of the target nuclide and the energy of the incident particle, and is characterized by the nuclear cross section parameter σ(E). The cross section is an areal representation of the probability of reaction in a pure sample of the target nuclide and is frequently described in units of millibarns (1 barn = 10^{-24} cm^2). A larger cross section means that the reaction is proportionally more likely to occur when a single particle interacts with the target, or proportionally more frequent when a large number of particles interact with the target. Over the energy range of interest here, cross sections for neon-producing alpha particle reactions generally increase with alpha energy. Cross sections for neon producing reactions have been measured over the last several decades (Bair and Willard, 1962; Hansen et al., 1967; Bair and Del Campo, 1979; Norman et al., 1984), usually using a thin-target approach in which the cross section is determined by measuring the production rate of neutrons using alpha particles at just a single energy. In contrast, nucleogenic neon production in a mineral involves reactions occurring along the entire trajectory as the alpha particle slows and eventually comes to rest, and thus involves an integral along the alpha particle energy path. These observations have three important implications: neon production will be higher for alpha particle decays with high characteristic energy;

neon production will depend on how fast alpha particles lose energy within a given mineral; and neon production will preferentially occur early in the alpha particle trajectory, where energies are highest.

Stopping power S(E) describes the rate of energy loss of a given particle as it travels through a given material. Stopping power depends on the interactions of incident particles with both the nuclei and electron clouds of the atoms in the host mineral. In practice the electronic stopping power is several orders of magnitude larger than the nuclear stopping power and dominates at energies of interest here. Relativistic effects can be ignored here because alpha particles produced by radioactive decay are well below the energy at which such effects become significant (about 35 MeV). Stopping power is represented with density-normalized units of MeV/(mg/cm^2) to avoid the requirement of measuring density in natural samples. Like the cross section, stopping power is dependent on the energy of the incident alpha particles, so it must also be considered as an integral quantity as these particles lose energy and come to rest. Many studies have measured and modeled stopping powers in great detail (e.g., SRIM and references therein; Ziegler et al. 2010).

Reaction cross section, oxygen-18 or fluorine-19 content, and stopping power of a given mineral are the basic ingredients required to predict the neon production rate from alpha-emitting radionuclides. Production is linearly proportional to the concentration of the target nuclide in the host mineral, and is proportional to an energy-dependent integral quantity that includes both the cross section and the total stopping power for alpha particles in the host mineral. We will take this integral

from rest (Eα = 0 MeV) to the energy of each alpha particle emitted during alpha decay. As an example, in the next section we construct the yield equation for ^{21}Ne from ^{18}O for a given alpha particle in a generic mineral Z.

We represent the concentration of ^{18}O in Z as the product of the mass fraction of oxygen (X_O) in the mineral and the isotopic abundance of ^{18}O (N_{18}/N_O), divided by the total atomic mass of one formula unit of the mineral (A_Z). We multiply this quantity by the Avogadro constant (N_A) to arrive at $(X_O)(N_{18}/N_O)(N_A/A_Z)$, which has units of atoms/gram.

The integral quantity that describes the rate of reaction as an alpha particle interacts with the target mineral scales with the cross section (a higher cross section means more production) and scales inversely with stopping power (a higher rate of energy loss means less neon production). As a consequence our integrand is the cross section σ(E) divided by the mineral-dependent stopping power S_Z(E). We then integrate this from rest (Eα = 0 MeV) to the energy of the incident alpha particle $E_{\alpha k}$. We arrive at the term $\int_0^{E_{\alpha k}} \frac{\sigma(E)}{S_Z(E)} dE$, which has units of (mbarn)(mg/cm2).

Finally, we multiply by 10^{-3} to convert mbarn to barn, 10^{-24} to convert barn to cm^2, and 10^{-3} again to convert mg to g, which allows us to arrive at the following complete yield equation (e.g., Yatsevich and Honda 1997): $Y_{^{21}Ne} = 10^{-30} \frac{N_A}{A_Z} X_O \frac{N_{18}}{N_O} \int_0^{E_{\alpha k}} \frac{\sigma(E)}{S_Z(E)} dE$ (1) This equation has units of atoms and reflects the production rate of neon for a single alpha particle k of initial energy Eαk. This quantity will be quite small, about 5×10^{-8}, because most alpha particles come to rest as ^{4}He without reaction.

As a concrete example, we illustrate this calculation for quartz (SiO_2) and barium tungstate ($BaWO_4$) in Figure 1.1. Figure 1.1a shows the cross section for the reaction $^{18}O(\alpha,n)^{21}Ne$ as a function of alpha particle energy, with original data points in black circles and the smoothed interpolation presented as a red line (Section 1.2), Figure 1.1b shows the stopping power for alpha particles in quartz as a function of alpha particle energy (Ziegler et al., 2010), Figure 1.1c shows the integrand $(\sigma(E))/(S_Z(E))$ as a function of alpha particle energy, and Figure 1.1d shows the full yield equation given stoichiometric $X_O = 0.5326$ and $\delta^{18}O_{VSMOW} = +2$ ‰($^{18}O/^{16}O = 0.0020052$).

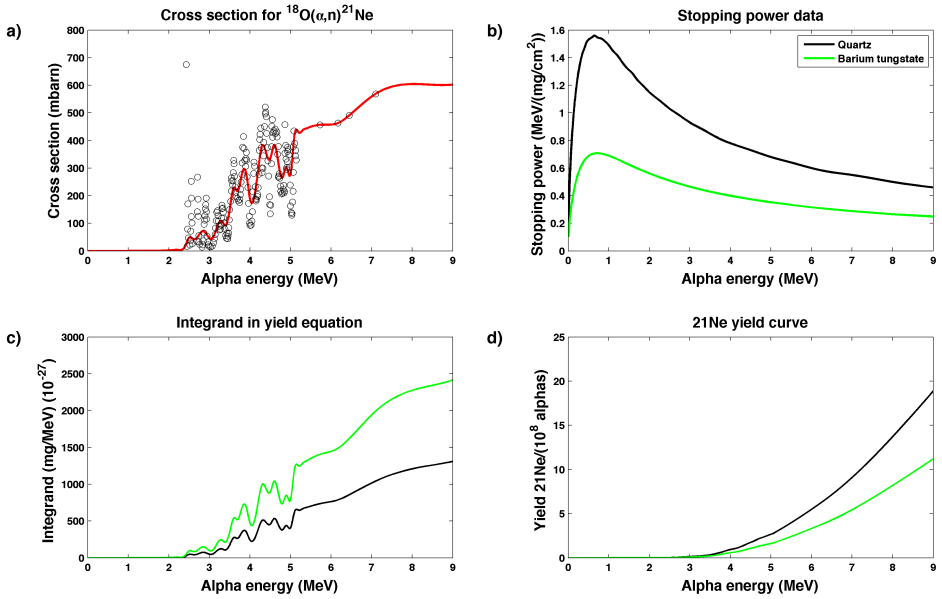

Figure 1.1: An illustration of the steps involved in calculating ^{21}Ne yield from alpha particles in quartz (SiO_2; black) and barium tungstate ($BaWO_4$; green). The figure shows a) the interpolated cross section of the reaction $^{18}O(\alpha,n)^{21}Ne$, including the renormalized (Bair and Del Campo, 1979) data of Bair and Willard (1962) and the high energy data of Hansen et al. (1967), b) the density-normalized stopping power for alpha particles in quartz and barium tungstate, c) the integrand $\sigma(E)/S_Z(E)$ from the yield equations, and d) the calculated yield for ^{21}Ne from alpha particles in quartz and barium tungstate.

The yield equation for ^{21}Ne from alpha particles in quartz (Figure 1.1d) demon-

strates several notable features. The production rate increases toward the higher energy end of the alpha energies produced by uranium and thorium decay, so these decays will dominate the total nucleogenic neon in a sample. Conversely, alpha emitters with no high-energy decays (^{147}Sm, for example) will produce negligible nucleogenic neon. In addition, because alpha particles are more productive when first emitted (at their highest energy), most nucleogenic neon will be produced closer to the alpha emitter than the final rest position of ^{4}He that does not react. This means that the alpha ejection correction for neon produced by alpha particles will be smaller than the alpha ejection correction for radiogenic helium in the same minerals (Gautheron et al., 2006).

1.1.2 Physical quantities used to predict neon production rates

For use in chronometry it is both impractical and unnecessary to measure neon production rates at many alpha energies for a large number of minerals. One may instead use a (validated) cross section and stopping powers calculated from SRIM, along with the stoichiometric oxygen concentrations and assumed or measured oxygen isotopic compositions of any mineral to calculate a neon production rate. In this section we predict ^{21}Ne production rates in synthetic materials using these methods, and then compare the prediction to our measured production rates in order to validate the cross sections and stopping powers. We chose the minerals quartz (SiO_2) and barium tungstate ($BaWO_4$) because we were able to obtain large, optically pure synthetic crystals of each and because the stopping power for alpha particles in quartz is almost twice as high as in barium tungstate, so we can easily

deconvolve the effects of cross section and stopping power on the measured neon production rates.

The concentration of ^{18}O in a mineral exhibits linear control on the production rate of neon in the reaction $^{18}O(\alpha,n)^{21}Ne$, so it is crucial to account for stoichiometric variations in oxygen composition and to note the oxygen concentration used in calculating reported (U–Th)/Ne ages. In the case of measured differences in $\delta^{18}O$ or small variations in oxygen concentration, the production rates provided here may be scaled linearly because the changes in alpha particle stopping powers will be small. The mass fraction of oxygen in mineral phases is usually known from stoichiometry, and the variations in oxygen isotopic composition measured in natural minerals are usually small compared to other uncertainties in the (U–Th)/Ne system. We measured $\delta^{18}O$ = +25‰for our synthetic barium tungstate and $\delta^{18}O$ = 0‰for our synthetic quartz using the laser fluorination method at Caltech (Eiler et al., 2000). We assume a common igneous $\delta^{18}O_{VSMOW}$ = +6‰for the other calculations presented here unless otherwise noted. The user may modify this value in the software provided in the appendix.

The $^{18}O(\alpha,n)^{21}Ne$ cross section used by Gautheron et al. (2006) is based on a critically evaluated compilation of data from several sources and includes numerous resolved resonances. The thin target experiments vary in quality and include a dataset from Bair and Willard (1962) that was later renormalized by a factor of 1.35 by Bair and Del Campo (1979) because the original thin target thicknesses were measured incorrectly. Following Gautheron et al. (2006), for our predicted ^{21}Ne

yields we use a 0.01 MeV interpolation of the renormalized (Bair and Willard, 1962) data below 5.14 MeV because it is the most detailed, and we supplement it with the more sparse data from (Hansen et al., 1967) in the energy range above 5.14 MeV (Figure 1.1a).

We also adopt the cross section curve for the $^{19}F(\alpha,n)^{22}Ne$ reaction presented by Murata et al. (2006), which is based on a small amount of very sparse experimental thin target data. As noted by Murata et al. (2006), numerous resonances were observed in this reaction below alpha energies of 3.1 MeV by Wrean and Kavanagh (2000). Although these resonances are too low energy to be important for neon production, similar features must exist in the energy range of interest (primarily 3—8 MeV, because alpha particles with higher energy are not emitted by uranium and thorium series decay, and alpha particles with lower energy produce very little neon; Figure 1.1) for (U–Th)/Ne dating as well, but have not been documented. Thus the $^{19}F(\alpha,n)^{22}Ne$ cross section should be used with more caution than the cross section for the reaction $^{18}O(\alpha,n)^{21}Ne$ owing to the sparseness of these measurements.

We computed the stopping powers of the minerals of interest using SRIM (Ziegler et al., 2010) with stoichiometries found on webmineral.com. The primary limitations of SRIM are that it depends on experimental data that can vary in quality and that it does not account for crystal structure but rather assumes an amorphous phase. However, experimental data for alpha particles are relatively plentiful, and the stopping of ions is dominated by electronic collisions that will not be greatly affected by crystal structure. Effects such as channeling in a crystal lattice can be

neglected due to very low probability and low impact on total neon production. While we suspect errors introduced to our calculations from the stopping powers from SRIM are small, our experimental measurements, involving phases with very different predicted stopping powers, allow us to assess this expectation.

The calculated neon production rates for other minerals allow users to calculate (U–Th)/Ne ages from uranium, thorium, and neon data for a wide variety of minerals of geochemical interest (Section 4.3). As explained above, oxygen concentration and stopping power both affect the production rate of nucleogenic neon in a given mineral, so the differences between minerals include both of these effects.

1.1.3 Neon-21 production rates measured by alpha particle implantation

As mentioned above, previously published ^{21}Ne production rates estimated for uranium- and thorium-containing minerals differ by up to ~10% (Leya and Wieler, 1999; Gautheron et al., 2006), which is greater than the uncertainty of most noble gas measurements. This discrepancy is sufficiently large as to preclude accurate chronometry and is primarily related to different interpretations of sparse and contradictory ^{18}O(α,n)^{21}Ne cross section data (Bair and Willard, 1962; Hansen et al., 1967; Bair and Del Campo, 1979). Note that our calculations in Section 1.1 use the same approach for establishing the ^{18}O(α,n)^{21}Ne cross section as Gautheron et al. (2006), so are not an independent estimate for comparison.

To assess the accuracy of the predicted ^{21}Ne production rates, we directly measured the rates by implanting a known fluence of alpha particles of a single energy into thick targets (i.e., mineral samples in which all alpha particles stop) of synthetic

materials and then measuring the amount of ^{21}Ne produced.

While quartz and barium tungstate are not likely to be targets of (U–Th)/Ne chronometry, they were appealing choices for several reasons. As noted above, their extreme contrast in stopping power may allow us to distinguish errors in stopping power from errors in cross section. In addition, we were able to obtain large optical grade crystals in both cases, which ensured homogeneous samples of adequate size for the experiment. We experimentally verified that the samples were free of neon and helium before performing the implantations. Measured quantities are exclusively a product of the implantation experiment.

1.1.4 A natural test of the ^{21}Ne production rate and preliminary ^{22}Ne production rate from Durango apatite

Fluorine is a challenging target for (U–Th)/Ne chronometry as it substitutes readily for hydroxyl and chlorine in many minerals and is therefore often not stoichiometric. In addition, it is more difficult to measure accurately than oxygen, e.g., by electron probe. However, the target nuclide ^{19}F is the only isotope in natural fluorine, and the cross section of neon production from ^{19}F is higher than for ^{18}O. Using Durango fluorapatite as a model system, we explored the potential use of ^{22}Ne produced by ^{19}F as an independent chronometer and as a counterpart to ^{21}Ne produced by ^{18}O in the same phase. Even with a less well-known production rate, ^{22}Ne is potentially useful as a relative chronometer (Solé and Pi, 2006) or as a target for diffusivity studies in fluorine-rich minerals, and is useful for deducing the presence of a fluorine-bearing phase (e.g., an inclusion) in a studied sample.

1.1.5 Samarium-147 and cosmogenic neon

We do not consider the impact of ^{147}Sm or of cosmogenic neon production in the calculations in this paper. These are irrelevant for our synthetic samples, in which we control the sole production pathway for neon, but they might be relevant in Durango fluorapatite and other natural minerals that contain significant rare earth elements and/or that have been exposed to cosmic radiation. However, ^{147}Sm emits a single alpha particle with energy of only 2.23 MeV. The neon production rate at this energy is negligible due to the extremely low cross section for the reactions ^{18}O(α,n)^{21}Ne and ^{19}F(α,n)^{22}Ne in this energy range (Figure 1.1; Wrean and Kavanagh 2000).

Cosmogenic neon dating has applications to many surface processes, especially to ancient surfaces that cannot be dated as effectively using radioactive nuclides such as ^{10}Be. Durango fluorapatite is mined from below the surface, so it should be free of this component, but cosmogenic neon is a potential contaminant for samples that have been exposed within ~1 m of Earth's surface for a substantial period of time, so it should be considered during sampling and in cases for which the rock history is unknown. Production rates of cosmogenic neon are mineral-dependent, but are typically of the order of a few tens of atoms per gram per year. Cosmogenic neon is produced with a distinctive isotope ratio (mineral-dependent, but roughly subequal in all three isotopes; Niedermann 2002) compared to air and nucleogenic neon, so one can usually recognize it by analyzing all three neon isotopes. When helium is also analyzed, the presence of ^{3}He can be an indicator of cosmogenic nuclide contamination.

1.2 Experimental

1.2.1 Sample selection and preparation

We prepared ~1 cm square and ~1 mm-thick slabs of quartz and barium tungstate by cutting with a wire saw and cleaning in an ultrasonic bath of 18.2 MΩ purified water to ensure that no residue from the cutting slurry was present. These samples are far thicker than the average stopping distance for alpha particles in either mineral (~15–30 μm depending on energy) and therefore represent thick targets that effectively stop all incident alpha particles.

The quartz and barium tungstate analyzed in this study had low concentrations of non-nucleogenic (air-like) neon, with nucleogenic neon typically representing >85% of the measured ^{21}Ne. In minerals that tend to release more air neon, such as hematite (Farley and Flowers, 2012), the uncertainty is often limited by the correction for air contamination, which effectively raises the background level against which the nucleogenic neon signal must be resolved. Finally, the presence of non-atmospheric neon from mantle or crustal fluid sources could complicate nucleogenic neon measurements, and should be considered in the case of measured isotope ratios that do not fall on an air–nucleogenic mixing line.

We prepared the Durango fluorapatite samples from crushed and homogenized aliquots of a single gem-quality crystal such as the ones used for (U–Th)/He development (Farley, 2000). The crushing and homogenization procedure ensures that the uranium, thorium, neon, and helium distributions are homogenous between samples even though the large crystal may have uranium and thorium zonation as

reported by Boyce and Hodges (2005).

1.2.2 Alpha particle implantation

We implanted alpha particles using the 4 MV Dynamitron linear accelerator at SUNY-Albany. In order to produce alpha particles with energies in the range of approximately 4–8 MeV, which is the range encountered in the decay chains of ^{238}U, ^{235}U, and ^{232}Th, we used doubly charged particles accelerated at 2–4 MV. Using the calculations described in Section 1, we chose the alpha particle fluence for each energy by calculating the fluence necessary to achieve an easily measurable quantity of neon. The alpha particle fluence we used ranged from $\sim 10^{14}$ particles for the highest energy (most productive) experiments to $\sim 10^{15}$ particles for the lowest energy experiments.

We identified the helium beam produced by the Dynamitron using the spectra of backscattered particles from a synthetic silica slab, which produce a characteristic spectrum of backscattered alpha particles in measurements with a solid-state surface barrier detector. After focusing the beam, we placed the synthetic target (either quartz or barium tungstate) in the path of the incident beam and then measured accumulated charge in order to achieve the desired alpha particle fluence. Spectra of backscattered particles from each sample during the implantations were also monitored and collected with a solid-state surface barrier detector to ensure that only an alpha particle beam was implanted into samples during the experiments. We also monitored the shape and position of the incident beam during each experiment to ensure complete collection of beam on the targets. The Dynamitron has an energy

resolution (ΔE/E) of about 10^{-4}. The nominal uncertainty of this measurement is quite low (better than 1 ppm), but the practical uncertainty is limited to about 2% by the purity of the helium beam (Section 9.2.4).

At energies above 7 MeV, we experienced problems with beam stability and associated inadvertent implantation of hydrogen along with the helium beam. This hydrogen does not produce neon, but is included in the integrated beam current measurement along with the helium. During the implantation, a solid-state surface barrier detector set at 167.5 degrees with respect to the incident beam was used to monitor the beam, and assess whether there was any contamination of the incident helium beam by hydrogen. This could be evaluated by observation of changes in the backscatter signal if the spectra included features characteristic of hydrogen backscattered from the elemental constituents of the sample, along with spectra produced by the backscattered helium.

1.2.3 Neon

1.2.3.1 Neon mass spectrometry

We measured neon using a GV Helix SFT static vacuum magnetic sector noble gas mass spectrometer with a Balzers SEV-217 ion counting multiplier and a mass resolution (R) of approximately 800 (m/Δm, Δm = peak width at 5% of maximum peak height). To extract neon from the samples, we first degassed them in a double vacuum furnace at temperatures of 1100–1300°C, and then removed other gases using non-evaporable getters, a liquid nitrogen cryogenic trap, and a focusing cryostat. We isolated neon on a cryostat at 21K and then pumped away helium to

avoid detrimental effects of many orders of magnitude more helium than neon in the mass spectrometer. Some helium is retained at this nominal temperature on our cryostat, but we observe that the majority is removed. Neon-21 beams were several hundred counts per second (cps), well above multiplier backgrounds of ~0.15 cps and procedural blanks of ~3 cps. We measured each neon isotope beam on the multiplier by peak hopping with the accelerating voltage at a fixed magnetic field to avoid hysteresis effects and settling delays. Between analyses, we measured air standards in the same way as the samples to keep track of mass discrimination and sensitivity in the mass spectrometer. We use isotopic deconvolution and the measured composition of air standards to remove air backgrounds from samples. We are able to pseudo-resolve doubly charged ^{40}Ar from ^{20}Ne (R = 1777 for $^{40}Ar^{++}$ and $^{20}Ne^{+}$, ~45% resolved, isobar contribution less than 1‰at measurement position on ^{20}Ne) adequately enough to measure ^{20}Ne without significant interference when argon concentrations are controlled with the liquid nitrogen cryogenic trap. Doubly-charged carbon dioxide overlaps almost completely with ^{22}Ne (R = 6229), but we reduce its small contribution significantly by lowering the electron energy in the ionization source for ^{22}Ne measurement only, which reduces double ionization of carbon dioxide far more than the single ionization of neon. Carbon dioxide backgrounds are stable and less than 5‰ of ^{22}Ne signals, and we remove any carbon dioxide with the two steps of cryogenic separation.

1.2.3.2 Neon-21 measurement by isotope dilution and sample–standard bracketing

We made ^{21}Ne measurements by isotope dilution using a spike gas artificially enriched in ^{22}Ne relative to air and to the samples to ensure that pumping away the helium does not affect the neon concentration determinations. Our apparatus and spike gas for this application changed over the course of the experiments described here.

The measured isotopic composition of our first spike gas was approximately 8.9% ^{20}Ne, 0.12% ^{21}Ne, and 91% ^{22}Ne. The improved spike was of >99.5% pure ^{22}Ne. This gas is introduced into the vacuum line just after completion of the neon extraction in the furnace. After spiking, the measured mixture comprises an extraction line background including isobaric interferences, air contamination in the samples and vacuum system, the sample gas, and the spike gas. We measured the spike composition separately and, after subtracting the extraction line background from all other measurements, completely resolve the three components by matrix inversion using the three isotope measurements. The sample concentrations were determined by comparing spiked sample isotope ratios to spiked manometrically calibrated air standards.

The presence of measurable ^{20}Ne and ^{21}Ne in the first spike added to experimental error on both air corrections and ^{21}Ne determinations. In addition, we discovered a problem with the hardware (a virtual leak in the pipette volume) that led to spurious amounts of spike being emitted during a small number of experiments. Fortunately,

this problem was easily detected in ^{22}Ne measurements, and could be corrected by using the ^{22}Ne excess to determine how much extra spike we added. However, this method relies on consistent sample–standard measurements and therefore defeats the purpose of using isotope dilution. For this reason, we simply subtract spike and air contamination ^{21}Ne based on the ^{22}Ne and ^{20}Ne measurements for these few samples and present results using conventional sample–standard bracketing to determine absolute abundance. For the vast majority of samples, sample–standard bracketing and isotope dilution yielded statistically indistinguishable results, which confirms that our procedure for pumping away helium does not remove or fractionate neon. In our final results, we report isotope dilution results except when spiking problems suggest the use of the sample–standard bracketing results.

We made the Durango fluorapatite measurements using both sample–standard bracketing and isotope dilution after we redesigned our isotope dilution hardware and spike gas, which allows us to introduce a manometrically calibrated aliquot of the >99.5% pure ^{22}Ne that is repeatable to better than 0.1%. We made the first set of measurements without the addition of spike gas to characterize the isotopic composition of the neon from the fluorapatite; we then made the second set of measurements using the same method as used for the implantation measurements, but we compared the sample concentrations directly to the calibrated spike instead of using sample–standard bracketing.

The analytical uncertainties of neon measurements are about 1.5% (2σ) with isotope dilution, dominated by counting statistics and gas standard calibration, and

typically about 2% without isotope dilution. For the two samples that required a significant correction to the sample–standard bracketing result due to the problem with the isotope dilution apparatus, the uncertainty is about 4%. The higher uncertainty of the latter is primarily due to the correction for the added spike, which we calculated using its isotopic composition. We increased the stated uncertainties of these samples to encompass the results from both methods, so some data points have asymmetric uncertainties.

1.2.4 Helium

For approximately half of the implanted samples we measured for neon, we used the integrated implantation current as the measure of the alpha particle fluence. After it became apparent that two high-energy samples were unusually poor in neon compared to the expected production rate, we began to suspect that hydrogen had been implanted with helium at the highest energies. In addition, in the quartz target at 7.8 MeV, two replicate runs showed evidence of significant hydrogen contamination in the RBS spectra obtained during implantation (see Section 2.2). As a consequence, we then switched to a method that allowed us to split a very small amount of the sample helium and then measure it on a separate mass spectrometer. A split was required because the full sample of implanted helium is several orders of magnitude larger than we can measure. Measuring helium directly allowed us to determine correct neon/helium ratios even in the samples for which the alpha particle beam instability of the Dynamitron resulted in a significant implantation of hydrogen along with the alpha particles.

We isolated 0.18% of each helium sample in a small volume after gas extraction, then analyzed this gas on an MAP 215-50 static vacuum magnetic sector noble gas mass spectrometer connected to the same extraction system as the GV Helix SFT used to measure neon. This split represents an insignificant amount of the neon sample but, due to the $\sim 5 \times 10^{-8}$ production rate ratio of ^{21}Ne to alpha particles, contained enough helium to achieve a signal of tens to hundreds of mV on a Faraday cup detector equipped with an amplifier with a 10^{11} Ω resistor. We analyzed gas standards using the same split volume, so that uncertainties in the volume ratio are removed from the calculated helium concentrations. We performed all helium analyses by sample–standard bracketing with a helium-doped air standard developed at Caltech ("Caltech air"). Blank corrections for helium were insignificant.

The uncertainties on helium measurements are about 1%, and are dominated by gas standard calibration. We assigned a 2% uncertainty to helium concentrations calculated from the integrated beam current on the Dynamitron rather than measured directly. The nominal uncertainty of the implantation is far smaller (of order ppm), so this value is somewhat arbitrary and is meant to account for the typical observed scatter between the measured helium concentrations and the integrated beam currents in samples that show no evidence of hydrogen contamination. We assume that this added uncertainty is dominated by small amounts of contamination of the beam with hydrogen, and by measurement uncertainty on the mass spectrometer.

1.3 Results

1.3.1 Neon and helium in synthetic targets

Neon and helium measurements and $^{21}Ne/^{4}He$ ratios in the synthetic quartz and barium tungstate targets are shown in Table 1. Nucleogenic $^{21}Ne/^{4}He$ ratios are displayed in Figure 1.2 for quartz and Figure 1.3 for barium tungstate.

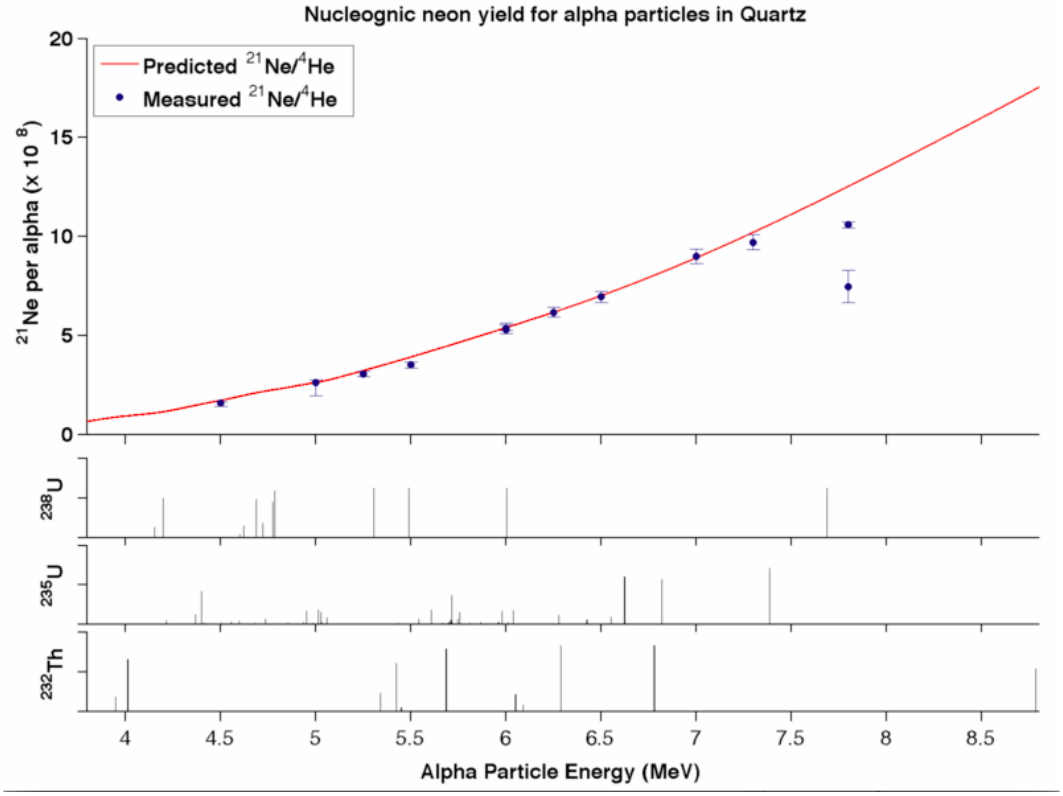

Figure 1.2: Comparison of measured ^{21}Ne yields per alpha particle in quartz with predictions based on the published cross sections of Gautheron et al. (2006) and stopping powers described in Section 1.2. The measured values at 7.8 MeV are internally inconsistent and probably represent uncorrected contamination of the alpha particle beam with hydrogen. Also shown are the relative distributions of alpha particle energies in each of the uranium and thorium decay chains.

The ^{21}Ne concentrations are between 8 and 19 million atoms in each sample. For the samples in which it was directly measured, ^{4}He concentrations range from $140x10^{12}$ to $1163x10^{12}$ atoms. With two exceptions, these numbers agreed with

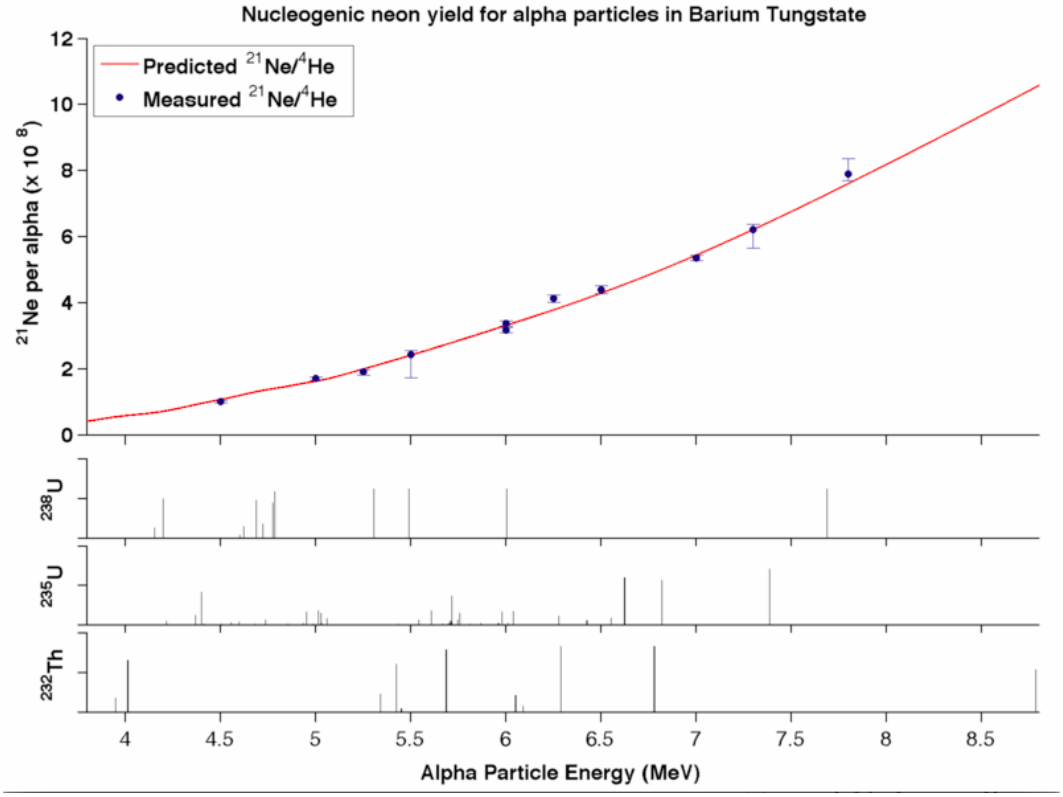

Figure 1.3: Comparison of measured ^{21}Ne yields per alpha particle in barium tungstate with predictions based on the published cross sections of Gautheron et al. (2006) and stopping powers described in Section 1.2. Also shown are the relative distributions of alpha particle energies in each of the uranium and thorium decay chains.

the total measured beam current. As expected, in both targets the ^{21}Ne/^{4}He ratios increase monotonically with alpha particle energy. The only exceptions are the two data points at Eα = 7.8 MeV in quartz (Figure 1.2); these are the samples with a large amount of contamination of the beam with hydrogen, prompting the use of the helium measurement method. The total span in production rate ratio is 1.58x10^{-8} to 1.06x10^{-7} in quartz and 1.02x10^{-8} to 7.89x10^{-8} in barium tungstate. At a given energy the production rates are higher in quartz than barium tungstate. All of these observations are in accord with predictions outlined in Section 1.2.

1.3.2 Neon, helium, uranium, and thorium in Durango fluorapatite

Three sets of experiments were done on splits of the Durango fluorapatite sample. In the first and third sets helium and neon were measured by peak height comparison while in the second set helium was measured by peak height comparison but neon was measured by isotope dilution (Tables 2 and 3). We used the measured ^{21}Ne/^{22}Ne ratio in the unspiked data set for the isotope dilution calculations (Table 2). These samples used our improved isotope dilution apparatus. All neon measurements are shown together in Figure 1.4. Finally, Table 4 shows uranium and thorium measurements made by solution ICP-MS using isotope dilution on splits of the same crushed sample of Durango fluorapatite following the procedures outlined in House and Farley (2000), and Table 5 shows (U–Th)/He age determinations on a subset of samples measured with a larger helium split for increased accuracy. Because of the significant correction for nucleogenic ^{22}Ne in fluorine-rich Durango fluorapatite, we observed no improvement in precision by switching to isotope dilution.

1.4 Discussion

1.4.1 Comparison with predicted production rates

We observed good agreement (typically <3% difference) between measured ^{21}Ne/^{4}He production rate ratios and the values predicted from the cross section data compiled in Gautheron et al. (2006) for quartz and barium tungstate. In contrast, we observed poor agreement when using the Leya and Wieler (1999) values (up to ~10% difference). The agreement for both analyzed phases indicates that the stopping powers and ^{18}O(α,n)^{21}Ne cross sections are both accurate at the level of

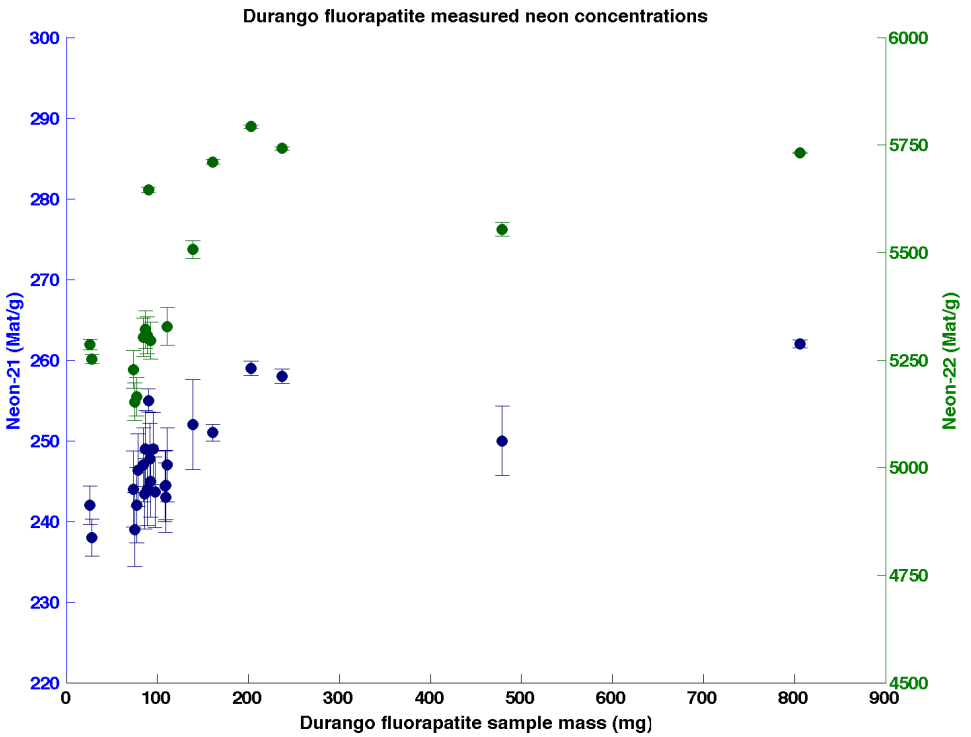

Figure 1.4: Durango fluorapatite ^{21}Ne (left axis) and ^{22}Ne (right axis) concentrations per gram of sample for all measured aliquots, plotted against sample size.

better than 3%. If the stopping powers were incorrect, one or both phases would exhibit ^{21}Ne production rates inconsistent with predicted values, and the difference would not be systematic. If the cross section were incorrect, we would observe a systematic difference between measured and predicted production rates in each target regardless of stopping power.

The quartz data differ by an average of 2.8% from the modeled production rates, with the modeled rates slightly higher. The barium tungstate data differ by 0.6% with the modeled rates slightly lower. These relationships may imply that the cross section is correct and that the quartz stopping powers are 3.0% too low, but the standard deviation of the measured to modeled production rate ratios is about 4% for

both targets, so the difference for both is within the uncertainty of the measurements.

1.4.2 Durango fluorapatite systematics

We find that the (U–Th)/^{21}Ne age of the Durango fluorapatite is 34.5 ± 3.3 Ma. This is in agreement with the accepted age of the standard (31.44 ± 0.18 Ma; McDowell et al. 2005), albeit with an uncertainty larger than we believe to be obtainable with the (U–Th)/^{21}Ne system, for reasons outlined below. For several of the third set of Durango fluorapatite measurements, we simultaneously measured (U–Th)/He ages of the same aliquots and obtained a mean age of 32.6 ± 0.7 Ma (Table 5). This value is near the accepted age, and serves primarily as a check on the procedures used for noble gas and uranium and thorium analyses.

The three sets of Durango fluorapatite experiments reported here varied in methodology. The first two sets each contained eight samples of roughly the same mass, with the only difference being the use of isotope dilution for the second set of samples. The third set contained six samples of broadly varying mass chosen to explore the source of the unexpectedly high (U–Th)/^{21}Ne ages of the first two sets. The third set of analyses was made without isotope dilution, a necessary first step in analyzing fluorapatite samples because of the presence of natural ^{22}Ne. In the third set, it is clear that the ratio of measured neon signal to neon concentration in the mass spectrometer varies with sample size (Figure 1.4), and that only the smallest samples provide ages close to the accepted age of the Durango fluorapatite standard. The cause of this correlation is not clear, and is under investigation, but it may be related to ion source effects from incomplete removal of helium (prior

to cryogenic separation, helium is present at a concentration approximately eight orders of magnitude higher than that of neon), or to other gases extracted from fluorapatite at high temperature. We note that for samples without nucleogenic ^{22}Ne, isotope dilution offers a path around such problems.

Apatite (U–Th)/^{22}Ne chronometry depends on the concentration of fluorine in the apatite, which is much more variable than the oxygen content. However, the production rate of ^{22}Ne is much higher than that of ^{21}Ne because while the cross section for ^{19}F(α,n)^{22}Ne is about half that of ^{18}O(α,n)^{21}Ne, the isotope abundance of ^{19}F (100%) is much higher than that of ^{18}O (~0.2%). For example, we measure a ^{22}Ne/^{21}Ne production rate ratio of 21.52 ± 0.14 in Durango fluorapatite despite the fact that the F/O ratio is approximately 0.09. The exact relationship between F/O and ^{22}Ne/^{21}Ne production will vary slightly with oxygen isotope composition, sample age, and Th/U ratio, but will be approximately (^{22}Ne/^{21}Ne)/ (F/O) = 0.0042 in near-endmember fluorapatite.

In addition to its use as a chronometer, (U–Th)/^{22}Ne may be combined with (U–Th)/^{21}Ne in the same mineral as a method for determining the fluorine content. If isotope dilution with ^{22}Ne is not used, ^{22}Ne can also be measured to investigate contamination with apatite or another fluorine-containing phase (e.g., titanite or fluorite).

1.4.3 Neon production rates in other uranium- and thorium-bearing minerals based on validated cross section

The appendix includes MATLAB code that can be used to compute nucleogenic neon production rates and (U–Th)/Ne ages for a variety of minerals. Users may define the uranium, thorium, helium, and neon contents and δ^{18}O of minerals. The user can also change the cross section, stopping power, mineral stoichiometries, and oxygen contents within the code. This software has not been evaluated by Geochimica et Cosmochimica Acta or its reviewers.

In Table 6 we provide mineral-specific production rates of ^{21}Ne and ^{22}Ne per alpha particle for the decay chains starting with ^{238}U, ^{235}U, and ^{232}Th assuming secular equilibrium. These production rates can be used to calculate (U–Th)/Ne ages or to interpret neon/helium ratios in these minerals. Production rates average around $4.5\text{x}10^{-8}$ per alpha particle for ^{21}Ne for all three decay chains in each mineral. Using this value and assuming a Th/U ratio of 1, we estimate the age and uranium and thorium concentrations required to obtain measurable ^{21}Ne in a mineral (Figure 1.5). In order to plot this result in two dimensions, we use "equivalent uranium" (alpha activity represented as concentration of uranium; Gastil et al. 1967) and define "measurable neon" as 65,000 atoms, or about 1.5 cps on our mass spectrometer. This requirement assumes a very low amount of non-nucleogenic ^{21}Ne; if a large air correction is required for an analysis, more nucleogenic neon is required to achieve good precision (Section 2.3.2).

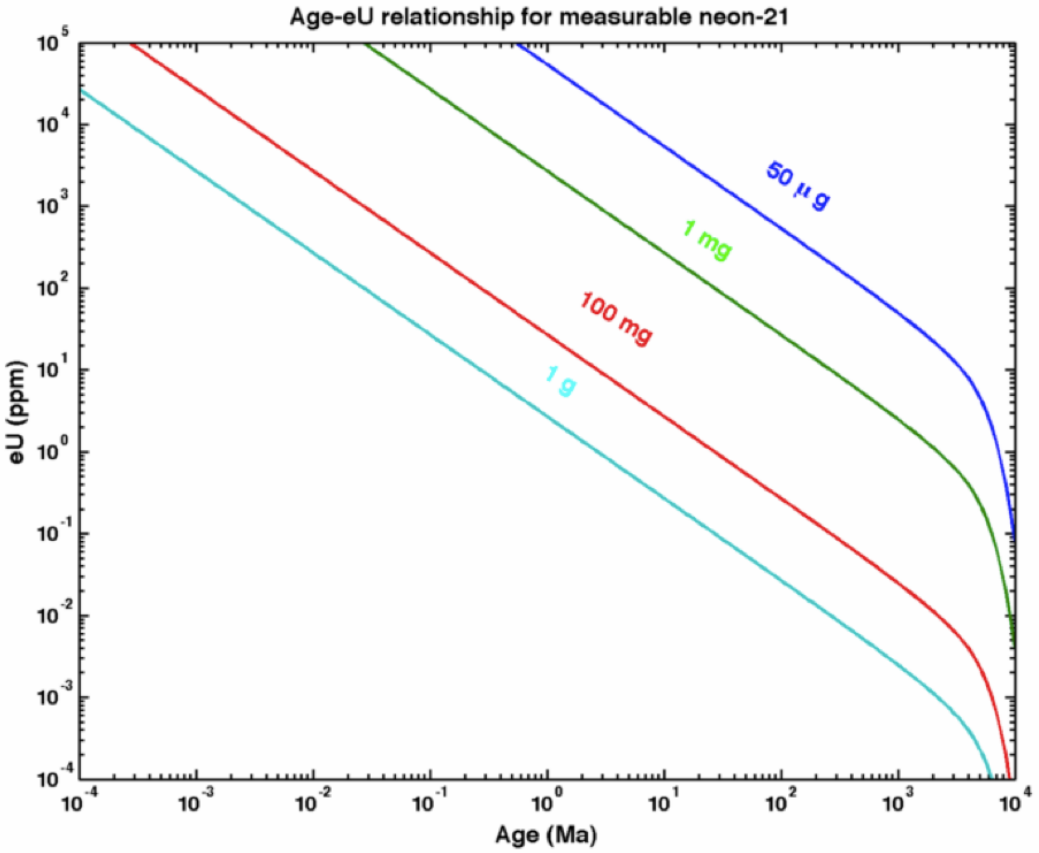

Figure 1.5: Relationship between age and effective uranium concentration (eU = U + 0.235 x Th, accounting for alpha dose over time) required for a measurable amount of ^{21}Ne (defined as 65,000 atoms) in a generic mineral with a fixed ^{21}Ne/^{4}He production rate ratio of 4.5×10^{-8}, assuming a Th/U ratio of 1. The different lines reflect different sample sizes. The actual production rate will vary slightly according to mineralogy and Th/U ratio.

1.4.3.1 Zircon, xenotime, thorite, and coffinite

The isostructural tetragonal minerals zircon and xenotime are commonly used for (U–Th)/Pb and, in the case of zircon, (U–Th)/He geochronometry and thermochronometry and may also be of interest for (U–Th)/Ne chronometry. Based on comparison with ages of other thermochronometers, Gautheron et al. (2006) estimated a neon closure temperature in zircon of 400±50°C. Closure temperatures for the (U–Th)/Ne system intermediate between the helium and lead systems in these

minerals raise the possibility of adding it to multiple chronometer thermochronology studies, and the (U–Th)/Ne system may also be used as a tool to expose or investigate problems with these chronometers in low-temperature and volcanic systems. Thorite and coffinite are less common, especially as euhedral crystals suitable for chronological studies, but may occur as inclusions or associated accessories in other minerals of chronological interest, and may be of interest themselves in unusual settings.

1.4.3.2 Titanite and baddeleyite

Other common candidates for (U–Th)/Pb dating include titanite and baddeleyite, both of which may be targeted for (U–Th)/Ne dating for the same reasons as the silicates in Section 4.3.1. Replacement reactions between baddeleyite and zircon may be more likely to completely reset the (U–Th)/Ne system than the (U–Th)/Pb system, especially when the reaction occurs in the direction zircon to baddeleyite, because lead is very resistant to diffusive loss (Cherniak and Watson, 2001). The different production rates of neon in zircon and baddeleyite, arising from differences in oxygen concentration, should also be noted because they often occur in close association.

1.4.3.3 Uraninite, thorianite, and the implications of micro-inclusions

Minerals such as uraninite and thorianite are unlikely to occur in large crystals with well behaved (U–Th)/Ne systematics, but may occur as micro-inclusions in other minerals of interest, especially as alteration products in hydrothermal systems. Even

very small inclusions will have a profound impact on the (U–Th)/Ne systematics of host phases due to the very high uranium and thorium concentrations of these minerals and the fact that neon production peaks very close to the source of alpha particles. Furthermore, very uranium-rich phases will become radiation damaged and will probably exhibit anomalous diffusivities for neon, as is observed in similar situations for helium (Hurley, 1954; Nasdala et al., 2004; Shuster, Flowers, et al., 2006; Shuster and Farley, 2009; Guenthner et al., 2013).

The phases above are typically very high in uranium and/or thorium, and will therefore likely exhibit high nucleogenic ^{21}Ne concentrations relative to air contamination and small amounts of cosmogenic contamination. The phases below typically have much lower uranium and thorium concentrations, so air contamination in the vacuum line and air adsorbed to and trapped within the samples will be a more significant factor affecting the precision of the measurements, and samples must be more carefully selected and screened for cosmogenic neon contamination. This applies especially to samples that form at or near the Earth's surface, such as carbonates, where cosmogenic neon contamination is more likely.

1.4.3.4 Hematite, goethite, and magnetite

Iron oxides frequently contain ppm-level concentrations of uranium and thorium that are adequate for the production of radiogenic helium and neon (Lippolt et al., 1993; Shuster, Vasconcelos, et al., 2005; Farley and Flowers, 2012). These uranium and thorium concentrations and high common lead concentrations prevent the use of the (U–Th)/Pb system on these minerals. Neon appears to be retained at surface

temperatures in iron oxides, and the (U–Th)/Ne system is therefore already in use as a geochronometer in hematite (Farley and Flowers, 2012). Because of the low uranium and thorium concentrations in the minerals themselves, care must be taken to either exclude or account for inclusions of other minerals that contain these elements.

1.4.3.5 Calcite and aragonite

Carbonates are similar to iron oxides in that low uranium and thorium concentrations and common lead contamination sometimes complicate the (U–Th)/Pb system (Rasbury and Cole, 2009) while low and variable helium retention complicates the (U–Th)/He system (Cros et al., 2014). Neon production rates are insufficient for dating of most Pleistocene marine carbonates using the (U–Th)/Ne system due to low uranium and thorium concentrations, but older deposits or deposits with unusually high uranium and thorium concentrations are candidates for (U–Th)/Ne geochronology.

1.5 Conclusions

We present direct measurements of the ^{21}Ne production rates of mono-energetic alpha particles in two targets, which allows us to verify the ^{18}O(α,n)^{21}Ne cross section and the stopping powers independently. These measurements agree well with the cross section data compiled by (Gautheron et al., 2006) and with stopping power calculations using SRIM, affirming the validity of the calculated production rates at the ~3% level. These production rates are presented here along with software for

the calculation of production rates in other minerals and of (U–Th)/Ne ages. These results allow geochemists to apply the (U–Th)/Ne system to questions about Earth history, including medium-temperature thermochronometry and geochronometry in rocks with high uranium or older than ∼10 Ma, with a better understanding of the inherent uncertainty in the system.

References

Bair, J. K. and J. G. Del Campo (1979). "Neutron Yields From Alpha-Particle Bombardment". In: *Nuclear Science and Engineering* 71, pp. 18–28.

Bair, J. and H. Willard (1962). "Level Structure in Ne^{22} and Si^{30} from the Reactions $O^{18}(\alpha,n)Ne^{21}$ and $Mg^{26}(\alpha,n)Si^{29}$". In: *Physical Review* 128.1, pp. 299–304.

Behrens, H. (2010). "Noble Gas Diffusion in Silicate Glasses and Melts". In: *Reviews in Mineralogy and Geochemistry*.

Boyce, J. and K. V. Hodges (2005). "U and Th zoning in Cerro de Mercado (Durango, Mexico) fluorapatite: Insights regarding the impact of recoil redistribution of radiogenic ^{4}He on (U–Th)/He thermochronology". In: *Chemical Geology* 219, pp. 261–274.

Cherniak, D. J., J. B. Thomas, and E. B. Watson (2014). "Neon diffusion in olivine and quartz". In: *Chemical Geology*.

Cherniak, D. J. and E. B. Watson (2001). "Pb diffusion in zircon". In: *Chemical Geology* 172.1-2, pp. 5–24.

Cros, A., C. Gautheron, M. Pagel, P. Berthet, L. Tassan-Got, E. Douville, R. Pinna-Jamme, and P. Sarda (2014). "^{4}He behavior in calcite filling viewed by (U–Th)/He dating, ^{4}He diffusion and crystallographic studies". In: *Geochimica et Cosmochimica Acta* 125, pp. 414–432.

Eiler, J. M., A. Crawford, T. Elliott, K. A. Farley, J. W. Valley, and E. M. Stolper (2000). "Oxygen Isotope Geochemistry of Oceanic-Arc Lavas". In: *Journal of Petrology* 41.2, pp. 229–256.

Farley, K. A. and R. M. Flowers (2012). "(U–Th)/Ne and multidomain (U–Th)/He systematics of a hydrothermal hematite from eastern Grand Canyon". In: *Earth and Planetary Science Letters* 359-360, pp. 131–140.

Farley, K. (2000). "Helium diffusion from apatite: General behavior as illustrated by Durango fluorapatite". In: *Journal of Geophysical Research* 105.B2, pp. 2903–2914.

Gastil, R. G., M. DeLisle, and J. R. MORGAN (1967). "Some Effects of Progressive Metamorphism on Zircons". In: *Geological Society of America Bulletin* 78.7, p. 879.

Gautheron, C., L. Tassan-Got, and K. Farley (2006). "(U–Th)/Ne chronometry". In: *Earth and Planetary Science Letters* 243, pp. 520–535.

Guenthner, W. R., P. W. Reiners, R. A. Ketcham, L. Nasdala, and G. Giester (2013). "Helium diffusion in natural zircon: Radiation damage, anisotropy, and the interpretation of zircon (U-Th)/He thermochronology". In: *American Journal of Science* 313.3, pp. 145–198.

Hansen, L. F., J. D. Anderson, J. W. McClure, B. A. Pohl, M. L. Stelts, J. J. Wesolowski, and C. Wong (1967). "The (α, n) cross sections on ^{17}O and ^{18}O between 5 and 12.5 MeV". In: *Nuclear Physics A* 98.1, pp. 25–32.

House, M. and K. Farley (2000). "Helium chronometry of apatite and titanite using Nd-YAG laser heating". In: *Earth and Planetary Science Letters* 183.3-4, pp. 365–368.

Hünemohr, H. (1989). "Edelgase in U- und Th- reichen Mineralen und die Bestimmung der ^{21}Ne-Dicktarget-Ausbeute der ^{18}O(α,n)^{21}Ne- Kernreaktion im Bereich 4.0-8.8 MeV". PhD thesis. Mainz, Germany: Max-Planck-Institut fur Chemie.

Hurley, P. M. (1954). "The helium age method and the distribution and migration of helium in rocks". In: *Nuclear Geology*. Ed. by H. Faul. Wiley and Sons, pp. 301–329.

Kennedy, B. M., H. Hiyagon, and J. H. Reynolds (1990). "Crustal neon: a striking uniformity". In: *Earth and Planetary Science Letters* 98.3-4, pp. 277–286.

Kyser, T. K. and W. Rison (1982). "Systematics of rare gas isotopes in basic lavas and ultramafic xenoliths". In: *Journal of Geophysical Research* 87.B7, p. 5611.

Leya, I. and R. Wieler (1999). "Nucleogenic production of Ne isotopes in Earth's crust and upper mantle induced by alpha particles from the decay of U and Th". In: *Journal of Geophysical Research* 104.B7, pp. 15439–15450.

Lippolt, H. J., R. S. Wernicke, and W. Boschmann (1993). "^{4}He diffusion in specular hematite". In: *Physics and Chemistry of Minerals* 20.6, pp. 415–418.

McDowell, F. W., W. C. McIntosh, and K. A. Farley (2005). "A precise ^{40}Ar-^{39}Ar reference age for the Durango apatite (U-Th)/He and fission-track dating standard". In: *Chemical Geology* 214.3-4, pp. 249–263.

Murata, T., H. Matsunobu, and K. Shibata (2006). "Evaluation of the (α, xn) reaction data for JENDL/AN-2005". In: *Japan Atomic Energy Agency-Research*, p. 78.

Nadeau, S. L., S. Epstein, and E. Stolper (1999). "Hydrogen and carbon abundances and isotopic ratios in apatite from alkaline intrusive complexes, with a focus on carbonatites". In: *Geochimica et Cosmochimica Acta* 63.11-12, pp. 1837–1851.

Nasdala, L., P. W. Reiners, J. I. Garver, A. K. Kennedy, R. A. Stern, E. Balan, and R. Wirth (2004). "Incomplete retention of radiation damage in zircon from Sri Lanka". In: *American Mineralogist* 89, pp. 219–231.

Niedermann, S. (2002). "Cosmic-Ray-Produced Noble Gases in Terrestrial Rocks: Dating Tools for Surface Processes". In: *Reviews in Mineralogy and Geochemistry* 16, pp. 731–784.

Norman, E., T. Chupp, K. Lesko, P. Grant, and G. Woodruff (1984). "^{22}Na production cross sections from the ^{19}F(α, n) reaction". In: *Physical review C: Nuclear physics* 30.4, pp. 1339–1340.

Rasbury, E. T. and J. M. Cole (2009). "Directly dating geologic events: U-Pb dating of carbonates". In: *Reviews of Geophysics* 47, RG3001.

Shuster, D. L., R. M. Flowers, and K. A. Farley (2006). "The influence of natural radiation damage on helium diffusion kinetics in apatite". In: *Earth and Planetary Science Letters* 249, pp. 148–161.

Shuster, D. L. and K. A. Farley (2005). "Diffusion kinetics of proton-induced ^{21}Ne, ^{3}He, and ^{4}He in quartz". In: *Geochimica et Cosmochimica Acta* 69.9, pp. 2349–2359.

— (2009). "The influence of artificial radiation damage and thermal annealing on helium diffusion kinetics in apatite". In: *Geochimica et Cosmochimica Acta* 73.1, pp. 183–196.

Shuster, D. L., P. M. Vasconcelos, J. A. Heim, and K. A. Farley (2005). "Weathering geochronology by (U-Th)/He dating of goethite". In: *Geochimica et Cosmochimica Acta* 69.3, pp. 659–673.

Solé, J. and T. Pi (2006). "Determination of the 22Nenucl/4Herad ratio in natural uranium-rich fluorite by mass". In: *Physical Review C* 74.4.

Tournour, C. C. and J. E. Shelby (2008a). "Helium solubility in alkali silicate glasses and melts". In: *Physics and Chemistry of Glasses - European Journal of Glass Science and Technology Part B* 49.4, pp. 207–215.

— (2008b). "Neon solubility in silicate glasses and melts". In: *Physics and Chemistry of Glasses - European Journal of Glass Science and Technology Part B* 49.5, pp. 237–244.

Wetherill, G. (1954). "Variations in the Isotopic Abundances of Neon and Argon Extracted from Radioactive Minerals". In: *Physical Review* 96.3, pp. 679–683.

Wrean, P. and R. Kavanagh (2000). "Total cross sections and reaction rates for ^{19}F(α,n)^{22}Na, ^{22}Ne(p,n)^{22}Na, and their inverses". In: *Physical Review C* 62.5, p. 055805.

Yatsevich, I. and M. Honda (1997). "Production of nucleogenic neon in the Earth from natural radioactive decay". In: *Journal of Geophysical Research* 102.B5, p. 10291.

Ziegler, J. F., M. D. Ziegler, and J. P. Biersack (2010). “SRIM – The stopping and range of ions in matter (2010)”. In: *Nuclear Instruments and Methods in Physics Research Section B: Beam Interactions with Materials and Atoms* 268.11-12, pp. 1818–1823.

Alpha Energy (MeV)	Ne Method	He Method	^{21}Ne (Mat)	^{21}Ne ± (Mat)	^{4}He (Tat)	^{4}He ± (Tat)	^{21}Ne/^{4}He (10^{-8})	^{21}Ne/^{4}He +	^{21}Ne/^{4}He -
Quartz									
4.5	No ID	Current	16.5	1.8	1163	23	1.58	0.08	0.17
5	No ID	Current	13.3	1.5	684	14	2.63	0.13	0.68
5.25	ID	Current	14.3	0.6	467	9	3.06	0.12	0.12
5.5	ID	Current	14	0.6	397	8	3.51	0.14	0.14
6	ID	Current	18.2	0.7	343	7	5.30	0.21	0.21
6.25	ID	Current	18.5	0.8	300	6	6.17	0.25	0.25
6.5	ID	Current	18.4	0.8	264	5	6.96	0.28	0.28
7	ID	Current	18.9	0.8	210	4	9.00	0.36	0.36
7.3	ID	Current	16.5	0.7	170	3	9.72	0.39	0.39
7.8	ID	Current	10.4	1.1	140	3	7.47	0.82	0.82
7.8	ID	Current	14.8	0.2	140	3	10.6	0.15	0.15
BaWO4									
4.5	ID	MS	9.09	0.15	892	2	1.02	0.02	0.05
5	ID	MS	12.2	0.2	710	1	1.72	0.03	0.06
5.25	ID	MS	10.9	0.2	570	1	1.92	0.03	0.10
5.5	No ID	MS	8.36	0.13	481.7	1	2.43	0.12	0.69
6	ID	MS	11.3	0.2	335.2	0.7	3.38	0.05	0.05
6	ID	MS	10.6	0.2	332.7	0.7	3.18	0.05	0.05
6.25	ID	MS	12.1	0.2	291.8	0.6	4.13	0.07	0.07
6.5	ID	MS	12.9	0.2	293.8	0.6	4.40	0.07	0.07
7	ID	Current	13.4	0.2	250	5	5.35	0.08	0.08
7.3	ID	MS	11.5	0.2	184.4	0.4	6.22	0.10	0.57
7.8	ID	MS	16.5	0.3	209.1	0.4	7.89	0.47	0.12

Table 1.1: Neon and helium data for implanted quartz and barium tungstate. Column "Ne Method" indicates whether we used isotope dilution for the neon measurement ("ID") or rejected it due to a hardware problem in favor of sample–standard bracketing ("No ID"). Column "He Method" indicates whether we calculated the amount of implanted helium from the integrated beam current on the Dynamitron with 2% assumed uncertainty ("Current") or from a direct measurement by mass spectrometry ("MS"). Last two columns give the + and - uncertainties separately since they are asymmetric. All uncertainties are 1 standard deviation.

Number	mass (mg)	^{21}Ne (Mat/g)	^{21}Ne ± (Mat/g)	^{21}Ne ± (%)	^{22}Ne (Mat/g)	^{22}Ne ± (Mat/g)	^{22}Ne ± (%)	^{22}Ne/^{21}Ne	^{22}Ne/^{21}Ne ±	^{22}Ne/^{21}Ne ± (%)
1	77.32	242	5	2.00%	5165	45	0.87%	21.3	0.6	2.60%
2	75.04	239	5	1.90%	5153	44	0.85%	21.6	0.6	2.60%
3	73.51	244	5	1.90%	5228	44	0.85%	21.4	0.5	2.50%
4	87.05	249	5	1.90%	5321	44	0.83%	21.4	0.5	2.50%
5	84.85	247	5	1.90%	5303	44	0.83%	21.5	0.5	2.50%
6	88.77	244	5	1.80%	5307	43	0.81%	21.8	0.5	2.40%
7	92.58	245	5	1.90%	5296	43	0.82%	21.7	0.5	2.50%
8	110.9	247	5	1.90%	5328	44	0.82%	21.6	0.5	2.40%
Average 1–8		244			5262			21.5		
SE (2σ)		0.88%			0.95%			0.46%		
Number	mass (mg)	^{21}Ne (Mat/g)	^{21}Ne ± (Mat/g)	^{21}Ne ± (%)	^{21}Ne (Mat/g) ID	^{21}Ne ± (Mat/g) ID	^{21}Ne ± (%) ID			
9	97.27	244	4	1.80%	241	6	2.30%			
10	78.66	246	5	1.80%	246	6	2.40%			
11	108.95	243	4	1.80%	240	5	2.30%			
12	95.51	249	4	1.80%	246	6	2.30%			
13	86.36	243	4	1.80%	245	6	2.30%			
14	91.82	248	4	1.80%	248	6	2.30%			
15	109.39	245	4	1.80%	243	6	2.30%			
16	108.22	244	4	1.80%	243	6	2.30%			
Average 9–16		245.25			244.01					
SE (2σ)		0.63%			0.80%					
Number	mass (mg)	^{21}Ne (Mat/g)	^{21}Ne ± (Mat/g)	^{21}Ne ± (%)	^{22}Ne (Mat/g)	^{22}Ne ± (Mat/g)	^{22}Ne ± (%)	^{22}Ne/^{21}Ne	^{22}Ne/^{21}Ne ±	^{22}Ne/^{21}Ne ± (%)
17	90	255	1	1.60%	5646	6	0.30%	22.13	0.12	1.63%
18	203	259	1	1.10%	5793	4	0.20%	22.33	0.08	1.09%
19	26.1	242	2	3.00%	5286	12	0.70%	21.84	0.22	3.01%
20	806	262	1	0.50%	5732	2	0.10%	21.86	0.04	0.55%
21	28.2	238	2	2.90%	5252	11	0.60%	22.05	0.21	2.91%
22	161	251	1	1.20%	5711	5	0.30%	22.77	0.09	1.24%
23	237	258	1	1.00%	5742	4	0.20%	22.3	0.08	1.01%
24	139	252	6	6.70%	5507	21	1.10%	21.89	0.5	6.79%
25	479	250	4	5.20%	5554	16	0.90%	22.24	0.39	5.27%
Average 17–25		252			5580			22.16		
SE (2σ)		2.10%			2.40%			0.90%		

Table 1.2: Neon isotope data of Durango fluorapatite. SE — standard error of the mean. Uncertainties on individual analyses reflect 1σ analytical error, while population uncertainties reflect 2σ standard error. When isotope dilution is used, ^{21}Ne concentrations calculated with isotope dilution (ID) and without are shown for comparison.

Number	mass (mg)	^{4}He (Tat/g)	^{4}He ± (Tat/g)	^{4}He ± (‰)	^{21}Ne/^{4}He (10^{-8})	^{21}Ne/^{4}He (10^{-8}) ±	^{22}Ne/^{4}He (10^{-8})	^{22}Ne/^{4}He (10^{-8}) ±
1	77.32	5499	55	1‰	4.4	0.1	93.9	1.3
2	75.04	5518	55	1‰	4.33	0.09	93.4	0.9
3	73.51	5550	56	1‰	4.4	0.09	94.2	0.9
4	87.05	5578	56	1‰	4.46	0.1	95.4	0.9
5	84.85	5519	55	1‰	4.47	0.1	96.1	0.9
6	88.77	5566	56	1‰	4.38	0.09	95.3	0.9
7	92.58	5539	55	1‰	4.41	0.09	95.6	0.9
8	110.9	5561	56	1‰	4.44	0.09	95.8	0.9
Average 1–8		5541			4.41		95	
SE (2σ)		0.35‰			1‰		1‰	
Number	mass (mg)	^{4}He (Tat/g)	^{4}He ± (Tat/g)	^{4}He ± (‰)	^{21}Ne/^{4}He (10^{-8})	^{21}Ne/^{4}He (10^{-8}) ±	^{21}Ne (ID)/^{4}He (10^{-8})	^{21}Ne (ID)/^{4}He (10^{-8}) ±
9	97.3	5550	56	1‰	4.39	0.09	4.34	0.11
10	78.7	5512	55	1‰	4.47	0.09	4.46	0.11
11	109	5494	55	1‰	4.42	0.09	4.37	0.11
12	95.5	5583	56	1‰	4.46	0.09	4.41	0.11
13	86.4	5503	55	1‰	4.42	0.09	4.44	0.11
14	91.8	5536	55	1‰	4.47	0.09	4.48	0.11
15	109.4	5563	56	1‰	4.4	0.09	4.36	0.11
16	108	5515	55	1‰	4.43	0.09	4.41	0.11
Average 9–16		5532			4.43		4.41	
SE (2σ)		0.40‰			0.52‰		0.81‰	

Table 1.3: Helium and Ne/He data for Durango fluorapatite. Uncertainties on individual analyses reflect 1σ analytical error, while population uncertainties reflect 2σ standard error.

Sample	Mass (μg)	U (ppm)	U ± (ppm)	Th (ppm)	Th ± (ppm)	Th/U	Ne Age (Ma)	Ne Age ± (Ma)
A	133.6	9.21	0.12	173.9	1.2	18.8	33.8	1.4
B	257.3	8.99	0.13	169.8	1.1	18.9	34.6	1.4
C	298.2	8.87	0.15	170.2	1.2	19.2	34.7	1.4
D	100.9	8.79	0.13	167.4	1	19	35.3	1.4
	Average A–D	8.97	0.18	170	2.7	19	34.6	2.4
E	27.37	9.51	0.11	183.7	0.6	19.3	32.5	1.3
F	29.54	9.33	0.1	173.3	0.6	18.6	35.1	1.4
G	39.33	9.2	0.06	175.2	0.6	19	35.2	1.4
H	35.57	9.2	0.08	176	0.6	19.1	35.1	1.4
I	35.12	9.38	0.08	178.1	0.6	19	34	1.4
	Average E–I	9.32	0.13	177.3	4	19	34.4	2.1

Table 1.4: Uranium, thorium, and (U–Th)/Ne age data for Durango fluorapatite based on multiple aliquots for uranium and thorium and the population averages for neon for the first two datasets. Uncertainties on individual analyses reflect 1σ analytical error, while population uncertainties reflect 2σ standard error.

Number	mass (mg)	^{4}He (Tat/g)	^{4}He ± (Tat/g)	^{4}He ± (%)	He Age (Ma)	He Age ± (Ma)
5	28.23	5441	54	1%	32.62	0.49
6	161.18	5435	54	1%	32.58	0.49
7	236.62	5500	55	1%	32.98	0.50

Table 1.5: Helium and (U–Th)/He age data for part of the third dataset, using population averages of uranium and thorium. For these analyses, we increased the split size of the helium in order to obtain accurate (U–Th)/He ages.

Mineral	Target Composition		Production rates for each decay chain from ^{18}O			Production rates for each decay chain from ^{19}F		
	[O]	[F]	^{238}U ^{21}Ne/^{4}He	^{235}U ^{21}Ne/^{4}He	^{232}Th ^{21}Ne/^{4}He	^{238}U ^{22}Ne/^{4}He	^{235}U ^{22}Ne/^{4}He	^{232}Th ^{22}Ne/^{4}He
	(wt. fraction)	(wt. fraction)	(10^{-8})	(10^{-8})	(10^{-8})	(10^{-8})	(10^{-8})	(10^{-8})
Quartz	0.5326	0	4.04	5.62	6.08	–	–	–
Barium Tungstate	0.1662	0	2.44	3.39	3.66	–	–	–
Zircon	0.3491	0	3.38	4.70	5.08	–	–	–
Xenotime-(Y)	0.3480	0	3.34	4.65	5.03	–	–	–
Thorite	0.1974	0				–	–	–
Coffinite	0.1953	0	2.85	3.95	4.26	–	–	–
Titanite	0.4080	0	3.33	4.63	5.01	–	–	–
Baddeleyite	0.2597	0	2.90	4.04	4.36	–	–	–
Hematite	0.3006	0	2.80	3.89	4.21	–	–	–
Maghemite	0.3006	0	2.80	3.89	4.21	–	–	–
Goethite	0.3602	0	3.14	4.37	4.73	–	–	–
Magnetite	0.2764	0	2.60	3.62	3.91	–	–	–
Calcite	0.4795	0	3.59	5.00	5.41	–	–	–
Aragonite	0.4795	0	3.59	5.00	5.41	–	–	–
Uraninite	0.1185	0	2.17	3.01	3.24	–	–	–
Thorianite	0.1212	0				–	–	–
Cryptomelane	0.3485	0	3.14	4.37	4.72	–	–	–
Fluorapatite	0.3801	0.0352	3.02	4.20	4.54	42.1	64.5	73.9
Fluorite	0	0.4867	–	–	–	595	915	1044

Table 1.6: Average ^{21}Ne and ^{22}Ne production rates calculated based on verified production rates in a variety of minerals for each decay chain for stoichiometric compositions (obtained at webmineral.com) and δ^{18}O = +6‰. Production rates assume secular equilibrium for each decay chain.

Chapter 2

Ne Diffusion in Polycrystalline Hematite and Single Crystal Corundum

Abstract

We show Ne diffusivity as a function of temperature in polycrystalline hematite to demonstrate Ne retention for (U–Th)/Ne dating. We performed step-heating Ne diffusion experiments on the Caltech MI-43 hematite standard. We also measured He and Ne diffusion in corundum, a mineral with the same structure as hematite that typically forms large euhedral crystals rather than the bladed crystallites formed by hematite. Ne diffusion in polycrystalline hematite exhibits the same complex behavior observed in He diffusion from hematite. The highest temperature experiments show an activation energy of Ea = 3.9 (±0.1) x 10^5 J/mol for Ne diffusion in both hematite and corundum. Hematite diffusion domains span more than five orders of magnitude in apparent physical size, while corundum exhibits single domain behavior. As with He diffusivity, apparent Ne diffusivity in hematite depends on the crystallite size and shape distribution in a particular sample, so diffusion experiments are necessary on each sample for thermochronometry. For geochronometry, we establish that more than 94% of Ne is retained at temperatures over 290°C, with $\ln(D_0/a^2)$ = 49.3 $\ln(s^{-1})$. The closure temperatures for the most retentive domains in our sample are around 500°C, so the (U–Th)/Ne system can be used to probe a large portion of the thermal history of a rock.

2.1 Introduction

Neon isotopes are produced in minerals by nuclear reactions on light elements, most importantly via capture of α particles by oxygen and fluorine. Although the probability of these reactions is very low, the accumulated nucleogenic neon is readily measured in a variety of minerals. Recent studies have demonstrated the use of nucleogenic neon as a chronometer for dating minerals including apatite, zircon, fluorite, and hematite (Gautheron et al., 2006; Solé and Pi, 2006; Farley and Flowers, 2012; Farley and McKeon, 2015). However, little is known of the diffusion behavior of neon in minerals, making it difficult to evaluate possible open system behavior. Such information is essential for assessing whether (U–Th)/Ne ages date mineral formation, or if instead they should be considered cooling ages.

Hematite is a particularly interesting phase for (U–Th)/^{21}Ne chronometry. The formation age of hematite is difficult to measure with standard radiometric techniques because the hematite structure does not favor incorporation of the parent isotopes. While concentrations of order 1 ppm of U and Th are common, hematite typically also contains significant common Pb, making U/Pb geochronology challenging. In contrast, hematite appears to have remarkably low initial ^{21}Ne, indicating very effective exclusion of atmospheric neon. As a result, even the slow production of ^{21}Ne can be measured in large (hundreds of mg) hematite samples of typical U concentration older than a few tens of Ma (Farley and Flowers, 2012; Cox et al., 2015).

Many natural hematite specimens are aggregates of crystallites of micron to

sub-micron dimensions. He diffusion experiments show that these crystallites act as isolated diffusion domains, with the intergranular space providing a fast He migration pathway. The experiments indicate an activation energy of ~160 kJ/mol, and a large range in domain size thought to reflect the crystallite size distribution. A polycrystalline hematite sample therefore carries a spectrum of He closure temperatures, which has been found to encompass a range from about Earth surface temperature to ~200°C (Farley and Flowers, 2012; Farley and McKeon, 2015). By combining the diffusion data with a ^{4}He/^{3}He experiment, a ^{4}He/^{3}He age spectrum and associated cooling path through this temperature range can be obtained. Of importance for the current study, ^{4}He/^{3}He age plateaus measured on several previously studied hematite samples are within error of the (U–Th)/^{21}Ne age of the same sample (Farley and McKeon, 2015). The simplest interpretation of this agreement is that the ^{21}Ne age is a formation age, and the bulk Ne closure temperature exceeds the highest closure temperature in the He system, about 200°C. Recently Balout, Roques, Gautheron, and Tassan-Got (2017) also published a model study of Ne diffusion in hematite that showed high retention, although with an activation energy of 2.3×10^{5} J/mol, much lower than we observe in this paper.

Direct measurement of Ne diffusion in hematite is complicated by several factors. First, it is reasonable to expect that Ne, like He, will demonstrate poly-diffusion domain behavior associated with the range of crystallite sizes in the specimen. Such behavior can be interpreted only if a fairly large number of heating steps are used in the diffusion experiment. This is problematic because the ^{21}Ne content of hematite is

fairly low, and so not amenable to dividing into many steps. A variety of techniques have been used to solve this general problem in noble gas diffusion studies, but none are applicable to neon in hematite. Neither neutron nor proton irradiation produces significant quantities of Ne in a mineral comprising only iron and oxygen, and implantation with ionized Ne or α particles (to produce Ne indirectly) produces a thin layer of highly concentrated Ne near the mineral surface that is a challenge to use for a volume diffusion experiment, especially in a complex polycrystalline material. To avoid these complications, we have chosen to use natural ^{21}Ne in an especially Ne-rich hematite. Even with a Ne-rich sample, this approach still requires a large sample mass, so we built a diffusion cell based on a large double-vacuum resistance furnace to ensure uniform heating of samples in excess of 1 gram (Figure 2.1).

As a complementary approach, we have also investigated neon diffusion in corundum. Corundum and hematite are isomorphic, and the replacement of Fe by Al allows proton irradiation as a source for a high concentration of homogeneous ^{21}Ne. By measuring neon diffusion in a single crystal of corundum, we hope to shed further light on the behavior of neon in hematite. An analogous approach was used to illuminate He diffusion behavior in isomorphic rare earth phosphates of the zircon and monazite structures (Farley, 2007).

2.2 Samples and Methods

We chose to investigate neon diffusion in hematite MI-43, studied in detail by Farley and McKeon (2015). This is a high purity hydrothermal hematite associated

with a banded iron formation in the Gogebic iron range in Michigan, USA. It carries 7 ppm U, 0.01 ppm Th, and yields a (U–Th)/^{21}Ne age of 756±18 Ma. The ^{21}Ne in this sample is 97% nucleogenic, amounting to ∼1 fmol/g. The initial specimen was extremely large—over a kg—and a large amount of the sample was crushed, sieved, and homogenized as a standard reference material for future study, including the present work. We sieved MI-43 hematite to a size fraction of 64-90 μm, rinsed it in ethanol, and dried it overnight at 50°C. The sample is pure hematite, so no mineral separation was necessary.

The large diffusion cell used for the hematite experiments comprises a double-vacuum resistance furnace with an insulated thermocouple mounted in the sample volume (Figure 2.1). The furnace provides about 10 cm3 of nearly isothermal volume within the lower part of its niobium crucible. The niobium crucible, the double vacuum configuration, and the type K thermocouple insulated with alumina allow continuous operation up to 1250°C. Temperature is controlled with a PID loop tuned to achieve prograde (increasing) temperature adjustments of 25–50°C in less than 60 seconds with no overshoot, and to achieve retrograde (decreasing) temperature adjustments of up to 500°C in less than five minutes. We operate the furnace continuously during the experiment, periodically removing splits of gas for analysis between temperature adjustments. Changing temperature during the experiment requires careful control because overshooting the setpoint causes unacceptable transient increases in diffusivity. For a prograde adjustment, we use a damped PID control to avoid overshoot or oscillations. For a retrograde adjustment,

we maintain power and allow the temperature to fall slowly to avoid a rapid drop and overcorrection. The sample splits are always taken before a prograde temperature adjustment or after a retrograde temperature adjustment so that the temperature never exceeds the setpoint during a given measurement period. We used step times of an hour or greater. We present results for three aliquots of this sample subjected to three different heating schedules to evaluate and interpret the likely polydomain behavior of this hematite (see Farley and Flowers 2012).

The corundum sample was a 1-2 mm ruby fragment from a large, natural single crystal. The fragments were proton irradiated following Shuster et al. (2005). Irradiation with ~200 MeV protons produces a uniform distribution of ^{3}He and ^{21}Ne through spallation reactions in the target minerals. After irradiation, individual ~1 mm corundum fragments were hand-picked and then mounted in niobium packets suspended from K type thermocouples in a standard diffusion cell (e.g., Farley, 2000) and heated with a diode laser as described in Farley and McKeon (2015).

After being inlet either from the furnace or the diffusion cell, the sample gas passed through several SAES St101 Zr-Al getters, a charcoal trap at liquid nitrogen temperature, and finally into a focusing cryostat (21 K for Ne, 14 K for He). After this step, the gas was introduced directly into a mass spectrometer at 68 K for Ne analysis and at 34 K for He analysis. In all cases, we measured procedural blanks and standards throughout to keep track of sensitivity and mass fractionation. The blanks, standards, and samples were analyzed using exactly the same procedure and split volumes, so no further corrections were necessary. Ne procedural blanks were

mostly air and were less than 80 million atoms for ^{20}Ne and less than 400,000 atoms for ^{21}Ne. Typical amounts after blank and air correction were more than 2 million atoms of ^{21}Ne. We verified pseudo-resolution of ^{20}Ne from $^{40}Ar^{++}$. Other isobars in the mass spectrometer, such as HF, HHF, and $^{44}CO_2^{++}$, are accounted for in the blank. We monitored CO_2^{++} by measuring $^{45}CO_2^{++}$ during each analysis. This isotopologue is present at about 1/70 of $^{44}CO_2^{++}$, but did not exceed its typical dynamic background levels (< 0.5 cps) during any measurement. He procedural blanks amounted to only 71,000 atoms for ^{3}He. Typical samples after blank correction were over 10 million atoms of ^{3}He.

Fractional gas yields for Ne in hematite were calculated using the established Ne concentration for the MI-43 standard from Farley and McKeon (2015) due to the difficulty of complete recovery from the large diffusion cell. Total gas yields for corundum were measured directly by fusing the sample in the resistance furnace. Neon and helium diffusivities were calculated from incremental yields and isothermal holding time using the spherical model equations of Fechtig and Kalbitzer (1966). For each experiment, we used the measured diffusivities during the final (high temperature) retrograde heating sequence to calculate the activation energy for the mineral.

2.3 Results

The results for all experiments are compiled in Table 2.1, and are presented as separate Arrhenius plots of He diffusion in corundum (Figure 2.2), Ne diffusion in corundum (Figure 3), and Ne diffusion in hematite (Figure 2.4).

2.3.1 Helium in corundum

Figure 2.2 shows data for helium diffusion from corundum on an Arrhenius plot. The experiment was conducted from 600°C to 1150°C with two retrograde heating sequences. The sample was first heated in steps from 600°C to 850°C, then in decreasing steps from 850°C to 650°C, then in increasing steps to 1100°C, again in decreasing steps to 800°C, and finally in increasing steps to 1150°C. This sequence released 91.9% of the helium in the corundum. The data form a single linear array in the Arrhenius plot, with even the first step (0.7% yield) falling on the line, although there is some unexplained scatter throughout the array. Fractional gas yields range from 0.06% to 12.37%, with the lowest step representing 270,000 atoms, or almost four times the procedural blank. All other steps yielded over 1 million atoms.

The linear Arrhenius array produced by helium diffusion in corundum in Figure 2.2 allows for a simple determination of the diffusion kinetics. We fit all data to a single line that defines the temperature dependence of helium diffusivity in corundum. The slope of this line gives an activation energy of 1.8×10^5 J/mol, within the range of 1.6–1.9×10^5 J/mol reported for He diffusion in hematite (Farley and McKeon, 2015), although with a much lower frequency factor of $\ln(D_0/a^2) = 4.4$ $\ln(s^{-1})$ compared to the suite of values reported for polydomain hematite. This similarity is consistent with the hypothesis that mineral with the same structure exhibit similar activation energies for noble gas diffusion (Farley, 2007), which is useful for assessing the neon diffusion data in hematite and potentially for investigating the diffusion of heavy noble gases in minerals in which they cannot be directly measured

due to scarcity or difficulty of extraction (for example, if generating an Arrhenius array would require such high temperatures that the mineral would be destroyed).

2.3.2 Neon in corundum

Like helium, neon in corundum exhibits fairly simple diffusion characteristics. The Arrhenius plot (Figure 3) shows an experiment conducted from 350°C to 1200°C with two retrograde sequences. The sample was heated from 350°C to 1000°C in increasing steps, then to 700°C in decreasing steps, then again to 1200°C in increasing steps, then in decreasing steps to 1000°C. This sequence released 50.2% of the helium in the corundum. The first six steps, representing less than 3.5% of the total gas in the sample, exhibit anomalously high diffusivity, a phenomenon that has been observed in noble gas diffusion from many different mineral systems (e.g., Reiners 2005). After this, all data points fall on a single line in the Arrhenius plot. Fractional gas yields ranged from zero to 25.3%, and we excluded two steps with less than 10% of the background level of ^{21}Ne, along with a step during which temperature recording failed, making the placement on the Arrhenius plot uncertain. The Ne measured in these steps was included in the cumulative gas yields for Arrhenius calculations.

Ignoring the initial deviation from the linear Arrhenius array, the array in Figure 3 allows us to calculate the diffusion parameters for Ne diffusion in corundum. These data suggest an activation energy of $3.9(\pm 0.3) \times 10^5$ J/mol with a frequency factor of $\ln(D_0/a^2) = 19.8\ (\pm 2.4)\ \ln(s^{-1})$. Following the analogy suggested by the helium data, we can compare this to the activation energy and frequency factor for

Ne in hematite, and we find again a similar activation energy and a suite of much lower frequency factors in hematite (see below).

2.3.3 Neon in hematite

Arrhenius plots of the Ne diffusion in hematite results are shown in Figure 2.4. We prepared five experiments, two of which were abandoned before Ne measurement due to failures of the temperature control. The three successful experiments are reported here. For aliquot 1 (Figure 2.4, blue line), we conducted a rapid experiment from 449°C to 872°C with two retrograde heating sequences. The sample was dropped into the apparatus at 798°C, then heated in isothermal and decreasing steps to 449°C, then increased to 872°C in a single step, then heated in isothermal and decreasing steps to 769°C. The reason for the strange temperatures is that the actual measured temperatures are generally a few degrees lower than the setpoint due to the conservative nature of the temperature control loop, which must avoid overshoot. Almost 60% of the Ne was released in the first heating step, and subsequent heating steps showed anomalous high diffusivity before settling onto an approximately linear array. We excluded two steps with less than 10% of the background level of ^{21}Ne. Fractional gas yields on most steps were very low, ranging from zero to 1.9%. However, this experiment allowed us to establish the temperature range at which Ne diffusion occurs and to change the tuning of the temperature control loop to allow us to easily raise the temperature of the apparatus as well as lowering it.

For aliquot 2 (Figure 2.4, yellow line), we started the experiment at a much lower temperature in order to interrogate more of the Arrhenius space. This experiment

was conducted from 638°C to 907°C with many isothermal steps followed by a retrograde sequence to 784°C and then a prograde sequence to 906°C. The isothermal steps captured decreasing isothermal diffusivity, consistent with the progressive exhaustion of smaller (higher diffusivity) diffusion domains and subsequent interrogation of larger domains. The first step, at 638°C, released 22% of the Ne in the sample, and the sequence released 77% in total. Fractional gas yields ranged from zero to 8.5% after the first sample, and we excluded one step with less than 10% of the background level of ^{21}Ne. The paired retrograde and prograde sequence at the end of the experiment included eight steps showing a linear Arrhenius array.

After the first two aliquots, we tried two more experiments similar to the second one, but both failed due to problems with the temperature control apparatus that resulted in overshoots of the setpoint. We abandoned each immediately without measuring the Ne because the primary goal of the experiments was to establish the low temperature limit of Ne retention in hematite, which requires low yield initial heating steps. The fifth aliquot (Figure 2.4, red line) used a retuned temperature control loop that yielded good stability at 461°C for the first heating step, which released only 6.4% of the Ne in the hematite. After this initial step, we slowly increased the temperature to 934°C, performing several isothermal heating steps at each temperature. This experiment did not include a retrograde heating schedule, but the continuously decreasing diffusivity at each temperature demonstrates that the hematite consists of diffusion domains of varying size that are sequentially degassed in order of increasing size (and therefore decreasing apparent diffusivity) as the

experiment proceeds.

For the corundum He and Ne data, we excluded the first few low yield steps with high uncertainty and, in the case of the neon, apparently elevated diffusivities, and then calculated the activation energy and frequency factor from the remainder of the array. We calculated Ea = 1.8 (±0.08) $\times 10^5$ J/mol and $\ln(D_0/a^2)$ = 4.4 (±0.9) $\ln(s^{-1})$ for the He and Ea = 3.9 (±0.3) $\times 10^5$ J/mol and $\ln(D_0/a^2)$ = 19.8 (±2.5) $\ln(s^{-1})$ for the Ne. The uncertainties are calculated from the statistics of the linear regressions. We used the paired retrograde-prograde Arrhenius array from the second aliquot to calculate the activation energy for neon diffusion from the Caltech MI-43 hematite standard, which is Ea = 3.9 (±0.1) $\times 10^5$ J/mol. This activation energy is considerably higher than the activation energy reported by Farley and McKeon (2015) for helium diffusion in hematite, Ea = $1.6--1.9 \times 10^5$ J/mol, as expected for volume diffusion of a larger atom through the same crystal structure. We used the lowest yield initial step from the fifth aliquot to calculate the frequency factor for the least retentive fraction of the hematite, which is $\ln(D_0/a^2)$ = 49.3 $\ln(s^{-1})$. This value is the most important point for demonstrating the utility of hematite (U–Th)/Ne as a geochronometer, because it shows the conditions under which the most loosely retained Ne is lost to thermal diffusion in the poly-diffusion domain system. However, because the domain structure of hematite will vary between samples, this number applies to this particular hematite only.

2.4 Discussion

The diffusion measurements described above are relevant to the value of the hematite (U–Th)/He system as both a geochronometer, meaning a tool used to date the formation age of a rock, and a thermochronometer, meaning a tool used to probe the post-formation thermal history of a rock. For a given mineral, the distinction is related to the degree of heating experienced after formation; if the heating is significant enough to cause diffusive loss of the daughter product in the dating scheme (Ne in this case), the system serves only as a thermochronometer. Establishing a system as a geochronometer requires demonstrating that it has retained the daughter product quantitatively since formation, while establishing it as a thermochronometer requires measuring the diffusive response of the daughter product to thermal perturbation.

2.4.1 Polydomain Ne diffusion in hematite and (U–Th)/Ne geochronometry

The diffusivities in Figure 2.4 show that Ne diffusion in hematite is not a simple function of temperature as would be expected for single domain diffusion following the Arrhenius relationship. Like He diffusion in hematite (Farley and McKeon, 2015), Ne diffusion appears to fit a polydomain diffusion model, with the domains likely related to the small crystallites and fast diffusion pathways between crystallites of varying size that comprise the hematite. Retrograde step heating experiments and isothermal step heating experiments both show that the apparent diffusivity changes in an organized way, decreasing during the course of the experiment at a given temperature as the smaller domains are exhausted of their Ne and the larger,

more retentive domains become the dominant contributors to the measured gas in each step. The experiments also show that, toward the end of the experiment, a paired prograde-retrograde heating experiment yields a linear relationship between $\ln(D/a^2)$ and 1/T, indicating that these steps consist of gas from a set of domains of similar size, which follow the Arrhenius relationship .

The difficulty of obtaining a high-resolution Arrhenius array with a low abundance gas such as Ne in hematite means that the matched prograde-retrograde array that we use to calculate the activation energy for Ne diffusion contains fewer points than that used for He. However, we see several key differences. For example, the He diffusion data presented by Farley and McKeon (2015) shows a different domain structure in the low gas yield portion of the experiment, which can be probed more easily by measuring ^{3}He than by measuring ^{21}Ne; we were able to measure only a single step as low as 6%, while the He diffusion experiments included several steps at yields less than 1%. This difference can be seen in the $\ln(r/r_0)$ plots for our diffusion experiments (Lovera et al. 1991; Figure 2.5), which shift toward a plateau at around 10% gas yield, compared to around 30% in the He experiments. The Ne diffusion experiments on aliquots 2 and 5, which have better resolution at low gas yield than the experiment on aliquot 1, are also offset from one another by about the same amount that aliquot 2 is offset from the He data, and the reasons for this offset are not known.

The key to determining the viability of the (U–Th)/Ne geochronometer is to probe the smallest, least retentive domains in the mineral. We designed the experiment

on aliquot 5 to address this, and we measured $\ln(D/a^2)$ = -15.5 ln(s−1) for a heating step that yielded 6% of the Ne in the mineral. Using the activation energy that we determined on the high temperature array, we determine a frequency factor of $\ln(D_0/a^2)$ = 49.3 $\ln(s^{-1})$ for this step, which allows us to calculate a closure temperature of 299°C (-8/+17°C) assuming a cooling rate of 10°C/Ma (Dodson, 1973). This minimum closure temperature applies to the most retentive 94% of the Ne in the hematite; the vast majority of the Ne has a higher closure temperature, and the least retentive 6% will have a range of lower closure temperatures depending on the domain structure of the mineral.

2.4.2 Hematite (U–Th)/Ne thermochronometry

We have established the conditions under which the MI-43 hematite (U–Th)/Ne system can be used as a geochronometer, but it can also potentially be a thermochronometer. Most common thermochronometers have a single closure temperature, which is just an approximate temperature at which the system closes to diffusion given typical crustal cooling rates. Poly-diffusion domain systems do not have a single closure temperature; instead, larger domains will lose gas more slowly at a given temperature, so the larger domains in a poly-domain mineral effectively have higher closure temperatures than the smaller domains. Minerals such as hematite have a broad range of domains of different sizes, but the overall structure can be sampled approximately with a diffusion experiment of the type shown in Figure 2.4. The measured diffusivity is a minimum for a given heating step, so the remaining fraction of the gas has a closure temperature at least as high as the value

one would calculate using the frequency factor measured at that step.

A poly-diffusion domain thermochronometer has a larger range of temperature sensitivity than traditional thermochronometers because of the wide range of effective diffusivities produced by the range of domain sizes. The domain structure of hematite is sample-dependent, so a diffusion experiment is required for each sample that will be used as a thermochronometer. This presents a problem for hematite (U–Th)/Ne thermochronometry because of the difficulty of producing synthetic Ne in hematite. If some of the Ne has been lost to diffusion, one cannot use this Ne itself to interrogate the domain structure. Fortunately, it is easy to produce artificial He in hematite using proton irradiation (Farley and Flowers, 2012; Farley and McKeon, 2015), so one can interrogate the domain structure in any sample this way and then use our Ne diffusivity data to convert this domain structure into thermal history information. Doing so requires that we establish a relationship between He and Ne diffusivity, which requires that we determine which domains are related to one another in the He and Ne diffusion experiments. As mentioned above, however, our apparent domain structure differs in the low temperature regime from that measured for He diffusion by Farley and McKeon (2015); we take the average value of the He and Ne apparent domain sizes at 40% gas yield, where the structure of the plots is similar, and assert that the domain size is the same at this point. Given the offset between the Ne experiments, the higher resolution of the ^{3}He diffusion experiments, and the simpler history of the synthetic ^{3}He, we choose to assert the domain structure measured using the He diffusion experiment to use these data for

thermochronometry. Using the match at 40% gas yield, we can shift the Ne domains onto the same scale as the He data. At this point, the He $\ln(D_0/a^2) = 13.6\ \ln(s^{-1})$ and the Ne $\ln(D_0/a^2) = 32.9\ \ln(s^{-1})$. If we take the difference of these, we see that the frequency factor for Ne diffusion is 19.3 $\ln(s^{-1})$ higher than that for He diffusion. We can then scale the results of a ^{3}He diffusion experiment to create an artificial isotope of Ne, which we call ^{A}Ne, and which we can use the same way that ^{3}He is used in ^{4}He/^{3}He experiments (Shuster et al., 2005). Determining the thermal history of a sample using this information is not as straightforward as it is in single domain ^{4}He/^{3}He experiments because this does not provide a unique solution; rather, it will require more knowledge about the geologic context of a sample.

As an example, we show model data in Figure 2.6 for a 1000 Ma hematite sample that experienced a significant thermal event. This is not a general result because it depends on the domain structure of mineral, but the same approach could be applied to other samples and other minerals. U and Th, and therefore He and Ne, are distributed evenly throughout the polycrystalline mineral, which we have sampled internally so that there is no ejection loss. We irradiate the sample with protons and then conduct a diffusion experiment and measure ^{3}He, ^{4}He, and ^{21}Ne. By creating a plot of $\ln(r/r_0)$ using the ^{3}He data, we can probe the domain structure of the hematite, which matches the model input (Figure 2.6a). The constant isotope ratio measured in the ^{3}He and ^{4}He experiments (Figure 2.6b) shows that the sample underwent a rapid reheating event that completely degassed its helium, and the (U–Th)/He age of the sample gives the date of this event as 100 Ma. Simply measuring a (U–Th)/Ne

age would yield a meaningless result of 440 Ma because the sample lost two-thirds of its Ne during the reheating event. By applying the transformation suggested above to the ^{3}He diffusion experiment (Figure 2.6c), however, we can create the uniformly distributed artificial Ne isotope (^{A}Ne) that we need to look at Ne loss in the ^{21}Ne diffusion experiment (Figure 2.6d). If we then calculate the ratio of ^{A}Ne to nucleogenic ^{21}Ne, normalized to the largest domain size, as a function of cumulative gas yield, we can see clearly that ^{21}Ne has been lost to smaller domains as a result of the reheating event. We can compare this profile to simulations of reheating events of different duration or temperature to constrain the reheating temperature, which in this case matches the model input of 400°C for 1 million years; however, this solution is not unique, so we must make assumptions based on context or apply other information about the temperature or duration of reheating (Figure 2.6e).

2.4.3 Ionic Porosity Model

The suggestion that the same gas diffuses with similar activation energies in minerals with the same structure but different chemistry is based on an ionic porosity model and was illustrated using zircon- and monazite-structure phosphate minerals by Farley (2007). This model simply involves using the ionic spacing in the crystal lattice to predict differences in diffusivity between materials; previous work had suggested that this might be a primary control on diffusivity in minerals (Fortier and Giletti, 1989; Dahl, 1996; Zhao and Zheng, 2007), but Farley (2007) found that ionic porosity only correlated strongly with diffusivity after controlling for mineral structure, which was far more important. Fortier and Giletti (1989) and Dahl (1996)

found scaling effects on both activation energy and frequency factor for Ar diffusion in a large suite of minerals (micas did not follow the law). Farley (2007) found changes in frequency factor, but not in activation energy, between minerals with similar structures but different chemical compositions and therefore ionic spacing. The eleven zircon-structure phosphate minerals investigated, for example, showed activation energies ranging from $1.10 \times 10^5(\pm 3)$ J/mol to $1.28 \times 10^5(\pm 4)$ J/mol, with frequency factors ranging from is $\ln(D_0) = 12.9$ $\ln(cm^2s^{-1})$ to $\ln(D_0) = 3.57$ $\ln(cm^2s^{-1})$. The ionic porosities ranged from 33.1% to 30%, and both frequency factor and closure temperature correlated well (but not perfectly) with ionic porosity. The correlation is less strong for the monazite structure minerals, however, and the synthetic and natural minerals discussed by the paper follow different trends. For example, an extrapolation of the fit between ionic porosity and closure temperature for these synthetic phosphates leads to a closure temperature almost 200°C too low for zircon itself, and the paper discusses evidence that some natural minerals have higher activation energies and closure temperatures than the synthetic analogs, perhaps because of radiation damage or small structural differences.

Total ionic porosity is defined as the percentage of a mineral's unit cell volume that is not occupied by ions, following the equation Z = 100 x (1 - V_I/V_C), where V_I is the total volume of ions in the unit cell and V_C is the total volume of the unit cell (Zhao and Zheng, 2007). The unit cell of hematite has a volume of 3.03×10^{-28} m^3 with six formula units per cell , meaning it has twelve iron ions and eighteen oxygen ions. The iron is ferric (Fe^{3+}) and, at pressures near the Earth's surface, is

in the high-spin state. Using the "crystal" ionic radii from Shannon (1976), the iron ions have a radius of 78.5 pm and the oxygen ions have a radius of 126 pm. The volume of ions in the hematite unit cell is, therefore, 2.19×10^{-29} m^3, yielding an ionic porosity of 27.7%. The unit cell of corundum has a volume of 2.54×10^{-28} m^3 with twelve aluminum ions and eighteen oxygen ions . Following the same approach as above, the aluminum ions have a radius of 67.5 pm, the volume of ions is 2.08×10^{-29} m^3, and the ionic porosity is only 18.1%. Like the zircon-structure phosphates investigated in Farley (2007), hematite and corundum have highly anisotropic crystal structures.

We can use this information to assess the data presented here in two different ways. First, we can use the He diffusion data in corundum and hematite to predict a scaling factor for Ne diffusion in corundum and hematite, then use the diffusion data for Ne diffusion in corundum to predict the more complicated diffusivities in hematite. We do not know the absolute size of the diffusion domains observed for He diffusion in hematite (Farley and McKeon, 2015), so the scaling factor itself is arbitrary, but we can create a prediction of apparent Ne diffusivity $\ln(D_0/a^2)$ that will have same domain structure as the He data used to generate it. For example, we simply consider the point at which 40% of the gas (He or Ne) is released from the hematite and we observe that measured $\ln(D_0/a^2)$ = 19.9 $\ln(s^{-1})$ from MI-43-d1 in Farley and McKeon (2015). We can then calculate the actual value of $\ln(D_0)$ = -9.46 $\ln(m^2s^{-1})$ for He diffusion in corundum from the measured $\ln(D_0/a^2)$ = 4.35 $\ln(s^{-1})$ and the known crystal fragment radius of 1 mm. Coupled with the difference in

ionic porosity (9.6%), we can assert an artificial scaling factor of 3.05 $\ln(D_0)$ per % ionic porosity between corundum and the arbitrarily chosen 40% gas release point for the MI-43 hematite.

We can then attempt to apply this scaling to the Ne diffusion data. We cannot use the compensation laws between activation energy and frequency factor used by Zhao and Zheng (2007) because Farley (2007) showed that these are not correct in detail. Instead, we can assume that the activation energy is the same for these isostructural minerals, then we apply the scaling factor of 3.05 $\ln(D_0)$ per % ionic porosity to the value of $\ln(D_0) = 5.97$ $\ln(m^2s^{-1})$ that we calculate for Ne diffusion in corundum from the measured $\ln(D_0/a^2) = 19.8$ $\ln(s^{-1})$ and the known crystal fragment radius of 1 mm. We can rescale this to a predicted value for Ne diffusion in the MI-43 hematite at 40% gas yield of $\ln(D_0/a^2) = 23.4$ $\ln(s^{-1})$. The measured value is between $\ln(D_0/a^2) = 30.8$ $\ln(s^{-1})$ for aliquot 5 and $\ln(D_0/a^2) = 33.5$ $\ln(s^{-1})$ for aliquot 2, so the scaling factor for Ne and He may be slightly different. However, considering the offset between the two aliquots and the lack of resolution in the Ne diffusion data, this difference is small.

The second way that we can use ionic porosity and our diffusion data is to take advantage of the fact that we were able to measure He and Ne diffusivity in each mineral and to interrogate the different scaling factors for diffusivity for each gas. Zhao and Zheng (2007) used scaling laws for both activation energy and frequency factor and showed different scaling laws for different elements, with the slope of the scaling law between both activation energy and frequency factor

and ionic porosity being significantly higher for argon than for hydrogen, lead, or strontium. This is not necessarily surprising, as noble gas diffusion through a crystal structure is fundamentally different than diffusion of most other elements, but the fact that Fortier and Giletti (1989) and Farley (2007) found different scaling laws for noble gas diffusion in different minerals (and no relationship in others) suggests the possibility that different scaling laws might exist for different gases in the same mineral.

Our data indicate that, like the zircon-structure phosphates of Farley (2007), isostructural corundum and hematite have similar activation energies. We measure the same activation energy for Ne diffusion in corundum and hematite, and an activation energy for He diffusion in hematite that falls in the range measured by Farley and McKeon (2015). As stated above, we find a scaling factor of 3.05 $\ln(D_0)$ per % ionic porosity for He diffusion between corundum and an arbitrary domain size in hematite, but this factor predicts a low frequency factor for Ne diffusion in hematite when we use it to scale the data for corundum. Instead, we find a factor of between 3.83 and 4.11 $\ln(D_0)$ per % ionic porosity for Ne diffusion. The absolute value of these factors is arbitrary because we do not know the hematite domain size, but the relationship that the scaling factor for Ne is 0.78-1.06 higher than that for He is a result that could be used to predict Ne diffusion for other minerals.

2.4.4 Comparison to computation models

Recently, Balout, Roques, Gautheron, Tassan-Got, and Mbongo-Djimbi (2017) published a model of He diffusion in hematite that matched the Farley and McKeon

(2015) activation energy very well. The companion paper looking at Ne diffusion finds an activation energy for Ne diffusion in hematite that is significantly lower than that we observe—just 2.32×10^5 J/mol (Balout, Roques, Gautheron, and Tassan-Got, 2017). Both results suggest significant retention of Ne at near surface conditions, and it is difficult to compare them directly given that we do not know the absolute sizes of the diffusion domains measured in this paper. However, considering the grain size we used for these experiments and the range of domain sizes observed in both the He diffusion data (Farley and McKeon, 2015) and in this paper, it seems likely that the closure temperature of 297°C observed by Balout, Roques, Gautheron, and Tassan-Got (2017) for a domain size of 1 μm corresponds to a smaller apparent domain size in our data, and that domains smaller than 0.01 μm retained both He and Ne in hematite despite heating in the 100°C -200°C range (Farley and Flowers, 2012; Farley and McKeon, 2015).

2.5 Conclusions

The hematite (U–Th)/Ne system is a useful geochronometer for dating large iron oxide deposits that are difficult to date using established techniques. We demonstrate that this geochronometer is robust to thermal resetting at temperatures in excess of 290°C in our MI-43 standard, which means that it is insensitive to most surface processes. In addition, we show that Ne in polycrystalline hematite exhibits polydomain diffusion behavior in the same manner as He. The large size distribution of diffusion domains in polycrystalline hematite provides thermal sensitivity throughout much of the mid-crustal regime, as Ne will be progressively

lost due to thermal events from about 300°C to over 500°C. Compared to single crystal corundum, which has the same structure as hematite, we find evidence that hematite He and Ne diffusion have similar activation energies, and that there is a correlation between ionic porosity and noble gas retention in these minerals.

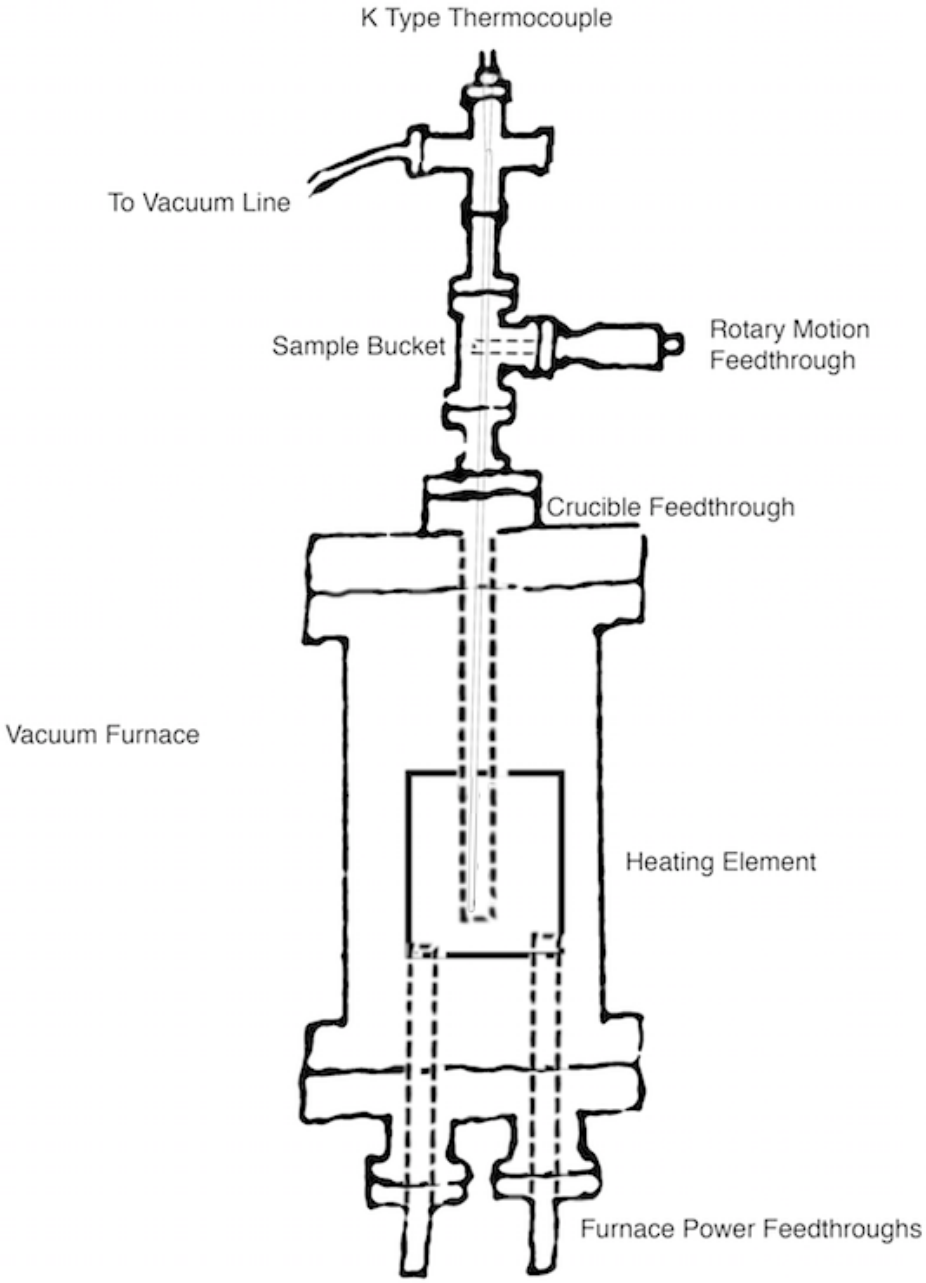

Figure 2.1: The large diffusion cell apparatus that we used for Ne diffusion experiments on hematite. The sample is introduced through a sample bucket attached to a rotary motion feedthrough, which allows the furnace to be degassed before introduction. Temperature is measured at the sample with a K type thermocouple enclosed in a long ceramic tube. The crucible and furnace assembly is a typical double vacuum furnace. We developed custom software to monitor the temperature of the sample and adjust the heating element to change and maintain temperature without overshoot.

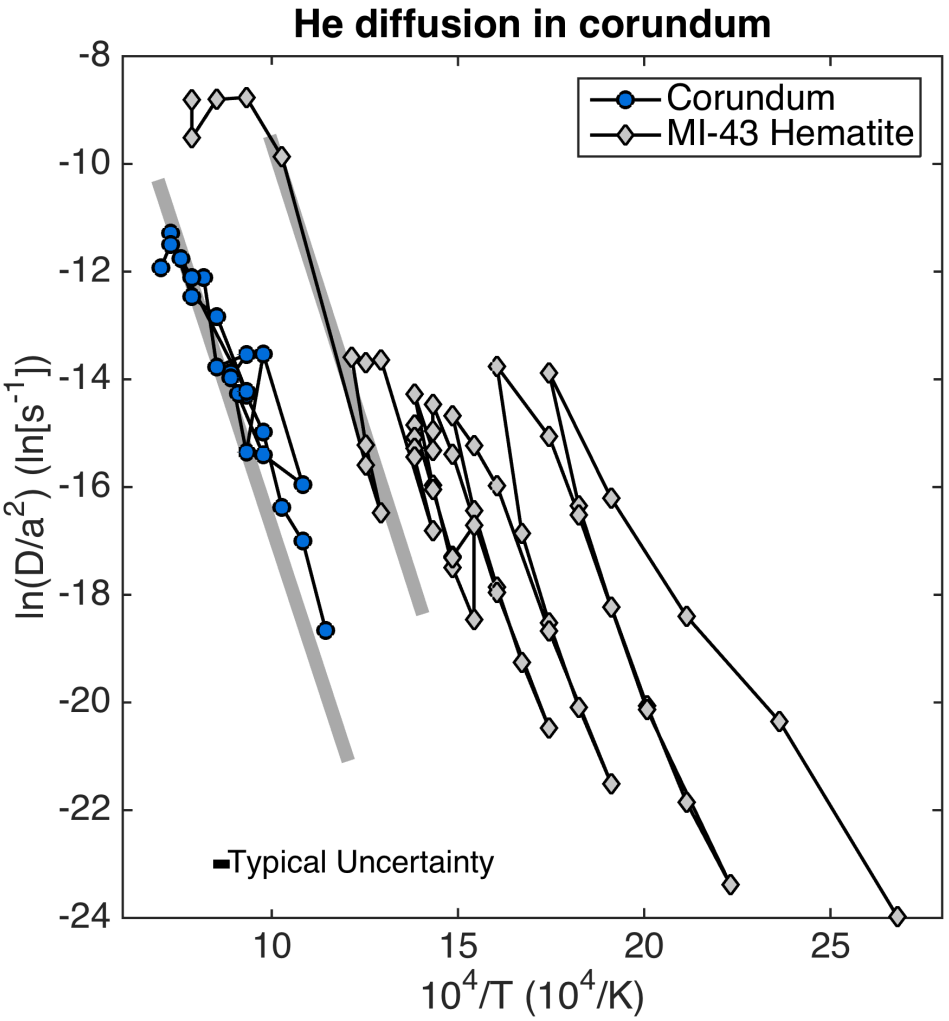

Figure 2.2: A comparison of helium diffusivity in a single grain of gem-quality corundum (blue symbols) and in MI-43 hematite (Farley and McKeon, 2015) . The activation energy for the high temperature arrays shown for each is Ea= 1.8×10^5 J/mol. The apparent activation energies from the retrograde portions of the He diffusion data vary from 1.4×10^5 to 2.4×10^5, with the corundum activation energy in the middle.

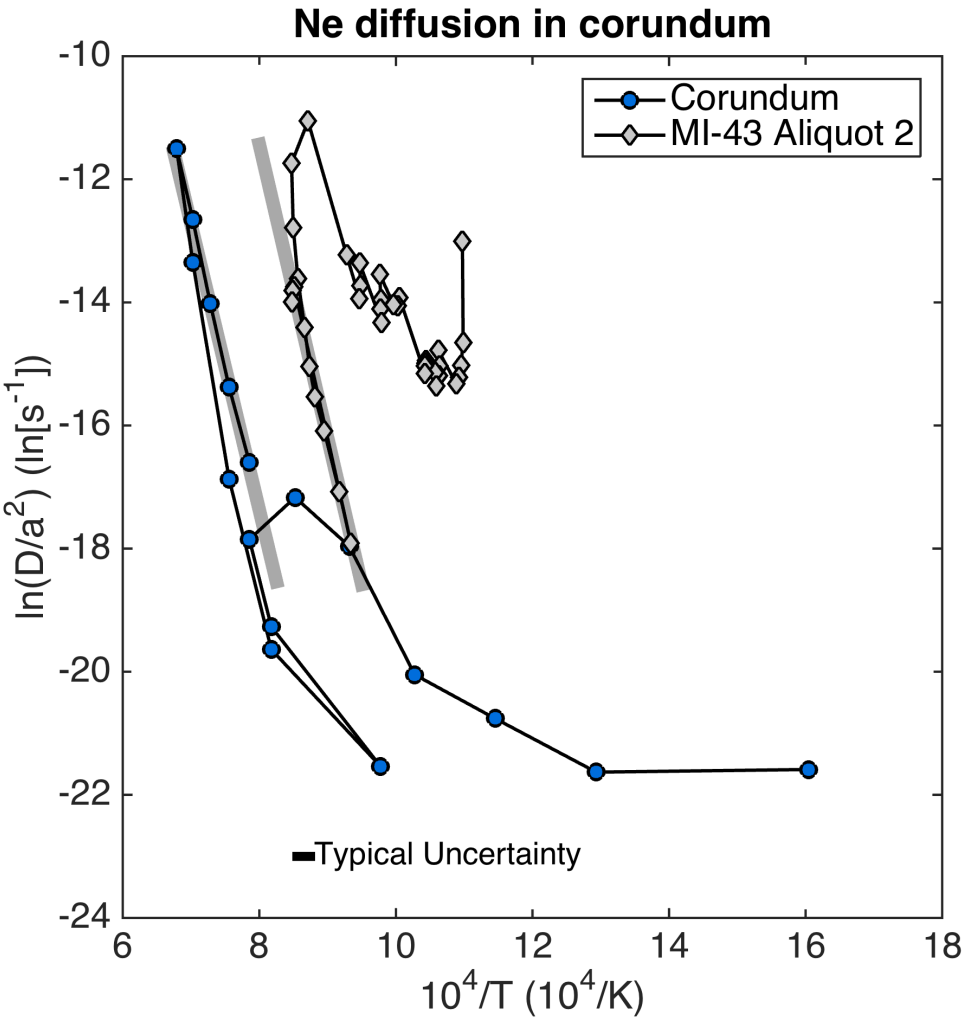

Figure 2.3: A comparison of neon diffusivity in a single grain of gem-quality corundum (blue symbols) and in MI-43 Sample 2. The activation energy for the high temperature arrays shown for each is Ea= 3.9×10^5 J/mol.

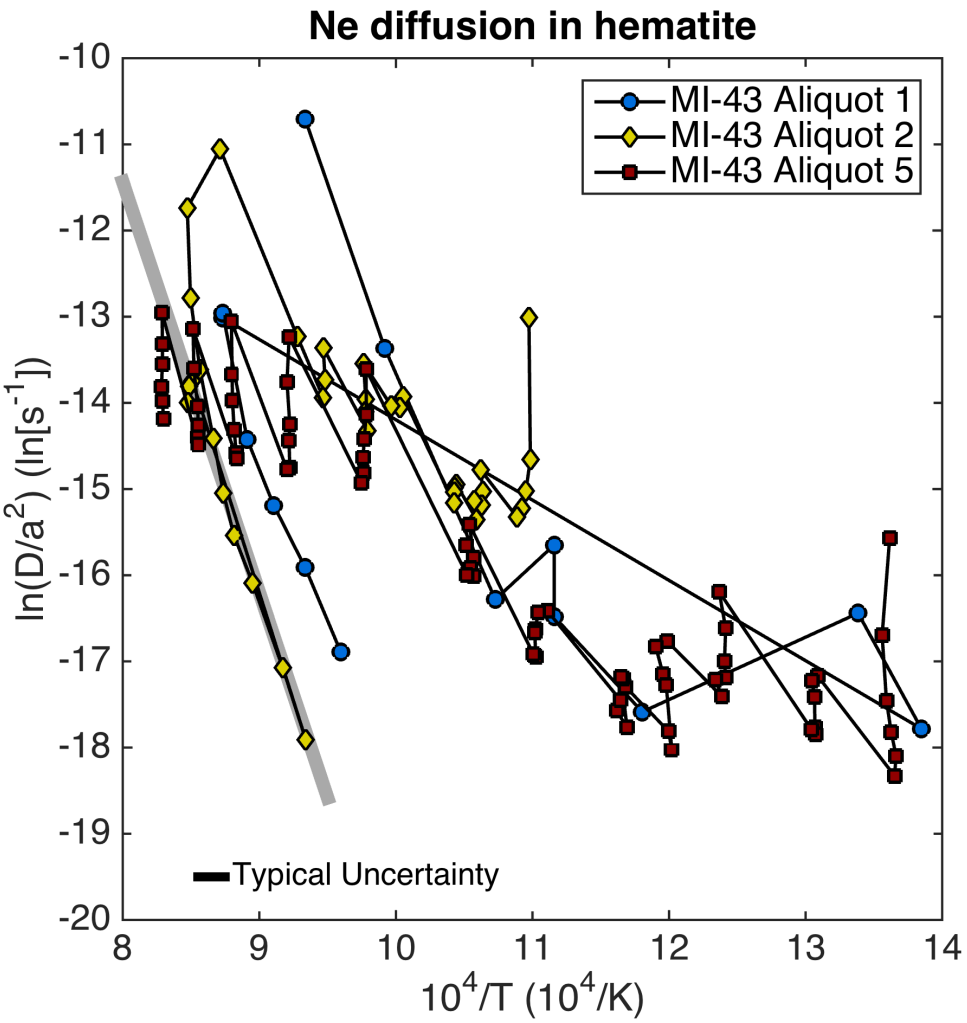

Figure 2.4: Neon diffusivity as a function of inverse temperature for three aliquots of the MI-43 hematite standard measured using the big diffusion cell apparatus. The difference in path followed by each sample is a function of the heating schedule. The fit to the high temperature array for aliquot 2 shown has the activation energy Ea= 3.9×10^5 J/mol.

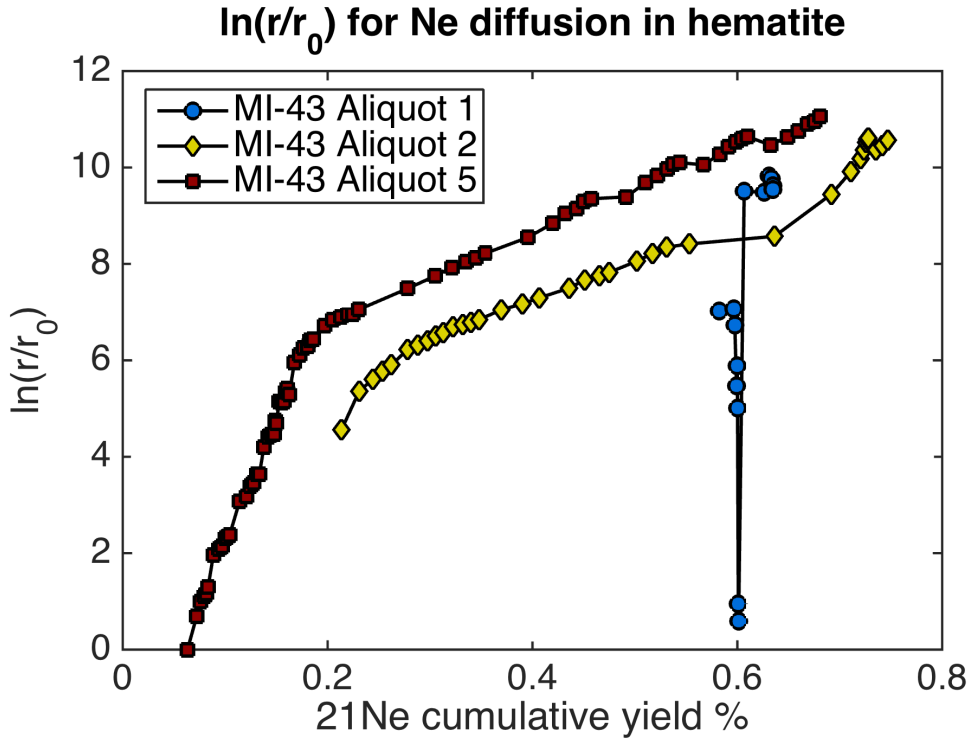

Figure 2.5: A plot of the logarithm of the ratio of the apparent domain size (assuming uniform diffusivity) for each temperature step for the three MI-43 experiments shown in Figure 2.4, following Lovera et al. (1991). The smallest domain size r_0 is simply fixed at the smallest apparent domain size sampled, which is the first heating step for aliquot 5. The offset between the samples is discussed in the text.

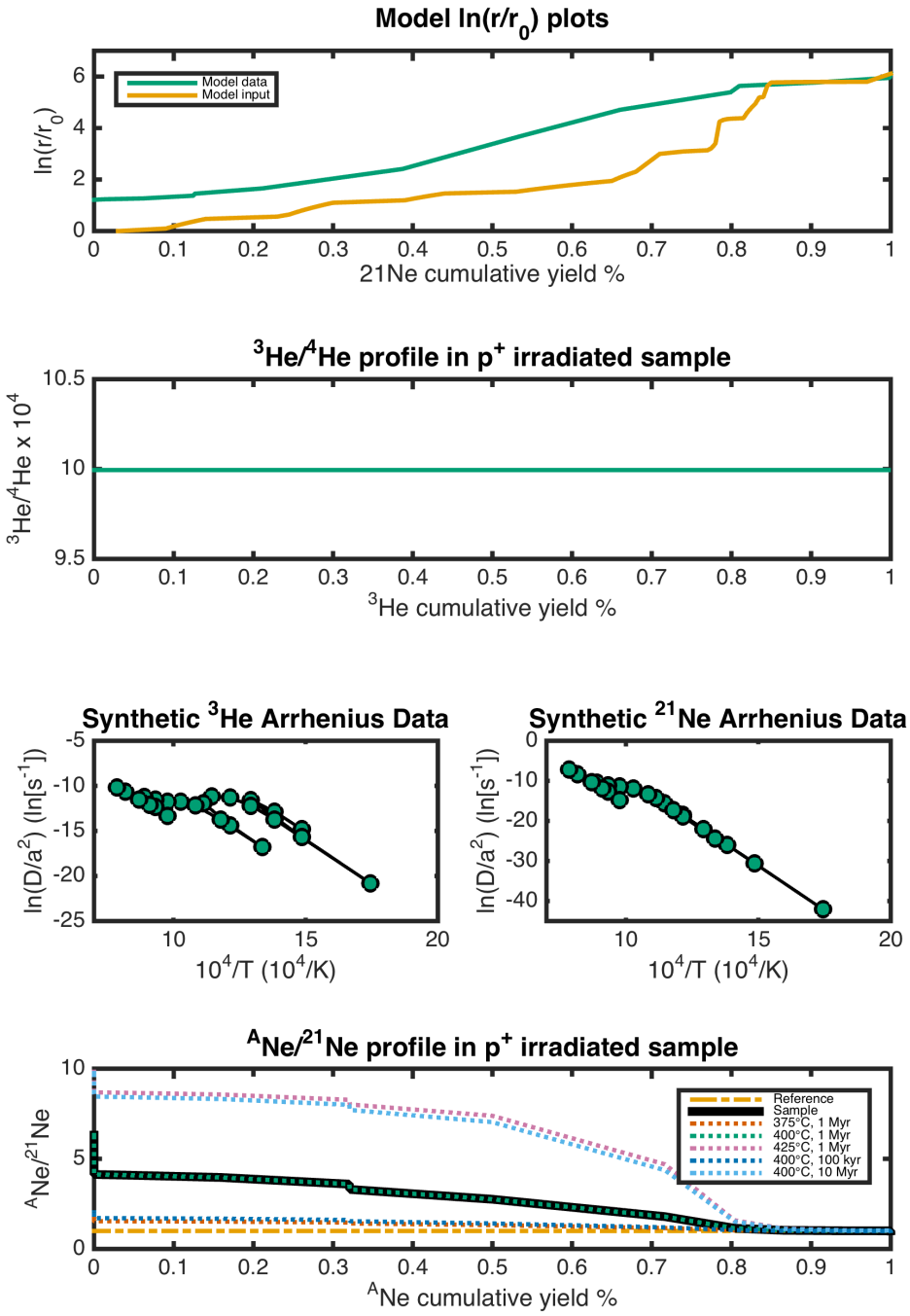

Figure 2.6: Model run showing the transformation of simulated ^{3}He diffusion domains into ^{21}Ne domains. (a) The input domains are plotted on an ln(r/r$_0$) and compared to the calculated domains from the diffusion data. (b) The ^{3}He/^{4}He for the sample after proton irradiation showing no ^{4}He retained from before the reheating event. (c,d) The calculated ^{3}He and ^{21}Ne Arrhenius plots showing polydomain diffusion behavior. (e) The ratio of artificial isotope ^{A}Ne, created by scaling the ^{3}He diffusion data, to ^{21}Ne in the heated sample, as a function of cumulative ^{A}Ne. This shows the effect of the reheating event on the ^{21}Ne distribution in the polydomain system, and shows the strength and shortcomings of the model in resolving unique reheating histories.

Table 2.1: All results from He and Ne diffusion experiments.

MI-43 aliquot 1 (1277 mg)	1	798	33.4	3.34E+08	-10.7	58.2%
	2	735	31.4	8.24E+06	-13.4	59.7%
	3	659	32.4	4.49E+05	-16.3	59.8%
	4	623	41.1	2.78E+04	*	59.8%
	5	623	36.1	9.36E+05	-15.6	59.9%
	6	623	41.1	4.62E+05	-16.5	60.0%
	7	574	36.3	1.35E+05	-17.6	60.0%
	8	528	41.1	-5.48E+03	*	60.0%
	9	474	36.1	4.21E+05	-16.4	60.1%
	10	449	61.4	1.87E+05	-17.8	60.1%
	11	872	8.8	3.13E+06	-13.0	60.7%
	12	872	31.4	1.12E+07	-13.0	62.6%
	13	849	32.4	2.57E+06	-14.4	63.1%
	14	825	41.1	1.49E+06	-15.2	63.3%
	15	798	36.2	6.35E+05	-15.9	63.4%
	16	769	41.1	2.70E+05	-16.9	63.5%
	1	638	33.4	1.52E+08	-13.0	21.9%
	2	637	31.4	1.23E+07	-14.6	23.6%
	3	640	37.6	9.40E+06	-15.0	25.0%
	4	642	36.8	7.11E+06	-15.2	26.0%

Sample	Step	Temperature (°C)	Time (min-utes)	^{21}Ne* atoms	ln(D)	Fcum
	5	645	36.1	5.99E+06	-15.3	26.9%
	6	668	41.2	1.12E+07	-14.7	28.5%
	7	667	36.2	7.15E+06	-15.0	29.5%
	8	668	41.1	6.66E+06	-15.1	30.5%
	9	673	36.2	5.91E+06	-15.1	31.3%
	10	671	41.1	5.23E+06	-15.3	32.1%
	11	684	36.2	6.68E+06	-14.9	33.0%
	12	685	41.1	6.99E+06	-14.9	34.0%
	13	686	36.2	5.65E+06	-15.0	34.9%
	14	686	41.1	5.49E+06	-15.1	35.6%
	15	722	36.2	1.56E+07	-13.9	37.9%
	16	724	41.1	1.43E+07	-14.0	40.0%
	17	730	36.2	1.20E+07	-14.0	41.7%
	18	751	41.1	2.05E+07	-13.5	44.6%
	19	749	36.2	1.10E+07	-13.9	46.2%
	20	750	41.1	1.02E+07	-14.0	47.7%
	21	748	36.2	6.90E+06	-14.3	48.7%
	22	783	41.1	1.92E+07	-13.3	51.4%
	23	782	36.2	1.08E+07	-13.7	53.0%

Sample	Step	Temperature (°C)	Time (min-utes)	^{21}Ne* atoms	ln(D)	Fcum
	24	783	41.2	9.56E+06	-13.9	54.4%
	25	805	36.1	1.59E+07	-13.2	56.7%
	26	875	18.4	5.93E+07	-11.0	65.2%
	27	907	31.4	3.95E+07	-11.7	70.9%
	28	904	35.9	1.37E+07	-12.7	72.9%
	29	894	41.3	6.48E+06	-13.5	73.8%
	30	881	36.2	2.50E+06	-14.3	74.1%
	31	871	41.3	1.49E+06	-14.9	74.4%
	32	861	36.2	7.96E+05	-15.4	74.5%
	33	844	41.3	5.19E+05	-16.0	74.6%
	34	817	36.2	1.70E+05	-17.0	74.6%
	35	797	41.2	8.38E+04	-17.8	74.6%
	36	784	36.3	2.42E+04	*	74.6%
	37	902	41.2	5.29E+06	-13.6	75.3%
	38	905	36.2	4.26E+06	-13.7	76.0%
	39	906	41.2	3.91E+06	-13.9	76.5%

Sample	Step	Temperature (°C)	Time (min-utes)	^{21}Ne* atoms	ln(D)	Fcum
	1	461	33.4	3.52E+07	-15.5	6.5%
	2	464	31.4	5.00E+06	-16.6	7.4%
	3	463	32.6	2.21E+06	-17.4	7.8%
	4	461	41.1	1.84E+06	-17.8	8.1%
	5	459	36.1	1.19E+06	-18.0	8.4%
	6	459	41.1	1.05E+06	-18.3	8.5%
	7	491	36.2	2.82E+06	-17.1	9.1%
	8	493	41.1	2.87E+06	-17.2	9.6%
	9	492	36.2	2.00E+06	-17.4	10.0%
	10	492	41.1	1.54E+06	-17.6	10.2%
	11	492	36.2	1.12E+06	-17.8	10.4%
	12	494	41.1	1.32E+06	-17.7	10.7%
	13	535	36.2	5.39E+06	-16.1	11.7%
	14	532	41.1	3.70E+06	-16.6	12.4%
	15	533	36.2	2.12E+06	-16.9	12.8%
	16	532	41.1	1.92E+06	-17.1	13.1%
	17	537	36.1	1.61E+06	-17.2	13.4%
	18	534	41.2	1.48E+06	-17.4	13.7%
	19	561	36.2	2.39E+06	-16.7	14.1%

Sample	Step	Temperature (°C)	Time (min-utes)	^{21}Ne* atoms	ln(D)	Fcum
	20	567	41.1	2.46E+06	-16.8	14.6%
	21	563	36.2	1.53E+06	-17.1	14.8%
	22	562	41.1	1.50E+06	-17.2	15.1%
	23	559	36.1	6.14E+05	-18.0	15.2%
	24	560	41.1	8.54E+05	-17.8	15.4%
	25	583	36.2	1.24E+06	-17.2	15.6%
	26	584	41.1	1.52E+06	-17.1	15.9%
	27	585	36.1	1.34E+06	-17.1	16.1%
	28	582	41.1	8.36E+05	-17.7	16.3%
	29	588	36.2	8.86E+05	-17.5	16.5%
	30	586	41.1	1.12E+06	-17.4	16.7%
	31	627	36.2	2.71E+06	-16.4	17.2%
	32	632	41.0	2.92E+06	-16.4	17.7%
	33	634	36.2	2.06E+06	-16.6	18.1%
	34	635	41.1	2.19E+06	-16.6	18.5%
	35	634	36.1	1.42E+06	-16.9	18.7%
	36	635	41.1	1.64E+06	-16.9	19.0%
	37	676	36.2	6.21E+06	-15.4	20.2%
	38	673	41.1	4.52E+06	-15.7	21.0%

Sample	Step	Temperature (°C)	Time (min-utes)	^{21}Ne* atoms	ln(D)	Fcum
	39	678	36.2	4.41E+06	-15.6	21.8%
	40	675	41.1	3.69E+06	-15.9	22.5%
	41	673	36.1	2.84E+06	-16.0	23.0%
	42	677	41.1	3.20E+06	-15.9	23.6%
	43	749	36.2	2.66E+07	-13.6	28.5%
	44	749	41.0	1.49E+07	-14.1	31.3%
	45	751	36.2	9.04E+06	-14.4	32.9%
	46	751	41.1	7.77E+06	-14.6	34.3%
	47	751	36.2	5.43E+06	-14.8	35.3%
	48	753	41.0	5.29E+06	-14.9	36.3%
	49	812	36.2	2.29E+07	-13.2	40.5%
	50	814	41.1	1.36E+07	-13.7	43.0%
	51	811	36.2	6.87E+06	-14.2	44.3%
	52	812	41.1	6.15E+06	-14.4	45.4%
	53	811	36.2	3.84E+06	-14.7	46.1%
	54	814	41.1	4.16E+06	-14.7	46.9%
	55	864	36.1	1.89E+07	-13.0	50.4%
	56	863	41.1	1.06E+07	-13.6	52.3%
	57	863	36.2	6.52E+06	-13.9	53.5%

Sample	Step	Temperature (°C)	Time (min-utes)	^{21}Ne* atoms	ln(D)	Fcum
	58	861	41.1	5.09E+06	-14.2	54.4%
	59	859	36.2	3.33E+06	-14.5	55.1%
	60	859	41.1	3.46E+06	-14.6	55.7%
	61	901	36.2	1.30E+07	-13.1	58.1%
	62	900	41.1	8.74E+06	-13.5	59.7%
	63	897	36.2	4.74E+06	-14.0	60.6%
	64	896	41.1	4.20E+06	-14.2	61.3%
	65	896	36.2	3.15E+06	-14.3	61.9%
	66	896	41.1	3.23E+06	-14.4	62.5%
	67	933	36.2	1.24E+07	-12.9	64.8%
	68	933	41.0	9.11E+06	-13.2	66.5%
	69	933	36.2	6.07E+06	-13.5	67.6%
	70	934	41.1	5.10E+06	-13.7	68.5%
	71	933	36.2	3.70E+06	-13.9	69.2%
	72	932	37.6	3.04E+06	-14.1	69.8%
(neon)	1	350	30.0	7.61E+05	-21.6	0.3%
	2	500	30.0	3.04E+05	-21.6	0.4%

Sample	Step	Temperature (°C)	Time (min-utes)	^{21}Ne* atoms	ln(D)	Fcum
	3	600	30.0	5.04E+05	-20.8	0.6%
	4	700	30.0	7.04E+05	-20.0	0.9%
	5	800	30.0	2.92E+06	-18.0	2.0%
	6	900	30.0	3.48E+06	-17.2	3.4%
	7	1000	30.0	1.31E+06	-17.8	3.9%
	8	950	30.0	2.91E+05	-19.3	4.0%
	9	850	30.0	0.00E+00		4.0%
	10	750	30.0	2.97E+04	-21.5	4.0%
	11	700	30.0	0.00E+00	*	4.0%
	12	750	30.0	0.00E+00	*	4.0%
	13	**	**	4.29E+04	**	4.0%
	14	950	30.0	1.95E+05	-19.6	4.1%
	15	1050	30.0	2.73E+06	-16.9	5.1%
	16	1150	30.0	3.30E+07	-13.4	17.9%
	17	1200	30.0	6.49E+07	-11.5	43.0%
	18	1150	30.0	1.17E+07	-12.7	47.5%
	19	1100	30.0	2.72E+06	-14.0	48.6%
	20	1050	30.0	6.82E+05	-15.4	48.9%
	21	1000	30.0	2.00E+05	-16.6	48.9%

Sample	Step	Temperature (°C)	Time (min-utes)	^{21}Ne* atoms	ln(D)	Fcum
(helium)	1	600	60.0	2.95E+06	-20.6	0.7%
	2	600	60.0	1.24E+06	-20.6	1.0%
	3	650	60.0	4.68E+06	-18.6	2.1%
	4	700	60.0	1.43E+07	-16.6	5.4%
	5	750	60.0	1.52E+07	-15.9	9.0%
	6	800	60.0	2.30E+07	-14.9	14.4%
	7	825	60.0	1.70E+07	-14.8	18.3%
	8	850	60.0	1.59E+07	-14.6	22.1%
	9	800	60.0	6.84E+06	-15.3	23.7%
Corundum	10	750	60.0	1.52E+07	-14.4	27.2%
	11	700	180.0	2.00E+06	-17.4	27.7%
	12	650	180.0	2.69E+05	-19.4	27.7%
	13	750	180.0	8.19E+06	-16.0	29.7%
	14	850	180.0	5.29E+07	-13.8	42.0%
	15	800	180.0	9.87E+06	-15.2	44.3%
	16	900	30.0	1.08E+07	-13.2	46.9%
	17	950	30.0	2.02E+07	-12.5	51.6%

Sample	Step	Temperature (°C)	Time (min-utes)	^{21}Ne* atoms	ln(D)	Fcum
	18	1000	30.0	2.39E+07	-12.1	57.2%
	19	1050	30.0	2.92E+07	-11.7	64.0%
	20	1100	30.0	2.59E+07	-11.6	70.1%
	21	1000	60.0	1.14E+07	-12.9	72.7%
	22	900	60.0	2.74E+06	-14.3	73.4%
	23	800	180.0	1.67E+06	-15.8	73.8%
	24	1100	60.0	3.94E+07	-11.3	83.0%
	25	1150	60.0	3.81E+07	-10.8	91.9%

References

Balout, H., J. Roques, C. Gautheron, and L. Tassan-Got (2017). "Computational investigation of interstitial neon diffusion in pure hematite". In: *Computational Materials Science* 128, pp. 67–74.

Balout, H., J. Roques, C. Gautheron, L. Tassan-Got, and D. Mbongo-Djimbi (2017). "Helium diffusion in pure hematite (α-Fe_2O_3) for thermochronometric applications: A theoretical multi-scale study". In: *Computational and Theoretical Chemistry* 1099, pp. 21–28.

Cox, S. E., K. A. Farley, and D. J. Cherniak (2015). "Direct measurement of neon production rates by (α,n) reactions in minerals". In: *Geochimica et Cosmochimica Acta* 148, pp. 130–144.

Dahl, P. S. (1996). "The effects of composition on retentivity of argon and oxygen in hornblende and related amphiboles: A field-tested empirical model". In: *Geochimica et Cosmochimica Acta* 60.19, pp. 3687–3700.

Dodson, M. H. (1973). "Closure temperature in cooling geochronological and petrological systems". In: *Contributions to Mineralogy and Petrology* 40.3, pp. 259–274.

Farley, K. A. (2007). "He diffusion systematics in minerals: Evidence from synthetic monazite and zircon structure phosphates". In: *Geochimica et Cosmochimica Acta* 71, pp. 4015–4024.

Farley, K. A. and R. M. Flowers (2012). "(U–Th)/Ne and multidomain (U–Th)/He systematics of a hydrothermal hematite from eastern Grand Canyon". In: *Earth and Planetary Science Letters* 359-360, pp. 131–140.

Farley, K. A. and R. McKeon (2015). "Radiometric dating and temperature history of banded iron formation–associated hematite, Gogebic iron range, Michigan, USA". In: *Geology* 43, pp. 1083–1086.

Farley, K. (2000). "Helium diffusion from apatite: General behavior as illustrated by Durango fluorapatite". In: *Journal of Geophysical Research* 105.B2, pp. 2903–2914.

Fechtig, H. and S. Kalbitzer (1966). "The Diffusion of Argon in Potassium-Bearing Solids". In: *Potassium Argon Dating*. Ed. by O. A. Schaeffer and J. Zehringer. Berlin, Heidelberg: Springer Berlin Heidelberg, pp. 68–107.

Fortier, S. M. and B. J. Giletti (1989). "An empirical model for predicting diffusion coefficients in silicate minerals." In: *Science* 245.4925, pp. 1481–1484.

Gautheron, C., L. Tassan-Got, and K. Farley (2006). "(U–Th)/Ne chronometry". In: *Earth and Planetary Science Letters* 243, pp. 520–535.

Lovera, O. M., F. M. Richter, and T. M. Harrison (1991). "Diffusion Domains Determine by ^{39}Ar Released During Step Heating". In: *J Geophys Res* 96.B2, pp. 2057–2069.

Reiners, P. W. (2005). “Zircon (U-Th)/He Thermochronometry”. In: *Reviews in Mineralogy and Geochemistry* 58, pp. 151–179.

Shannon, R. D. (1976). “Revised effective ionic radii and systematic studies of interatomic distances in halides and chalcogenides”. In: *Acta Crystallographica Section A* 32.5, pp. 751–767.

Shuster, D. L., P. M. Vasconcelos, J. A. Heim, and K. A. Farley (2005). “Weathering geochronology by (U-Th)/He dating of goethite”. In: *Geochimica et Cosmochimica Acta* 69.3, pp. 659–673.

Solé, J. and T. Pi (2006). “Determination of the 22Nenucl/4Herad ratio in natural uranium-rich fluorite by mass”. In: *Physical Review C* 74.4.

Zhao, Z. F. and Y. F. Zheng (2007). “Diffusion compensation for argon, hydrogen, lead, and strontium in minerals: Empirical relationships to crystal chemistry”. In: *American Mineralogist* 92.2-3, pp. 289–308.

Chapter 3

Noble Gas Mass Spectrometry with a Quadrupole Ion Trap

3.1 Introduction

I have spent the latter half of my thesis working on the development of a new noble gas mass spectrometer using an old piece of technology: the quadrupole ion trap. This undertaking is unlocking a new generation of ultra-low-abundance measurements of a large array of noble gas species in diverse samples, but especially in extraterrestrial environments and in low abundance cosmogenic nuclide dating targets. The static vacuum quadrupole ion trap will expand our ability to measure noble gas species and open the door to new applications, much in the way that technological developments have driven progress in isotope geochemistry, and especially in noble gas geochemistry, since the inception of the field. While the magnetic sector mass spectrometer has strengths that the quadrupole ion trap is unlikely to match, such as absolute sensitivity on a single species, stability, and dynamic range, the quadrupole ion trap will find a place in mass spectrometry labs due to its own strengths of ultra low detector background, small volume, high mass resolution, and ability to scan over a wide mass range without loss of sensitivity.

3.1.1 History of noble gas mass spectrometry

The first separation of stable isotopes of an element involved a noble gas; J.J. Thomson separated ^{20}Ne ions from ^{22}Ne ions using a rudimentary mass spectrometer

in 1913 (Thomson, 1913). This development led to a flurry of research on splitting "positive rays," much of it done on noble gases by A.J. Dempster using magnetic sectors (Dempster, 1918). Modern noble gas mass spectrometry began with argon measurements performed on one of the earliest mass spectrometer designs by Al Nier (Nier, 1936). This early mass spectrometer was a double-focusing magnetic sector mass spectrometer with an electron ionization source (now called a Nier source) that uses rectangular symmetry. Noble gas mass spectrometers have largely followed the same design over the following 80 years, with arguably the most fundamental change coming with the development of the Reynolds static vacuum mass spectrometer in the 1950's (Reynolds, 1956). All developments since the 1930's have followed advances in technology that allow operators to achieve pre-existing goals. The switch to static vacuum, the use of stainless steel rather than glass, the move to turbomolecular pumps and ion pumps from diffusion pumps, and the use of ion counting detectors have all been incremental changes allowed by progress in ancillary technologies rather than fundamental redesigns of the Nier mass spectrometer.

Other designs used for noble gas mass spectrometry include the quadrupole mass spectrometer, which has been used primarily for the low-precision measurement of abundant helium in (U–Th)/He dating (e.g. Farley 2000), the accelerator mass spectrometer, which is being explored for niche applications such as replacing decay counting in the measurement of short-lived radioactive noble gas species, time of flight mass spectrometers intended for the low-precision measurement of extremely

small samples (Crowther et al., 2008), and the ion trap, which has seen limited use in the measurement of noble gases prior to this work (Ramisetty, 2015). Experimental designs such as the Baur compressor ion source have comprised slight modifications to one element of the Nier instrument (Baur, 1999). Other niche applications that allow the measurement of large quantities of noble gas and require high precision, such as the measurement of the isotope ratio of argon in air (Lee et al., 2006), have used continuous-inlet mass spectrometers with a pressure-balanced sample and standard inlet system of the type typically used for the measurement of major species such as carbon dioxide; the design of these mass spectrometers is essentially the same as the static vacuum mass spectrometers that descended from the Reynolds instrument with the exception of the vacuum hardware and sample inlet systems. Few applications of noble gas mass spectrometry have escaped the long shadow of Nier because, absent a compelling interest in reducing the cost, size, or sensitivity to environmental conditions of the instrument, it has not been possible to surpass the efficacy of this early design within the constraints of the development budgets available to this very small field.

The Nier mass spectrometer was an improvement on the Bainbridge mass spectrometer, which introduced the concept of separating ions sequentially according to mass/charge ratio using a magnetic sector and an electric sector (Bainbridge and Jordan, 1936). The Nier mass spectrometer comprised a glass vacuum chamber evacuated by a mercury diffusion pump, Nichrome lenses, and Kovar feedthroughs. Aside from the diffusion pump, which has largely fallen out of favor due to more

convenient alternatives, the vacuum hardware would be surprisingly recognizable to most modern operators. The Nier ion source produces electrons using a hot filament held at a potential of a few kiloV, focused by lenses that drop to an intermediate value (with the possibility of an offset perpendicular to the axis of the ions), then to ground. The ions accelerated thus are analyzed and refocused through a bent flight tube by a large electromagnet following the concept introduced by Barber (1933) and refined by Bainbridge and Jordan (1936). The Nier magnet was battery powered, but was otherwise strikingly similar to those on modern million-dollar instruments; the use of leveling screws and a rolling iron frame drives home this similarity. Detectors were strictly of the type known today as Faraday detectors, as electron multipliers were not yet available. However, the basic concept of a secondary electron multiplier was worked out during the First World War (e.g., Slepian 1923), and they were in regular use for particle counting by the 1930's (Allen, 1939), so this is not a particularly new technology, either.

The primary shift in the field of noble gas mass spectrometry since the Reynolds mass spectrometer has been the shift from homebrewed glass mass spectrometers built by scientists to commercial stainless steel mass spectrometers built by a handful of companies concentrated in rural England and Germany. Instruments such as the MAP 215-50 were designed for low cost and simplicity, while instruments such as the Thermo Helix MC were designed to push the limits of the technology, but the fundamental construction of the instruments—whether they were single- of multi-collector, and whether they were computer controlled or still used a chart

recorder—has not varied.

3.1.2 History and future of extraterrestrial mass spectrometry

Mass spectrometry has been instrumental to the space program since its inception. Many of the early Apollo missions were supported and motivated by ground-based mass spectrometry, which led to early breakthroughs such as the dating of lunar rocks (Papanastassiou et al., 1970). Samples brought back from the moon allowed scientists to unleash the capabilities of large, delicate laboratory instruments on lunar science, but the difficulty of returning samples from other extraterrestrial targets has meant that the mass spectrometers must often be taken to the measurement. Building a mass spectrometer that is small, efficient, and rugged enough to fly on a space mission often involves significant compromises in both the quality of sample preparation and in the instrument itself.

Some of the first space missions carried mass spectrometers. Early mass spectrometers were used for Earth atmospheric measurements on rockets and orbiters in the early days of the space program (Hoffman, Griffin, et al., 2010), and Apollo 15 carried the first mass spectrometer out of Earth's atmosphere. This instrument was a miniaturized magnetic sector mass spectrometer that was used to measure the lunar atmosphere (Hoffman, 1972). The final manned mission to the first American space station, the NASA Skylab, carried a gas chromatograph mass spectrometer to monitor volatile organic compounds for astronaut safety (Liebich et al., 1975). Later missions in the Space Shuttle program continued to carry instruments aimed at monitoring the air quality in the vehicle cabin (James et al., 1994), and the In-

ternational Space Station has recently carried a version of the JPL quadrupole ion trap (Darrach, Chutjian, et al., 2012). This is the first JPL quadrupole ion trap to participate in a space mission.

The first mass spectrometer to fly to another planet and measure geologic samples *in situ* was on the Viking 1 mission. A gas chromatograph on the Viking lander accompanied a biological experiment and was expected to provide a preliminary indication of the organic content of the Martian surface (Biemann et al., 1976). This measurement showed a surprising lack of organic compounds in Martian soils, a finding that was instrumental in directing the search for life on subsequent missions and in informing the interpretation of confusing results from the other instruments onboard. Overshadowed by the results of the soil experiment was another mass spectrometer on the same mission, a double-focusing magnetic sector mass spectrometer designed to measure the composition of the upper atmosphere (Nier and McElroy, 1977). This measurement was extremely important to the success of the gas chromatograph experiment because an early Russian measurement of the Martian atmosphere had suggested the presence of significant Ar (Istomin and Grechnev, 1976), which would have cripped the getter-pumped instrument on the lander (Ezell and Ezell, 1984).

Subsequent missions have carried more mass spectrometers to Mars. The Thermal Evolved Gas Analyzer on the Phoenix lander coupled another miniaturized magnetic sector mass spectrometer with a series of ovens meant to investigate the rocky ice in the Martian polar region (Hoffman, Chaney, et al., 2008). Most re-

cently, the Curiosity rover carried the Sample Analysis at Mars instrument suite, which includes a quadrupole mass spectrometer (Mahaffy et al., 2012). This set of instruments is designed to measure a wide range of species from atmospheric, rock, and soil samples. The SAM mass spectrometer is not capable of resolving isobaric interferences, but the scientists on the mission have been able to use the ratios of different chemical species to perform the corrections necessary to do geochronology nonetheless (Farley et al., 2014). Still, while these results have been impressive, a mass spectrometer with higher mass resolution and the ability to operate in static vacuum would have better sensitivity to both low abundance cosmogenic nuclides and to small isotopic perturbations.

3.1.3 History of the quadrupole ion trap

The quadrupole ion trap (QIT) is an old technology, but not one that is familiar to most geochemists. Geochemists have traditionally used magnetic sector mass spectrometers, favored for their stability, simplicity, and ability to resolve species of the same nominal mass such as the isotopes of uranium and lead or the isotopologues of carbon dioxide from one another and from interfering species at the same mass (isobars). Other instruments such as gas chromatographs (for organic geochemistry) and quadrupole mass spectrometers (for noble gas and trace element geochemistry) have become important as well. The QIT is a three-dimensional analog of the two-dimensional quadrupole lens used as a mass analyzer in a quadrupole mass spectrometer. Where the quadrupole lens adjusts the trajectory of ions passing through a plane such that only ions of a certain mass-to-charge (m/z) ratio are trans-

mitted to a detector or another lens element, the QIT presents a three-dimensional electric field that influences ions in three axes such that they are confined in space. For the first half of its existence, the QIT was used primarily in physics labs for experiments on ion storage and mass measurement. It was not until the 1980's that a series of breakthroughs allowed it to enter the commercial mass spectrometry market, and it has never become popular outside of the niche market for mass spectrometers capable of resolving very heavy organic molecules.

The first quadrupole ion traps were designed several decades after the first magnetic sector mass spectrometers, starting around 1950. The early development of the instruments was led by a group of physicists affiliated with Wolfgang Paul, who won the Nobel Prize in physics (along with Hans Dehmelt) for this work in 1989 and published a useful summary of the preceding four decades of work on ion traps in Paul (1990). Quadrupole ion traps, quadrupole mass filters, electronic lenses, Penning traps, and many other technologies emerged from early research into the use of electronic and magnetic lenses to manipulate particle motion, and it can be difficult to track the history of a single one of these due to frequent cross-pollination. However, the development of an RF-driven QIT for the purpose of measuring ion abundance ratios can be traced most clearly to Paul and Steinwedel (1953) and subsequent research at the University of Bonn. This group had produced a working instrument and filed a patent by 1956 (Paul and Steinwedel, 1956). These early instruments operated with a fixed RF potential on the main ring electrode, sometimes a DC offset, and a variable frequency RF applied along the axis of the

QIT to destabilize ions through resonant excitation.

As time-of-flight instruments, QIT mass spectrometers can achieve very high mass range in a relatively compact package, and without reducing the transmission of the ion beam (there is no "slit" on a time-of-flight instrument). This led to their introduction as commercial instruments in the early 1980's, primarily to measure large organic molecules (March, 2009). Virtually all of these instruments are based on the "mass selective instability" mode of operation, which was introduced by George Stafford of Finnigan MAT in the 1980's and which greatly simplified the operation of the QIT (Stafford et al., 1984). Prior to this, most QIT mass analysis had been conducted in the "resonance excitation" mode of operation, the technique described above that was introduced with the first QIT patent by Paul. The only exceptions before the Stafford development were a series of ion traps designed by Peter Dawson to operate in a narrow range of the stability field through the use of a DC potential applied to the ring electrode along with the RF drive potential (Dawson, 1969). The stability field could be tightened such that only a single species was trapped, after which it could be ejected and measured. The Stafford technique, in contrast to these other approaches, provided a simple way to rapidly scan a large mass range with high resolution and good stability.

An important aspect of the Stafford approach was the use of a buffer gas, usually He, to "cool" the trapped ions through neutral-ion collisions after a period of ionization. This buffer gas allowed the QIT to trap ions at a relatively high RF potential, providing good trapping efficiency, but then also to narrow the energy distribution

of the ions once trapped, providing the possibility of good mass resolution. The combination of these effects meant that the Stafford QIT could operate with both good sensitivity and high mass resolution, but since it required ~1 mbar of He, not at high vacuum.

3.1.4 Theory of operation of the quadrupole ion trap

An ion trap is simply a set of electrodes that create an electric field that traps charged particles. Three electrodes comprise the QIT: a central ring electrode, which defines the trapping volume in two identical axes, and two identical end cap electrodes, which define the trapping volume in the third axis. Each electrode presents a hyperbolic surface to the trapping volume, which is necessary to create field lines that stably trap ions. The space between the electrodes is defined by insulating spacers (alumina ceramic in an ultra high vacuum system), which allows gas to enter and leave the trap, and which allows a high voltage RF potential to be applied between the ring and the end caps. The field lines created by these electrodes define an oscillating potential well that confines the ions created or injected in the trapping volume. The frequency of oscillation of this potential well is the sine wave frequency of the RF potential applied to the electrodes. This frequency is chosen to coincide with the characteristic resonant frequency of the LC circuit defined by the ion trap (close to an ideal capacitor) and a metal air core coil (close to an ideal inductor) attached to the trap through a vacuum feedthrough. At the resonant frequency, this circuit acts as both an amplifier, generating higher potentials at the trap than would be possible with simply an RF power amplifier, and a filter, excluding

frequencies other than the resonant frequency that might cause ions to destabilize at different or unpredictable times.

The characteristic resonant frequency of an LC circuit is defined by these two ideal elements, and is proportional to the inverse square root of the inductance and the capacitance:

$\omega_0 = \sqrt{\frac{1}{LC}}$ (rad/s)

$f_0 = \sqrt{\frac{1}{2\pi LC}}$ (Hz)

The degree of amplification and the quality of the filtration is then defined by the RLC circuit that best approximates the actual system, in which significant resistance is presented by the wires, connectors, and feedthroughs used to connect the electronics to the QIT electrodes. No conductor is ideal, and the impedance (impedance is resistance correctly defined for an alternating current, which considers inductance and c capacitance, including the parasitic capacitance of all the metal around the conductors) presented by these elements is a function of frequency. The DC resistance of a well-configured ion trap system may be only a few Ω, but the impedance at several megahertz can be tens of Ω in the same system. As a result, the quality factor (Q-factor or just Q) of the circuit typically declines with frequency even though the formula for Q places frequency in the numerator:

$Q = \frac{1}{R}\sqrt{\frac{L}{C}} = \frac{\omega_0 L}{R}$ (unitless)

The value ω_0L is the inductive reactance of the circuit, which is the phenomenon in which the current flow and voltage on an inductor are out of phase (by 90° in

the ideal case, less in the real case of significant resistance; this value is sometimes written as $j\omega_0 L$, where j is the imaginary number, and +j corresponds to 90 degrees out of phase). As the circuit approaches resonance, one can see the current and voltage move out of phase when measured with a voltage probe and a current probe on an oscilloscope. Technically, one could search for resonance this way, but in practice it is not nearly as sensitive as the approaches that we use.

The capacitance of the QIT is defined by the spacing and geometry of the electrodes used for the ring and end caps, and is therefore not easily modified. The tuning of the RLC circuit is performed by selecting an appropriate inductor to achieve the desired resonant frequency and then by minimizing resistance to maximize Q. The resonant frequency is chosen by accounting for the required mass resolution of the QIT, as the resolving power increases with frequency. Increasing the frequency of the circuit typically increases its impedance, reducing Q, and also increases the power requirements of the circuit and increases the RF interference with every other aspect of the electronics, so there is a trade-off between resolution and most other aspects of QIT performance.

One can derive the stability conditions for a trapped ion in a QIT from the equations of motion. As summarized in (Paul, 1990), the quadrupole potential field Φ is given by the quadratic equation:

$$\Phi = \frac{\Phi_0}{2r_0^2}(\alpha x^2 + \beta y^2 + \gamma z^2) + C$$

Where Φ_0 is the ring potential, r_0 is the trap radius, and the z direction corresponds to the axis of the trap (the line that passes through the center of the ring and

each end cap). The parameters α, β,and γ must be chosen to satisfy the stability condition given by Laplace's equation $\Delta\Phi = 0$. Taking the partial second derivatives of $\Phi = 0$ gives $\frac{\partial^2\Phi}{\partial x^2} = 0$, and likewise for y and z. Substituting back into the Laplace condition gives $\Delta\Phi = 0 = \alpha + \beta + \gamma$. In three dimensions, asserting that x = y, this gives $\alpha = 1$, $\beta = 1$, and $\gamma = -2$, meaning that the field is twice as strong in the z direction. This has obvious consequences, such as that the frequency of secular motion of ions trapped in the potential well will be different in the z direction and the off-axial direction. Since the x and y axes are equivalent, we can simply refer to the off-axial direction as r, which simplifies the coordinate system and allows us to concern ourselves only with stability in two axes.

The potential field described by this equation has hyperbolic field lines, and is therefore generated by hyperbolic electrodes. The r electrodes are most conveniently combined into a ring, equivalent to bending two of the rods of a two-dimensional quadrupole lens and joining them at the ends to form a circle. The z electrodes are then separate pieces, equivalent to deforming the other two rods of the two-dimensional lens such that they present hyperbolic surfaces in all orientations of the r axis (that is, the electrodes must be circular with respect to the r axis). This configuration is illustrated as a cross section below (figure modified from Madzunkov and Nikolić 2014):

The hashed grey line is the z-axis. The central ring electrode is shown in dark blue, the end caps in light blue, and the ceramic insulators in fuchsia. The gap in the ceramic electrodes that allows gas to enter (either through dedicated tubing through

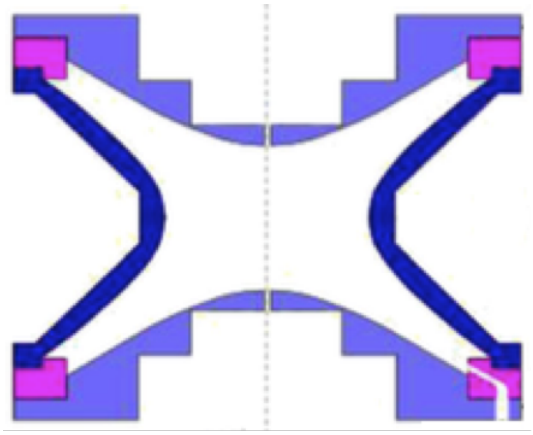

the end cap or simply from the ambient vacuum chamber) is shown schematically as a break in the lower right corner. The electrodes and the insulators are symmetric about the z-axis in three dimensions.

A two-dimensional quadrupole confines an ion beam in two dimensions, allowing it to serve as a mass analyzer or a focusing element. When an RF potential is applied to the three-dimensional electrodes described above, it creates an oscillating potential well of a few V or tens of V that confines ions (Paul, 1990). Because the depth of this potential well scales with the voltage at which a given ion is trapped, and because the trapping voltage scales with mass, the QIT tolerates a larger energy spread of ions at both higher frequency and higher mass. This phenomenon occurs in addition to the fact that mass resolution scales with mass because resolution is constant in voltage at a given operating frequency, and the voltage of maximum stability for an ion increases linearly with mass.

All of the JPL QIT mass spectrometers operate in mass selective instability mode as introduced by Stafford et al. (1984), although usually not with a buffer gas. Instead, we trap and then cool the ions solely through manipulation of the RF drive

potential. Some versions of the JPL QIT use a secondary RF applied at the endcaps to create a dipole field for resonant ejection, but this is used only to enhance the effect of the mass selective instability provoked by the primary RF drive potential, not to replace it.

The geometry of the QIT means that the only axis of concern for mass analysis is the z axis, and the radial axis is only used for confinement. Since we have asserted that x = y, we can convert the potential defined above, using $\alpha = \beta = 1$ and $\gamma = -2$, to cylindrical polar coordinates using the transformation $x = r\cos\theta$, $y = r\sin\theta$, and z = z. This gives us

$$\Phi = \frac{\Phi_0}{2r_0^2}(r^2 - 2z^2)$$

If we apply an oscillating potential field with no DC offset to the ring electrode, the potential on the electrode is given by $\Phi_0 = V_{\text{pk}}\cos[\omega t]$. We can plug this into the equation above to find

$$\Phi = \frac{V_{\text{pk}}\cos[\omega t]}{2r_0^2}(r^2 - 2z^2)$$

If we fix r and consider motion in the z direction, we find

$$\Phi_r = \frac{V_{\text{pk}}\cos[\omega t]}{2r_0^2}(-2z^2)$$

The electric field in the z axis is then given by the spatial derivative

$$\frac{d\Phi_{r=0}}{dz} = -4z\frac{V_{\text{pk}}\cos[\omega t]}{2r_0^2}$$

The force on a charged particle is then

$$F_z = -e\frac{d\Phi_{r=0}}{dz} = 4ez\frac{V_{\text{pk}}\cos[\omega t]}{2r_0^2}$$

And since $F = ma$,

$$4ez\frac{V_{\text{pk}}\cos[\omega t]}{2r_0^2} = m\frac{d^2z}{dt^2}$$

or,

$$\frac{d^2z}{dt^2} = \left(\frac{4eV\cos[\omega t]}{m(2r_0^2)}\right)z$$

We recognize this is a form of the Mathieu equation,

$$\frac{d^2y}{dx^2} + (a - 2q\cos[2x])y = 0$$

From which we derive the stability constants,

$a = 0$ (because we have fixed the DC potential at zero)

$$q = \frac{4eV}{mr_0^2\omega^2}$$

The Mathieu equation has two sets of stable solutions, and only the stable solutions are of interest to the operation of the QIT. The unstable solutions represent those in which the particle motion blows up in one or both axes. The stability region of typical interest is shown in Figure 3.1 for $^{40}Ar^+$ ions in a 1.404 MHz trap at an RF voltage of 200 V_{pk}.

We have included the full figure for reference, but again, in the case that we do not apply a DC potential to the ring electrode, only the x-axis is of interest. The stability region ends at $q_z = .908$, so we can solve for q_z values below 0.908 to determine stability for a given RF configuration.

Also note that the figure includes a calculation of the frequencies of secular motion of the ions, which is not covered here. This can be calculated from the

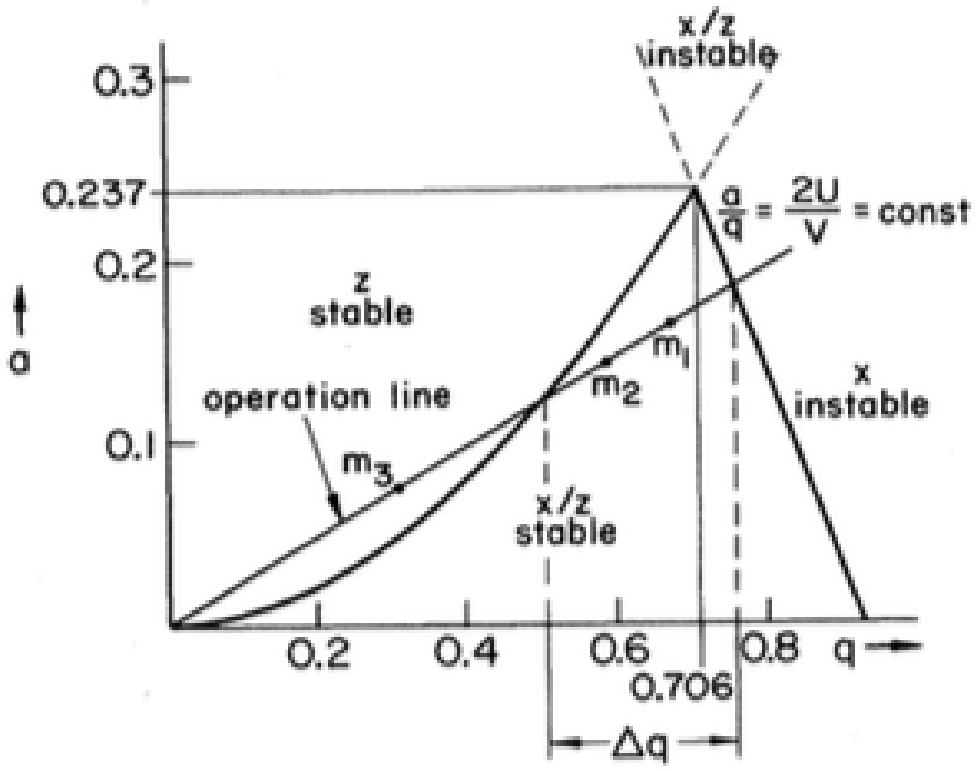

Figure 3.1: The Mathieu stability diagram for f = 1.404 MHz, V_{pk} = 200 V, m = 40 amu, and z = +1. Produced using the application at <http://iap.iisc.ac.in/ amohanty/paulTrapStability.html>, 4 December 2016

same equations of motion used above, and is especially of interest when resonance ejection is used. In this mode of operation, the RF field applied at the end caps can be set to the frequency of secular motion for an ion trapped in the main quadrupole RF field to perturb the ion from its stable path. This can be used both to analyze ions and to remove certain ions from the ion cloud in order to make the trapping and analysis of other ions more convenient. The motion of particles in the ion trap is complicated, but generally follows a bent figure-eight path with less important higher-order motions superimposed on it, as shown below in a photomicrograph reproduced from Paul (1990).

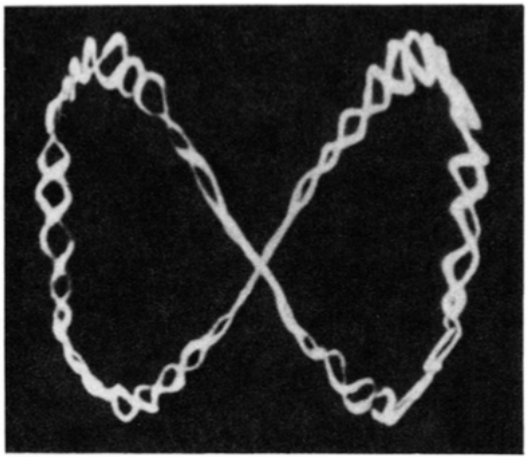

3.2 Hardware, calibration, and measurement schemes

3.2.1 Mass spectrometer hardware

3.2.1.1 Ion trap electrodes

The ion trap comprises a central ring electrode with an end cap electrode on either side of the ring (Figure 3.2). The electrodes in the JPL QIT are machined from a titanium alloy chosen for exceptionally low outgassing and for durability and machinability. The inner surface of the ring and the end caps are hyperbolic. An RF potential is applied to the ring, creating the quadrupole electric field that lends the QIT its name and its mode of mass analysis.

The end caps are isolated from the ring, typically using a spacer made from alumina, PEEK, or another insulator, and the separation produces the capacitance of the ion trap (typically 55-80 pF in the JPL QIT). This isolation means that when a potential is applied to the ring electrode, current will flow to the end caps by means of an induced displacement current. This coupling is commonly referred to as “AC coupling,” as opposed to “DC coupling,” in which a direct connection

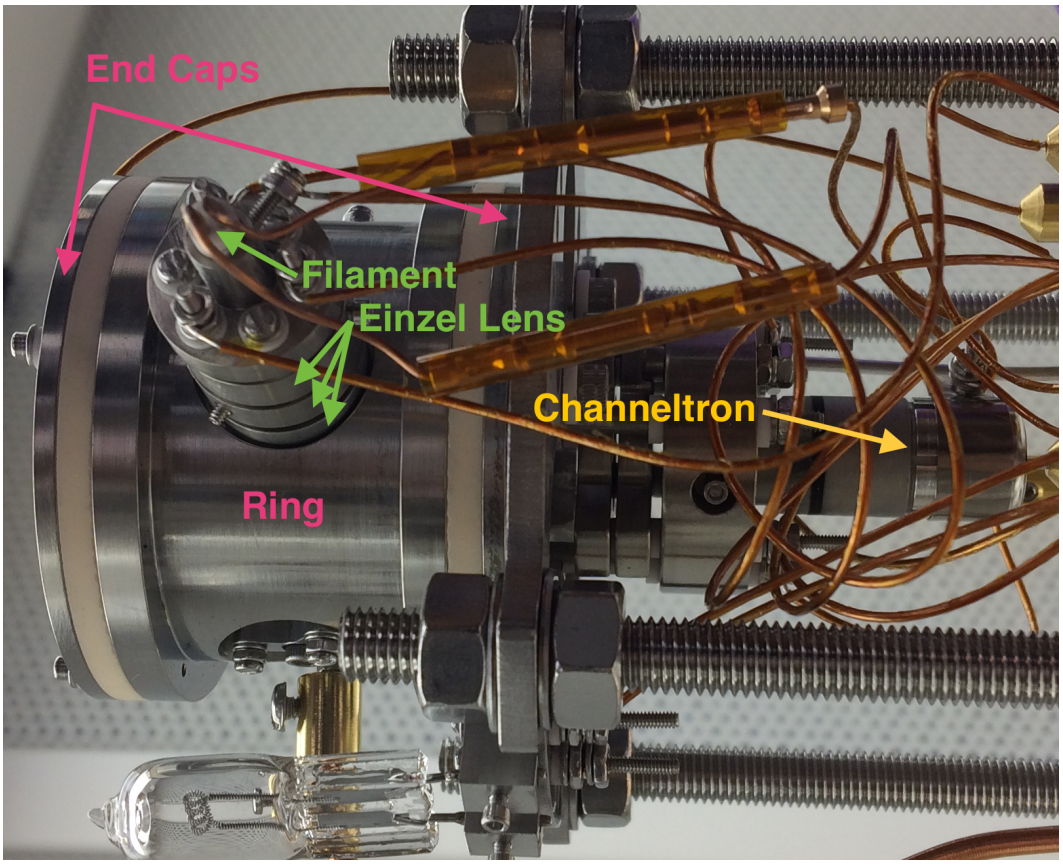

Figure 3.2: Photo of the JPL quadrupole ion trap. The ion trap electrodes are labeled in red. The main RF potential is applied at the ring electrode, and the end caps, usually grounded, present a capacitance of approximately 65 pF to the ring. The electric field produced by the hyperbolic interiors of these electrodes defines the trapping region. The filament is labeled in green, and is mounted in its lens assembly. The Channeltron detector, mounted behind the protective grid lenses, is labeled in orange.

between conductors provides the opportunity for direct current flow. A better term is the alternative "capacitive coupling," as opposed to "conductive coupling."

The ion trap electrodes provide the lion's share of the capacitance in the RLC circuit formed by the trap, a coil inductor, and the connections between them. These elements are connected in series, forming a series RLC resonator with a characteristic resonant frequency given by $\omega_0 = \sqrt{LC}$. The impedance in these circuits is minimized to the extent possible, and is not more than a few Ω at 1

MHz. It may be significantly higher at higher frequency. The capacitance of the JPL QIT is nominally 65 pF, and varies from 55 to 80 pF in different configurations, depending on the choice of insulator and the configuration of wires, lenses, and vacuum chamber components around the trap. The inductance of the coil is chosen for a particular application to give the correct resonance frequency, typically between 500 kHz and 5 MHz for the JPL QIT.

A major consideration in achieving high mass resolution with an ion trap is the precision machining of the hyperbolic surfaces of the trap electrodes. The effect of machining errors within a given tolerance can be estimated by the following equation provided by Orient and Chutjian (2002).

$$m/\Delta m = (|\Delta V/V| + 2|\Delta\omega/\omega| + 2|\Delta r_0/r_0|)^{-1}$$

According to this equation, the machining tolerance of the electro-polished titanium surfaces of the JPL QIT electrodes, which is 0.2 thousandths of an inch (5 μm), limits the resolution of the ion trap to about 10,000. This represents a significant improvement over the previous generation of the JPL QIT, in which the resolution was limited to about 300 by the machining (Orient and Chutjian, 2002). It is also worth noting that the machining quality of the electrodes has not been independently verified by, for example, laser mapping of the electrode surfaces.

Machining the trap from titanium is of limited use in a "vented" trap, the type used for noble gas measurements. In the typical configuration of the JPL QIT, gas is funneled directly into the center of the trap, where a relatively high pressure is maintained compared to the rest of the vacuum chamber. In the vented configuration,

the inside of the trap is in pressure equilibrium with the vacuum chamber, which is full of stainless steel components and which normally has stainless steel walls. For these traps, machining to the same tolerances from stainless steel would save money without affecting the performance of the QIT.

3.2.1.2 Ion source

The ion source is a simple electron ionization (also known as electron impact) source employing an Einzel lens to focus electrons into the center of the ring electrode (Figure 3.2). Ions created as close to the center of the ring as possible will experience the most ideal trapping, while ions created too far from the center will be ejected even at the trapping voltage, so it is important to focus electrons into this region. After the Einzel lens, a small aperture (1 mm diameter) restricts the transmission of electrons into the ionization region. Expanding this aperture might be desirable in vented traps; the current design considers the need to maintain the pressure gradient between trap and chamber.

Electrons are created using a Ta disc cathode intended for electron microscopy (typically the ES-042 from Kimball Physics). These cathodes are preferable to the wire filaments typically used in magnetic sector mass spectrometry because the emission is directional; the cathode comprises a circular emitter that produces electrons on its flat surface. These relatively large refractory metal cathodes are also significantly less fragile than wire cathodes, and in the larger sizes are capable of very high emission currents. The cathodes are available from the manufacturer on two bases; the standard AEI base is used in the axial ionization version of the QIT,

while the Kimball Physics CB-104 base is used in the side ionization version. These bases are made of high-purity alumina, and our mounting brackets are machined so that they fit tightly, providing automatic alignment.

The Einzel lens and the mounting bracket for the filament are machined from stainless steel at JPL. From the filament to the ion trap electrodes, there are four lenses that comprise the ion source. The mounting bracket (the cathode electrode) is held at the negative potential at which the electrons will be produced. The next electrode, the anode electrode, is the first lens of the Einzel and is held at ground during ionization. During mass analysis, the anode is held at negative voltage as well to prevent electrons from entering the Einzel. The third lens is the focusing lens, the middle lens of the Einzel, and is typically held at a negative potential approximately the same magnitude as the energy of the electrons. This provides focusing on a plane in the center of the ion trap. However, this lens may also be held at a higher ($\sim$ 2–3 times) positive potential to focus the electrons at a distance and provide an approximately collimated electron beam. The latter approach is easier to tune because it is less sensitive to small voltage changes, and produces a higher rate of electron transmission into the ionization region. However, it requires power supplies capable of producing 250-400 V. The final lens is the exit lens of the Einzel and is always grounded.

In the axial ionization version of the QIT, the lens assembly is mounted on screws that attach to the "bottom" end cap. Insulators that isolate them from the ion source lenses surround these screws. A separate set of screws holds the assembly itself

together and also provides connections to the each of the lenses. In the wireless version of the QIT, these screws then mount directly onto feedthrough pins using connectors that screw onto the screws and push onto the pins of the feedthrough flange. In the wired versions of the QIT, wires are simply attached to the ends of these screws using additional nuts.

In the side ionization version of the QIT, the lens assembly is mounted instead to the side of the ring electrode using screws surrounded by insulators. A separate set of screws holds the assembly itself together, as with the axial version. These screws are always connected to a feedthrough flange using wires that attach using additional nuts on the ends of the second set of screws, but it would be possible in principle to design a wireless version.

3.2.1.3 Ion detection

The QIT requires a detector capable of very fast measurements due to the analytical mode of the instrument. It must measure ions that emerge from the trap electrodes during a ramp of the amplitude of the RF field on the ring electrode. Complete ramps typically take anywhere from a few milliseconds to 100 milliseconds, and peaks may be as narrow as 10 microseconds or less. This means that taking advantage of the resolution of the analyzer requires a detector that can respond to ions and return to baseline within a few tens of nanoseconds. For this reason, analog detectors are not feasible; using them would be possible only in limited analytical modes, such as slowly scanning over very large peaks.

Every iteration of the JPL QIT has used a pulse-counting electron multiplier to measure ions. Some early versions used other versions of Channeltron and Spiraltron detectors, but the current instruments use either Photonis (previously Burle) 5901 MAGNUM Channeltrons or microchannel plate detectors (Figure 3.2). Because the spatial resolution of the latter is not of practical interest (the trajectory of the ion beam after ejection from the trapping region cannot be tuned in the current design), its primary advantage is the smaller size. The Channeltrons have better sensitivity, dynamic range, and hardiness, and are therefore preferred in most versions of the QIT.

3.2.1.4 Inductors

As described above, the R (resistor) and C (capacitor) in the RLC circuit are relatively invariant. The resistor is represented by all of the components in the circuit, and while we can try to minimize it further, the returns are small. The capacitor is defined by the geometry of the ion trap. The inductor (L), however, is an easily changed parameter that we select in order to set the resonant frequency of the circuit to the desired value.

The efficiency of the circuit, and therefore the voltage we are able to produce, is governed by the Q of the inductor. This quantity is described in detail above. We have used air core coils made from Litz wire and PTFE or PVC forms for most of the inductors at JPL, but Litz wire becomes undesirable at frequencies above about 2.5 MHz because the parasitic capacitance of the bundled wires becomes intolerable. Instead, we have found that the best inductors are air core coils made from large,

low resistance conductors such as copper tape. In addition, we have found that the stability of the circuit benefits from enclosing the inductor in metal. The inductors that we have made for high frequency experiments are therefore made from copper tape wound around PVC forms and enclosed in steel paint cans (purchased at a hardware store) with the necessary connectors installed in the lids.

We have also purchased several commercial high Q inductors for both low and high frequency work, and have seen good results from these as well. There are unfortunately few applications in modern electronics that require RF inductors in the frequency range that we use—most are designed for operation at significantly higher frequency. The inductors that we have purchased are used or new old stock inductors intended for loading antennas in old radio transmitters. TWo examples are shown below.

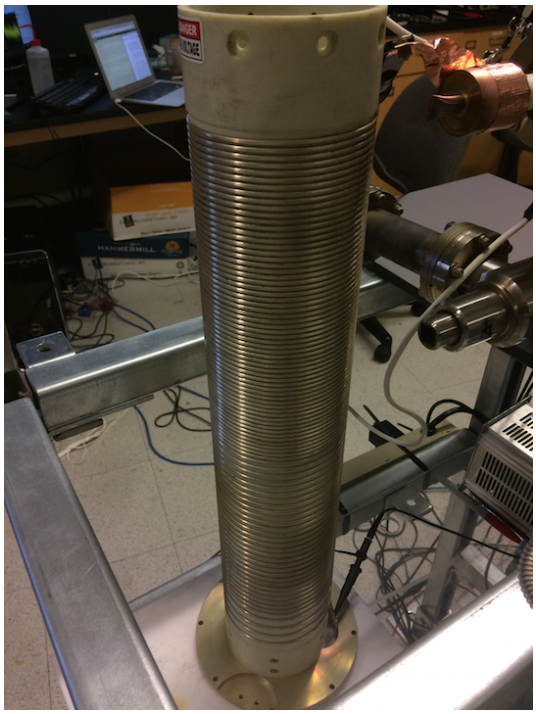

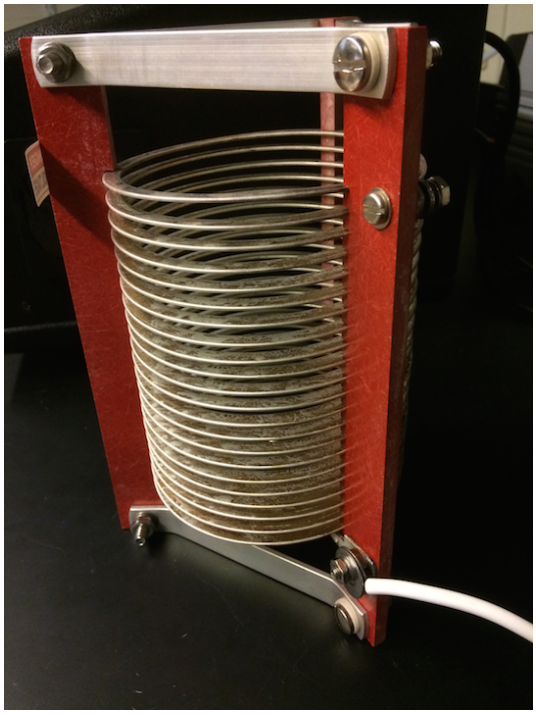

3.2.1.5 RF electronics

Creating a clean input signal for the drive RF on the ring and the supplemental RF on the endcaps (if used) is crucial to producing a clean mass spectrum. Power in frequency bands other than the desired one will perturb the ion oscillations, causing peaks to shift and broaden. Variation in the amplitude of the sine wave will cause the trapping efficiency of the trap to change between cycles and will cause peaks to shift in timing (and, therefore, in apparent mass) between cycles. The cleanest sine waves are produced using analog circuits that use an oscillator to create a true periodic signal, but these are impractical for this application because they are not easy to tune to different frequencies. The resonant frequency of the ion trap is affected by all of the components of the circuit and frequently changes due to intentional changes in the inductor and due to unintentional changes in any of these components, so the

ability to tune the sine wave frequency is crucial.

The next best option is to use a high-speed, high-resolution digital-to-analog converter (DAC) with an analog filter to synthesize the waveform. This can be done with a dedicated signal generator that produces the sine wave and another DAC that produces the ramp, which can be used to modulate the amplitude (I modulation) of the signal generator. We have used this approach to test whether the quality of sine waves produced digitally is adequate compared to a filtered bench-top signal generator, for example. A simpler approach is to synthesize the entire waveform, including the sine wave, with a sufficiently fast, high-resolution arbitrary waveform generator.

We use two different waveform generators in different configurations of the Caltech ion trap. One is on board the Red Pitaya, a single-board computer developed as a low-cost, portable laboratory instrument. The Red Pitaya FPGA has a 125 MHz clock that sets the maximum sampling speed of the sine wave synthesis to 125 MS/s (million samples per second). It synthesizes each point on the waveform with 14 bits of resolution from 0 to 2 V peak-to-peak. The quality of the waveform is noticeably diminished at low amplitude due to the limitation of the 14-bit DAC. We have found that it is advantageous to use an attenuator between the Red Pitaya and the power amplifier to maintain the desired input amplitude at the power amplifier while allowing the Red Pitaya to use the full range of its DAC for a given ramp.

The National Instruments PXIe-5451 is capable of 400 million samples per second, so it is plenty fast to synthesize a high-quality sine wave in the MHz range.

It also has 16 bits of output resolution and an analog gain that preserves the full range of this resolution into the mV range. This is especially important because the low amplitude trapping voltage is crucial to the efficient operation of the trap, especially when we measure light ions at low frequency. Finally, the PXIe-5451 has an analog filter capable of further smoothing the output sine wave.

We create files that describe every point on the waveform at 400 MS/s and then filter the output of the PXIe-5451 with its own filter and, after amplification, with the coil that serves as the inductor in the ion trap circuit. The observed input and output sine wave is extremely clean, with no remnants of the DAC synthesis, as seen in the oscilloscope measurement in Figure 3.3.

The quality of each signal generator is best measured with a spectrum analyzer. We have two spectrum analyzers available—a dedicated Agilent E4440A PSA Series Spectrum Analyzer at JPL and the built-in spectrum analyzer in the Tektronix MDO3034 oscilloscope at Caltech. The former is an instrument designed exclusively for spectral analysis, while the latter is an oscilloscope with a spectrum analysis function, so the former is capable of much more precise measurements of spectral purity. We have measured the output of the Red Pitaya and an Agilent 33250A signal generator, with and without the E&I 2200L power amplifier, on the Agilent E4440A spectrum analyzer, and we have measured the output of the Red Pitaya and the PXIe-5451 without a power amplifier on the Tektronix MDO3034. The Red Pitaya measurements allow the two techniques to be compared; the measurements of the PXIe-5451 spectral purity on the MDO3034 are clearly limited by the capabilities

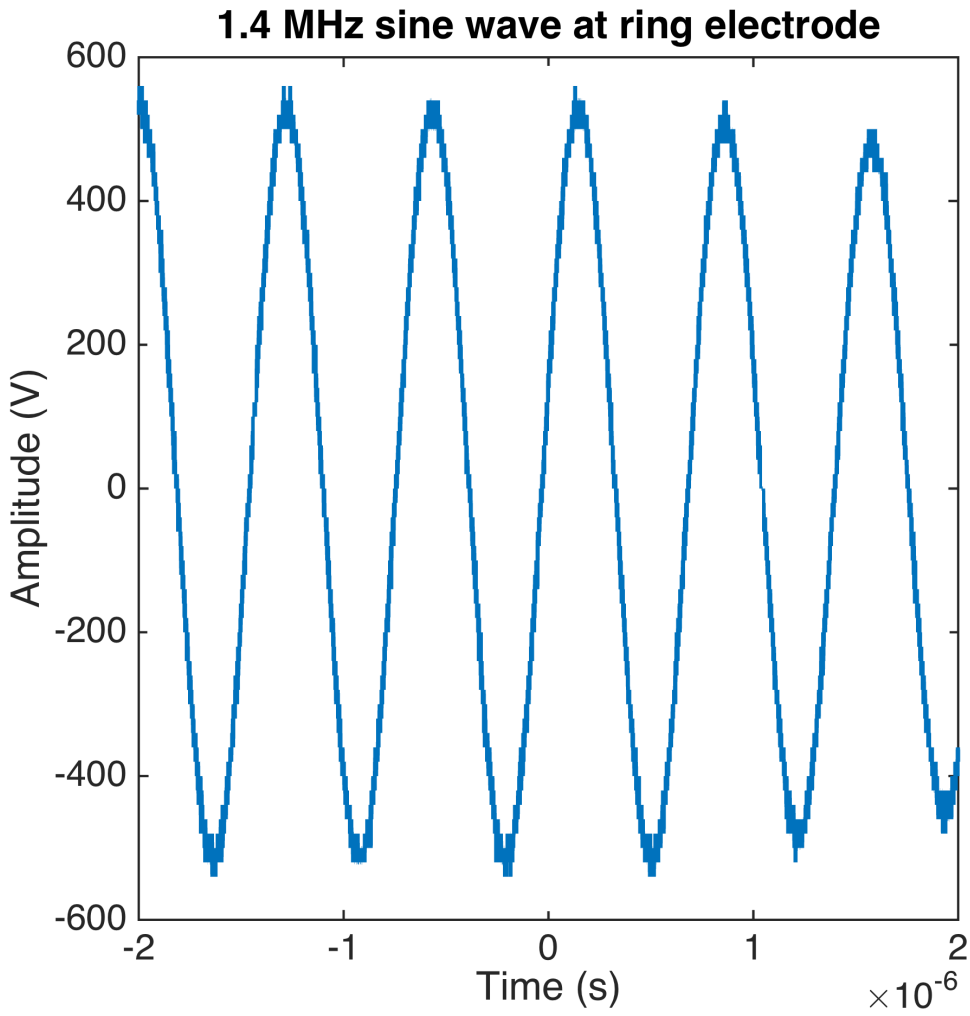

Figure 3.3: Oscilloscope trace showing a 1.404 MHz sine wave produced by at the vacuum feedthrough for the QIT ring electrode. The sine wave was synthesized digitally at a rate of 399.570 MS/s, then filtered by the PXIe-5451 analog stage, the E&I 2200L power amplifier, and the inductor coil.

of the oscilloscope, but all other measurements show artifacts above the background of the spectrum analyzer. These data demand further analysis, but for now are summarized in the Appendix.

3.2.1.6 Lens, timing, and ion counting electronics

The ion trap serves as its own ion source, so there are few lenses required for its operation. Ions are made in the middle of the trap by electrons created on a filament just outside. A simple Einzel lens, comprising three elements, focuses the electrons into the center of the trap. The Einzel has two grounded lenses, but one of them is pulsed (the "anode" lens) to negative voltage during analysis to prevent new ions from being created. The other, the "exit" lens, is always grounded. The middle lens, known as the "focus" lens, is held at a constant negative or positive voltage. This lens, along with the bias voltage applied to the filament and its holder (the "cathode"), is generated by a simple DC power supply—we use one capable of producing ±400 V to allow the full range of tuning possibilities on the focus lens. The power supply does not need to source appreciable current, so any power supply capable of these voltages is adequate.

3.2.1.7 Vacuum hardware and sample handling

The Caltech QIT is housed in a Kimball Physics spherical cube (part number MCF450-SphCube-E6C8A12) that fortuitously has almost the right amount of space in the linear face-to-face dimension for the complete axial ionization QIT. Because the Caltech trap uses side ionization, it does not require a chamber this large. Eventually, we plan to move it to a smaller chamber, or one with metal or alumina pieces inside, to reduce the overall volume. The choice of chamber is dictated primarily by the dimensions of the trap and the necessity of connecting lens elements

and gas inlets to different feedthroughs. A spherical cube is a good choice for a development system because of the large number of ports it affords, but a cylinder is a better choice for a production system because it is more congruent with the shape of the QIT.

The sample inlet system currently in use is very simple. It comprises only several Swagelok SS-4BG valves with the UHV stem tip and corresponding Swagelok tubing with VCR fittings. The requirements for sample handling and inlet are no different from those of any UHV noble gas mass spectrometer. We have observed on other versions of the QIT that opening and closing large valves changes the capacitance of the trap so much that it is necessary to retune the resonant circuit to operate at static vacuum, but this is not true on the Caltech system. The reason for the difference is not clear.

3.2.2 Control software

The software that controls the QIT is more complicated than the software that controls a sector mass spectrometer because of the demands of the time-of-flight measurement. Software must have the precision and speed to synthesize a high quality RF ramp and to repeatedly measure simultaneous ion counts.

3.2.2.1 Overview of JPL software

There are two sets of software programs on different QIT systems at JPL. The first is written in C++ (Madzunkov and Nikolić, 2014) and the second is written in Python. Both perform the same functions, but the C++ version interfaces with Na-

tional Instruments hardware on JPL development systems while the Python version interfaces with the Red Pitaya and JPL flight hardware. The C++ software has been ported to the Red Pitaya and some flight hardware, too, and the choice of software is largely a matter of preference.

3.2.2.2 Caltech Labview software

The Caltech QIT is operated by a set of integrated National Instruments electronics chosen for precise timing and high resolution. The parts of the system are outlined in the table below. These units all use hardware drivers from National Instruments that interface seamlessly with Labview, which we already use in the Caltech lab for hardware control. The software to control these units, which is provided in the appendix, is written in Labview for this reason. However, all of the National Instruments drivers that control the hardware in this PXI chassis can interface with other programming languages as well.

PXIe-1078 chassis	Rackmount chassis with nine slots (including the controller slot) for PXI/PXIe boards, 10 MHz and 100 MHz reference clocks, and eight trigger lines
PXIe-8840 controller	Onboard controller for PXIe system, runs Labview RT operating system
PXIe-5451 arbitrary waveform generator	16-bit, 400 MS/s dual channel arbitrary waveform generator for creating an arbitrary ramped sine wave for the main RF drive and the supplementary endcap RF drive
PXIe-6363 DAQ	High speed DAQ with four counters, 4 AO, 32 AI, and 48 DIO
PXIe-4137 SMU	Three PXIe-4137 boards for creating pulsed voltages up to 200 V
PXI-6514 DIO	Industrial 24 V DIO board for direct control of Festo valve relays

Timing and Synchronization A trigger produced by the PXIe-6363 DAQ board, which includes four high-speed counters, governs the timing of the Caltech system. The counter uses the 10 MHz reference clock in the PXIe-1078 chassis with PXIe-8840 built-in controller. We typically use a 20 Hz trigger to start a 50 ms sequence that includes ionization, cooling, and analysis, but this timing varies from a few ms to hundreds of ms depending on the application. The trigger starts an arbitrary waveform sequence that we create for the PXIe-5451 and also triggers pulse sequences from the three PXIe-4137 boards. Crucially, it also restarts a measurement sequence on one of the other counters on the PXIe-6363 board itself. The fact that all of these processes are linked to the same start trigger, retriggered every cycle, and referenced to the same onboard clock on the PXI chassis means that we are immune to problems with trigger jitter, clock synchronization, and sequence timing drift.

RF signal generation The PXIe-5451 is controlled by requesting pre-defined waveforms (such as a simple sine wave) or by loading binary files that specify each point in the waveform. These requests are interpreted by the National Instruments FGEN drivers, which interface with Labview or with various programming languages. It can also stream files from the controller if it is necessary to load waveforms that require too much memory to be loaded onto the card. We define waveforms using the Labview control software, then send them to the PXIe-5451 with a script that instructs it to loop the sequence on receipt of a trigger until another trigger is received, after which it will restart immediately. This approach allows us

to produce a continuous waveform without the requirement that we account for the jitter of the trigger signal.

The PXIe-5451 can also be modulated externally. In this case, we can simply request a sine wave of a given frequency using a built-in FGEN function, and then feed a modulation signal into the PXIe-5451. This is currently useful mostly for testing the effects of lower resolution rA, such as those produced by the Red Pitaya, on the trap. However, it would be possible to use a ramp with even higher resolution than the 16 bits provided by the PXIe-5451 this way.

Lens pulsing The pulsed lenses (the anode, grid 1, and grid 2) are controlled directly by three PXIe-4137 source measure units (SMUs). These units are capable of directly producing high-speed pulses up to 200 V, so no external power is required. They can also float up to 250 V, if higher pulses are necessary. The SMUs are controlled using the National Instruments DCPOWER drivers, which we also control from Labview. We define a pulse sequence consisting of a single pulse and a bias voltage, which is then retriggerable using the same trigger as the RF signal. It is possible to use an additional DAQ counter or a sequence with multiple pulses to create delays from the main trigger, but we find that this approach adds time to the measurement sequence while providing no benefit.

Ion counting The most challenging software requirement is counting the ions produced during ionization and analyzed during the RF ramp. The ramp and the ion counting must be precisely synchronized, and the ion counting must also be

gated sufficiently quickly to realize the full resolution provided by the RF ramp. This means that we must measure counts over precise time periods as short as one microsecond while maintaining consistent time offsets from the main trigger for each bin.

This challenge is met by using two of the counters on the PXIe-6363 board, which is controlled by the National Instruments DAQmx drivers. We use Labview to instruct the driver to use one counter to produce a 1 MHz pulse train, which we then use to gate the other counter. This entire sequence is restarted by the main trigger. Counter measurements do not include time information, so the 1 MHz pulse train creates the clock for the counting process. Because there is no timestamp, we cannot simply retrigger continuous counting using the main ramp. However, because the ramp always ends before the last few ms of the sequence, we can simply count for a fixed number of 1 MHz pulses that ends before the end of the sequence. For example, with a 50 ms sequence consisting of 2 ms of ionization, 8 ms of cooling, and 35 ms of RF ramp, we can count for 49,000 1-microsecond bins after the main trigger, which covers the ionization pulse and the entire ramp, and then restart this sequence every time the main trigger is detected.

3.2.3 The RF circuit

RLC circuits like the QIT store energy by charging a capacitor (C in RLC; in this case represented by the ion trap electrodes) and in an induced magnetic field in the inductor (L in RLC; in this case, the coil attached between the power amplifier and the ion trap electrodes). The resistor (R in RLC; in this case, the combination of

wires, connectors, and feedthroughs used to create the circuit) presents impedance that damps the oscillation of energy between these reservoirs like the damping of an oscillating weight on a spring. Just like the weight on a spring, this damping reaches a minimum at a characteristic frequency, in this case where the impedance is at a minimum. This is the resonant frequency of the RLC circuit, where power is transmitted most efficiently. Operating the QIT at the resonant frequency confers two important advantages: 1) because power is transferred most efficiently here, higher voltages can be achieved using the coil as an amplifier at the resonant frequency; and 2) because every other frequency band is transferred less efficiently, the coil acts as a filter that excludes stray power in other frequencies.

3.2.3.1 Finding resonance

At resonance, the circuit draws the most power at the highest voltage. Because the goal of increasing power transmission to the ion trap is to raise the voltage and thereby reach higher masses, the most obvious way to find resonance is to measure the voltage at the feedthrough for the ring electrode, after the RF signal has been amplified by both the power amplifier and the coil and also filtered by the coil. Sweeping frequency with a constant input amplitude will result in a broad peak in voltage at the feedthrough, with the peak voltage occurring at the resonant frequency. We frequently use a high bandwidth high voltage probe during development to keep track of resonant frequency and the quality factor (Q) of the circuit doing exactly this. The problem with this method is that even a high quality voltage probe of this sort presents more than 1 pF of capacitance, and it therefore degrades Q and

changes the resonant frequency slightly. During normal operation, therefore, we avoid attaching any probes at this point on the circuit.

Another good way to measure resonance is to measure power draw from the RF power amplifier. At resonance, more power is drawn by the circuit. The easiest way to measure this is with a 1:1000 current sense transformer connected in-line between the power amplifier and the coil. This transformer has a negligible impact on the circuit, but provides a secondary current of 1/1000 of the primary current that we can measure to determine the power being transmitted. This is usually on the order of a few A, which means that the secondary current will be a few mA. If terminated with a 50 Ω resistor, this provides a voltage of tens to hundreds of mV that we can easily measure with any analog input. The advantage of this approach, in addition to its minimal interference with the resonant circuit, is that we can also use it to continuously adjust the amplitude of the RF ramp to account for fluctuations in the quality of the circuit due to environmental factors, pressure changes in the vacuum chamber, and other variables that are difficult to control.

The least precise but also least invasive and simplest way to measure resonance is simply to place an oscilloscope probe near the chamber to measure RF pickup. The pickup naturally increases with the amplitude of the sine wave on the transmitter, in this case represented primarily by the coil. There is usually ample pickup for a signal of tens to hundreds of mV on an ungrounded 10:1 oscilloscope probe placed anywhere in the vicinity of the vacuum chamber. Grounding the probe increases the signal by turning the probe into an antenna. It is difficult to maintain high precision

using this method, however, as even a probe secured in place will suffer from the same perturbations in measurement efficiency that affect the resonant circuit itself. This method is better used for quick checks that RF is being transmitted and for passive monitoring of a functioning system than for important measurements of Q and resonant frequency.

3.2.3.2 Effects of resonance on mass spectra

At resonance, we achieve the highest voltage at the ion trap for a given input sine wave amplitude. The result of this is that, at a given point on the input ramp, we measure higher masses. If we sweep frequency with a given input ramp, we will observe that peaks appear to move to lower voltage (that is, they come out sooner, or appear to be at a lower position on the voltage/mass/time axis). If we do not control for the effect of resonance on the trapping voltage, we will also observe that sensitivity decreases as we leave resonance due to the lower trapping voltage. These effects can be observed in Figure 3.4, in which the background carbon dioxide ($^{44}CO_2$) peak is brought in and out of resonance with a fixed input ramp. The efficiency of the circuit declines considerably with small deviations from 1.404 MHz (the resonant frequency as determined by direct measurement of the ratio of the output voltage to the input voltage with a constant amplitude RF potential applied). At 1.404 MHz, the input ramp has a peak amplitude of 0.25 V_{pk}, which produces 1260 V_{pk} on the ring electrode. At 1.394 MHz, the input ramp has the same peak amplitude, but we achieve only 793 V_{pk} on the ring electrode. Note that the sensitivity also appears to decline when the circuit is not at resonance–this is simply because, given

a fixed input signal, the trapping voltage declines along with the ramp amplitude, not because the actual sensitivity of the ion source changes. At 1.404 MHz, we set the trapping voltage to maximize sensitivity for this measurement.

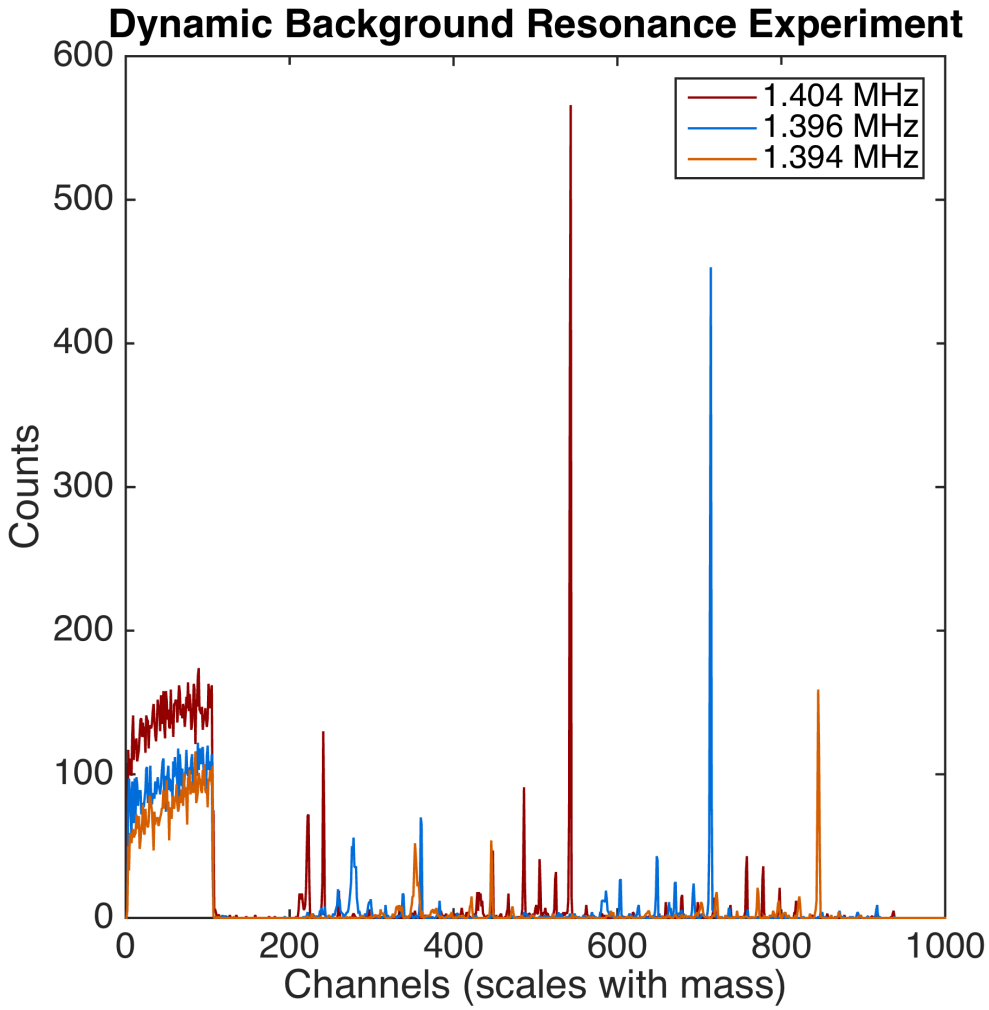

Figure 3.4: Figure showing the effects of resonance on the efficiency of the QIT. The x-axis is left at raw channel number measured from the instrument instead of scaling to mass to illustrate the effect of resonance. The same input ramp is applied to the RF power amplifier in all cases, and the RF power amplifier output has been measured to be linear across this frequency range. The voltage required to reach a given mass is trivially different at these three frequencies, so the differences observed are due entirely to the lower Q of the circuit when not at resonance.

During analysis, fluctuations in environmental conditions can influence the qual-

ity of the resonant circuit and its resonant frequency. This can result in apparent peak migrations, as voltage corresponds linearly to mass/charge during a QIT analysis. If the circuit is placed at resonance at the start of an analysis and then drifts, the ratio of voltage at the ion trap to input voltage will decrease, and peaks will appear to migrate to the right in a plot of measured signal intensity versus mass (~voltage). This is annoying when it occurs over analyses of many hours, as the peaks must be realigned to achieve a usable mass spectrum. It is fatal when it occurs on shorter timescales, as the peaks will be smeared out by jitter and migration, reducing the resolution of analysis. As an extreme example, Figure 3.5 shows the effect of a person walking by an open air core inductor during operation. The figure shows ten one-second integrations of a 50 ms ramp during a measurement of an ^{40}Ar standard. Enclosing the inductor in a metal shield reduces the effect of environmental disturbances such as this on the QIT.

Variations in resonance frequency or quality can be addressed on the timescale of minutes to hours by measuring resonance during analysis with a current sense transformer as described above and then adjusting the input ramp accordingly. Variations on shorter timescales must be avoided by sealing the coil, maintaining a stable vacuum chamber pressure, keeping environmental conditions in the lab constant, and protecting cables and feedthroughs from factors such as moving air, solar heating, and operator contact.

Neglecting the effects of resonance on filtering and the stability the circuit at different frequencies, increasing the operating frequency of the QIT will increase

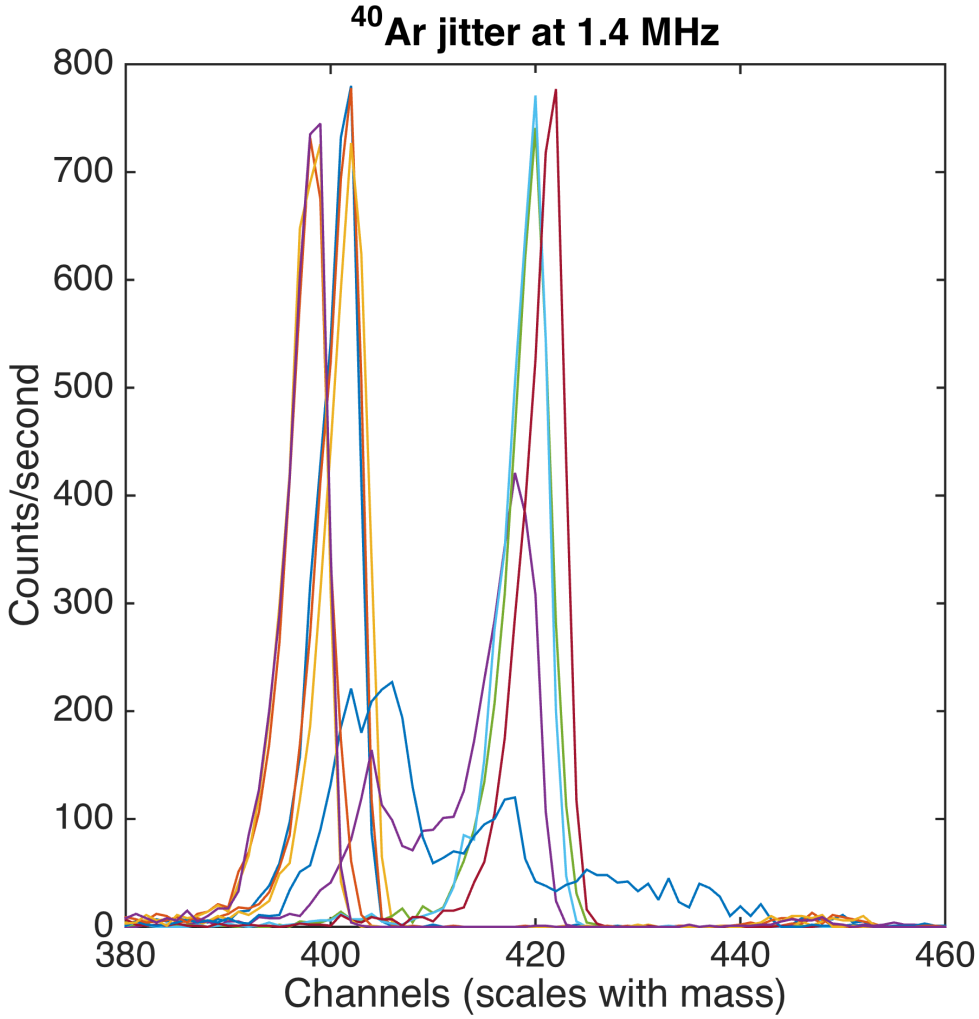

Figure 3.5: The jitter of the ^{40}Ar peak during ten seconds of analysis. A person walked too close to the QIT during this measurement (within about half of a meter), causing a disruption in the RLC circuit that manifested as fluctuations in the voltage applied at the ring electrode. This measurement was abandoned due to the jitter. Smaller effects can be observed due to changes such as the climate control settings in the lab changing at the beginning of the day, tools placed around the QIT, or pressure changes in the instrument. These effects can be greatly reduced by enclosing the inductor in a shield.

the mass resolution of the instrument. This is because the number of ion oscillations before ejection increases with RF drive frequency, which allows for greater confinement (Fischer, 1959) and, more important, because the ejection time for an ion at a given scan rate scales inversely with the frequency of secular motion of the ion,

which in turn scales with the RF drive frequency (Arnold et al., 1994). Scanning speed must be sufficiently low to take advantage of the resolution afforded by the instrument, so highest resolution is typically obtained with a zoom measurement over only a few Da.

3.2.4 RF ramp structure and timing

Assuming that a simple linear increase is used for the RF ramp, the modifications available are the amplitude at the beginning of the ramp (necessarily the same as the trapping voltage), the slope of the ramp, and the maximum amplitude at the end of the ramp.

The trapping voltage is usually a constant low amplitude sufficient to trap the target ions. This can be determined by solving for the mass at the stability limit (q = 0.908) at a given frequency, which is given by the equation:

$$(m/z)_{\text{cutoff}} = \frac{4eV_{pk}}{0.908\Omega^2 r_0^2}$$

where $(m/z)_{\text{cutoff}}$ is the low mass cutoff, e is the elementary charge, V_{pk} is the zero-to-peak amplitude of the RF at the trapping voltage, Ω is the RF drive frequency in rad/s, and r_0 is the radius of the ion trap (10 mm in our case), which is to say that r_0 is the maximum displacement of an ion before it leaves the trapping region.

As mentioned above, the slope of the RF ramp (that is to say, the mass scan speed) can affect the resolution of an ion trap measurement. This is the result of the physical limitations of the electrode at some level, but for practical purposes it is usually limited by the speed of ion detection and the quality of the timing

synchronization in the electronics. For example, at 2 MHz in a 65 pF QIT at a scan rate of 2000 Da/s (typical for a low mass, normal abundance, normal resolution measurement), a timing jitter of 50 μs will limit the mass resolution to 200. When resolution is the primary goal of an experiment, it is therefore advantageous to operate at a low slope over the mass range of interest. This is also true when large peaks must be measured; in this case, the slope must be reduced to the point that the detector is not saturated during the measurement of the peak.

The maximum amplitude of the RF ramp is determined simply by the highest mass one wishes to measure. This can be easily calculated from the trap capacitance and RF drive frequency, and the current necessary can then be determined by calculating the trap reactance at that frequency.

3.3 Demonstrated capabilities and development targets

Most of the first measurements on the Caltech QIT have been made using a resonant frequency of 1.4 MHz and a ^{40}Ar standard containing 2.75×10^{-8} cc STP, or about 1.22×10^{-12} moles of pure ^{40}Ar. We plan to test other inductors and to measure other noble gases soon, but this has served as the benchmark for testing electronics and measurement schemes. The dynamic background of the QIT after bakeout, at a pressure of about 1.5×10^{-9} Torr, is shown in Figure 3.6.

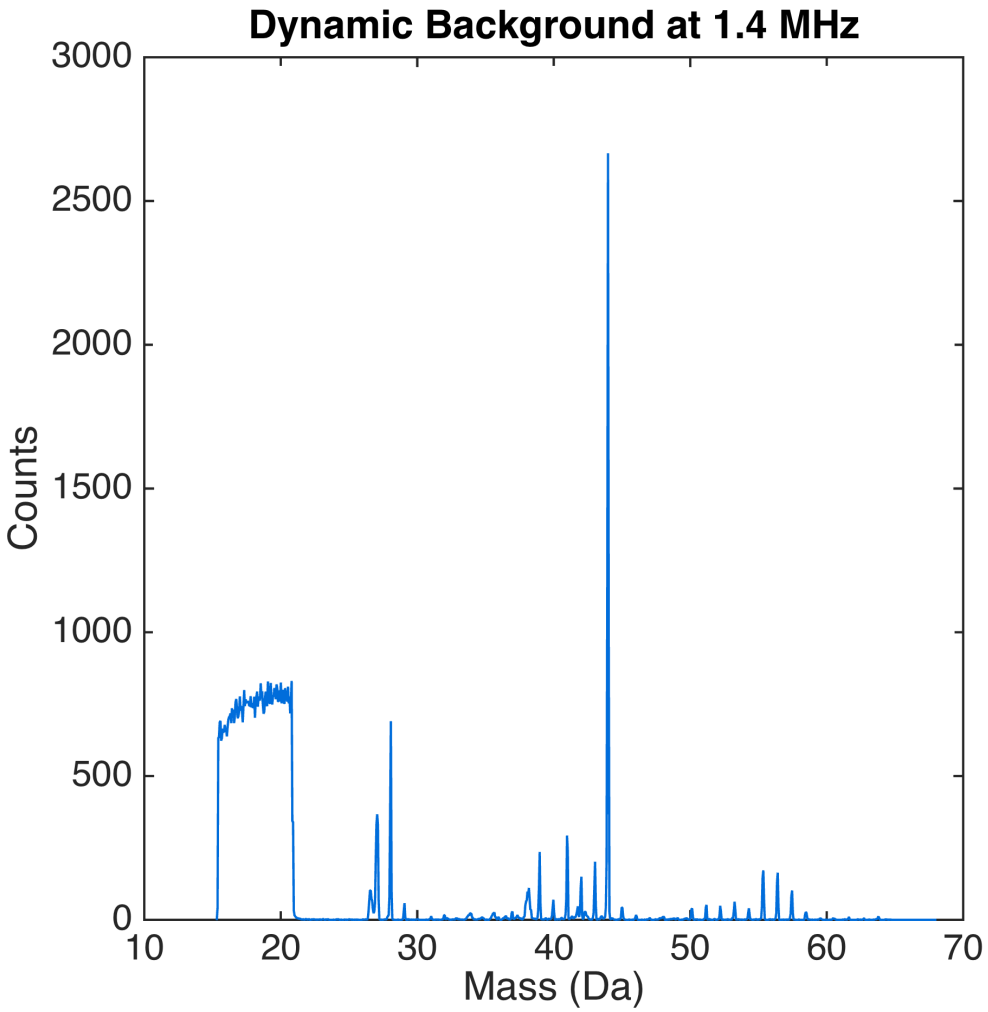

Figure 3.6: The dynamic background of the QIT at 1.5×10^{-9} Torr pressure with a cold St101 getter, the filament set to 1.55 A, and the measurement taken at an RF drive frequency of 1.404 MHz.

3.3.1 Sensitivity, background noise, Ar consumption, Ar rise rate, and mass resolution

The Caltech QIT is in the early stages of development, but it has already shown promise as a next generation noble gas mass spectrometer. We measured the sensitivity of the QIT using a manometrically calibrated ^{40}Ar standard at 1.4 MHz RF drive frequency. At a filament current of 1.55 A, we measure a sensitvity on

^{40}Ar of about 4×10^{11} cps/Torr (Figure 3.7), using an approximate chamber volume of 2000 cc. We have not fully explored the tuning parameter space of the QIT, but this provides a good starting point. At the filament setting of 1.55 A during this measurement, the filament produces approximately 20 μA of emission. It is capable of operating up to 1.8 A (with reduced lifetime), at which point it produces more than 100 times as much emission. However, increasing the current to 1.65 A, which should yield an increase of about a factor of 20 in emission, only increases ^{40}Ar sensitivity by about 12% over the number stated above. Clearly, some part of the parameter space remains to be explored. By comparison, the highest sensitivities claimed by the more established QIT systems at JPL are in the range of 10^{15} cps/Torr (Darrach, Madzunkov, et al., 2015), although these are not measured against a manometer at static vacuum.

More important at this stage than the absolute sensitivity, which we expect will improve dramatically once we are able to take advantage of the full emission of the filament, is the fact that the sensitivity appears stable for many hours. As an example, we show the absolute sensitivity of a single ^{40}Ar standard over an hour of measurement in Figure 3.7. We measured the ^{40}Ar rise rate in this chamber at 0.024 cps/second, or 86 cps/hour, less than 2% of the total standard size and about the standard deviation of the measured absolute sensitivity. Therefore, we conclude that the ^{40}Ar sample is not being consumed by the mass spectrometer, as one might expect given the mode of analysis. Unlike a magnetic sector mass spectrometer, the QIT does not use a high voltage source to accelerate ions. We hypothesize,

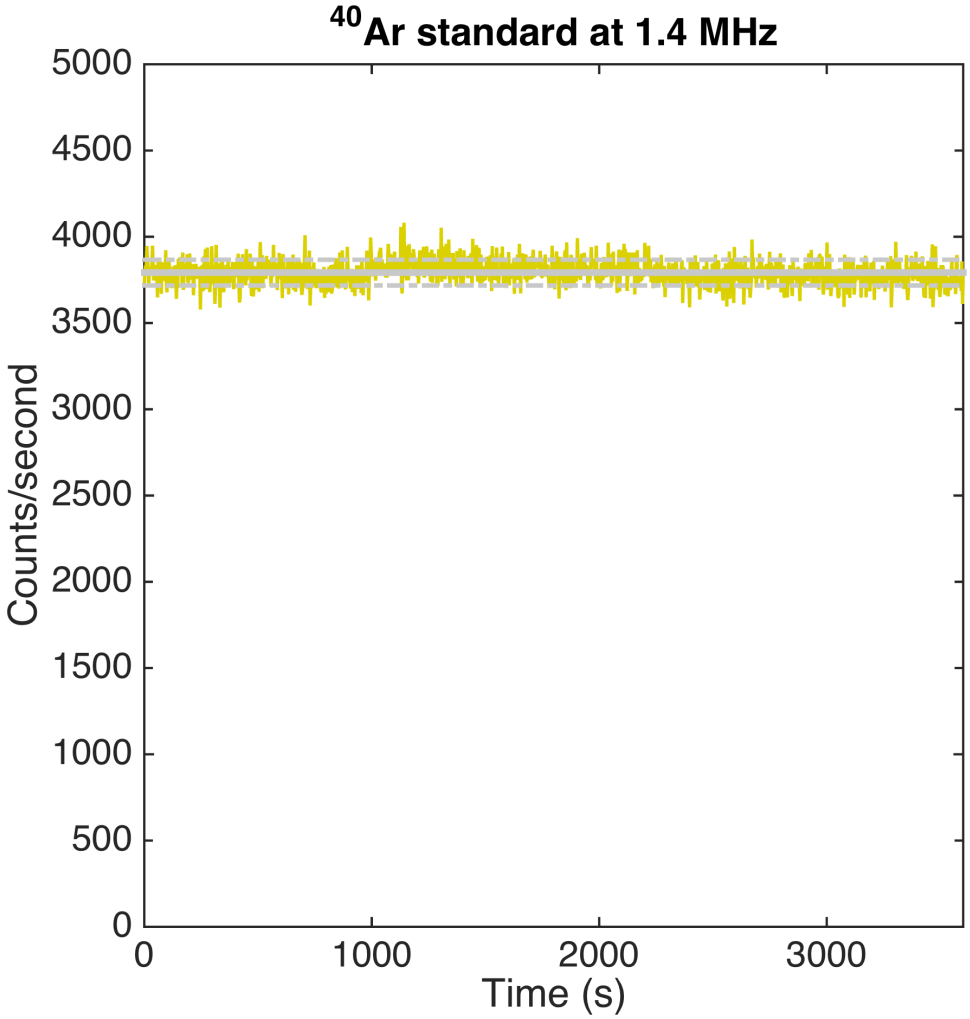

Figure 3.7: Sensitivity of the QIT measured on a ^{40}Ar standard of 2.75×10^{-8} cc STP, or about 1.22×10^{-12} moles. The yellow trace shows the integrated peak area in counts/second for one hour. The grey lines show the mean value of the peak area and the 1σ standard deviations from the mean. The sensitivity appears stable, and the sample does not appear to be consumed. In contrast, a magnetic sector mass spectrometer consumes about 10% of a Ne standard per hour, and given the higher ionization cross section for Ar would consume an Ar sample even more quickly.

therefore, that the low energy ions created in the trap are either analyzed or simply return to the neutral gas mixture in the chamber to be analyzed again. This means that, within the limits of chamber cleanliness, one could analyze a sample for an indefinite period of time until all gas particles have been measured.

This gain comes in addition to the low detector noise of the QIT. We currently measure about 0.012 cps of noise per peak width at the top of the RF ramp shown in Figure 3.6, where the RF-induced noise is highest. We have not yet attempted to minimize this noise level except by adjusting the preamplifier counting threshold by eye, so it is likely that we could reduce it further. The final noise value will likely be between 0.012 cps and 0.0025 cps, which is the detector specified dark noise of < 0.1 cps scaled by the duty cycle per peak at this ramp and frequency. Note that it is possible to perform wider mass scans in order to shrink the peak width without losing sensitivity if it is important to reduce dark noise further.

We have also not fully explored the frequency range of the Caltech QIT, but we have tested two inductors so far. One has an inductance of about 200 μH, which yields a resonant frequency of about 1.4 MHz. This is the inductor that we used for the sensitivity measurements above. At this frequency, the QIT has a mass resolution of 300 at mass 40 (Δm = 0.13, full width at half maximum), which is better than many commercial quadrupole mass spectrometers (Figure 3.8). Mass resolution scales with mass on the QIT, so this is equivalent to a resolution of only 30 at mass 4.

The other inductor we have tested has an inductance of about 26 μH, which yields a much higher resonant frequency of about 3.8 MHz. At this frequency, the QIT draws considerably more power, which poses a challenge on several levels. While we can produce enough power to reach at least the Kr mass range, the RF power required to reach above mass 30 produces unacceptable noise on the detector preamplifier.

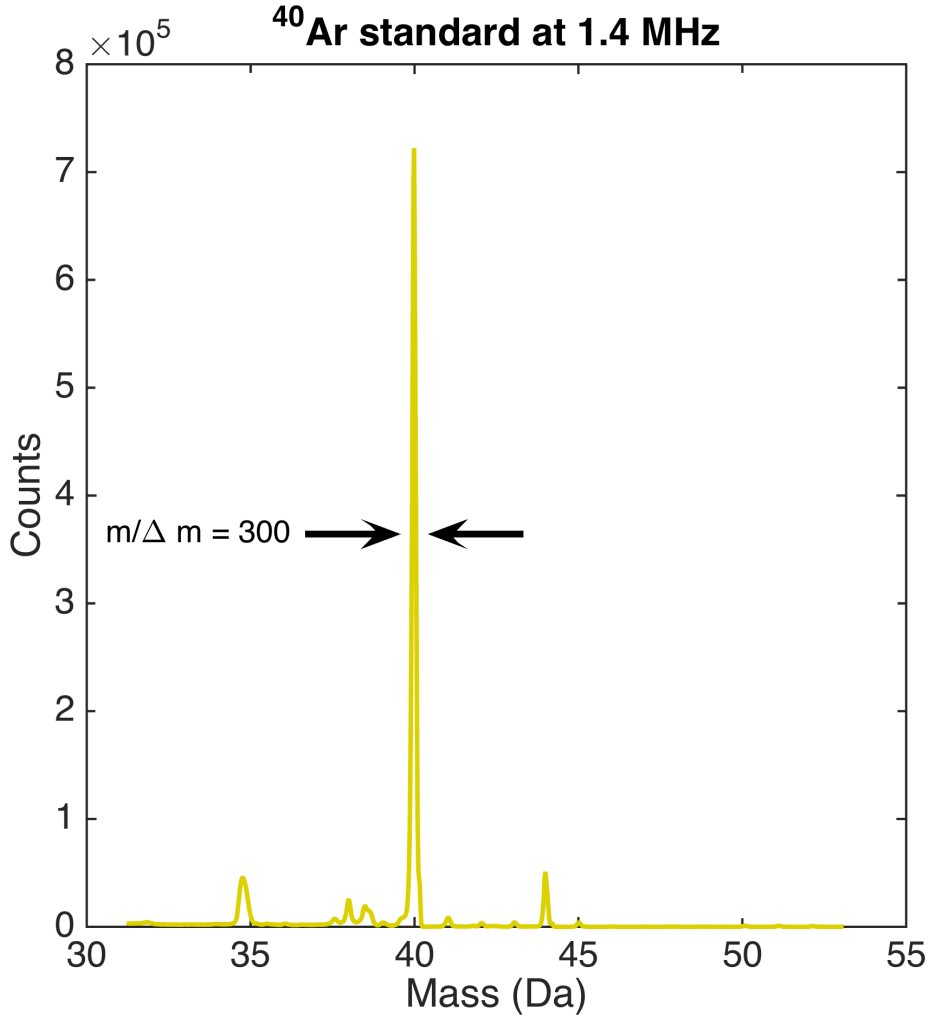

Figure 3.8: The mass resolution of the QIT measured on a ^{40}Ar standard of 2.75×10^{-8} cc STP, or about 1.22×10^{-12} moles.

Until we have isolated the preamplifier more effectively from the RF circuit, we cannot test the ^{40}Ar standard at this frequency. However, we have measured the background mass range up to mass 28 and found a mass resolution of about 700, comparable to most commercial magnetic sector noble gas mass spectrometers. Furthermore, we find that the RF power amplifier is less stable at this frequency, so the gain appears to vary with a short timescale. Once we implement a feedback to stabilize the RF ramp by measuring the current draw by the circuit with a current

sense transformer, we expect that the mass resolution at this frequency to increase.

On a similar system at JPL, I have measured a mass resolution of about 800 on mass 4 (Δm = 0.005, full width at half maximum) at 4.2 MHz (Figure 3.9). This system uses a side ionization QIT in a UHV chamber just like the one at Caltech, and I am also using an E&I 2200L power amplifier. The signal source in this case is a Red Pitaya. The reason for the significantly better resolution on this system is likely the stability of the circuit, which is much better at the relatively low power levels required to reach mass 4 than at mass 40. It is not possible to do a direct comparison at mass 40 because the RF noise level becomes unacceptable on the preamplifier before we reach mass 10. However, we are able to run this system at 5.7 MHz to look at mass 4, and we observe that the resolution actually decreases due to the increased instability of the circuit.

This resolution would be adequate for measuring ^{3}He given ^{3}He and ^{1}H^{2}H peaks of similar size. The equivalent resolution at mass 3 is 600, which is about the standard achieved by the previous generation of commercial magnetic sector mass spectrometers. However, this is a mass resolution measured using the peak width at half the maximum value, and the peak shape is not flat-topped on a time of flight instrument like it is on a magnetic sector mass spectrometer. Because the QIT peaks have characteristically longer tails on the low mass side, the contribution at the ^{3}He peak position from ^{1}H^{2}H calculated from the ^{4}He peak in Figure 3.9 will be about 2% of the ^{1}H^{2}H peak height.

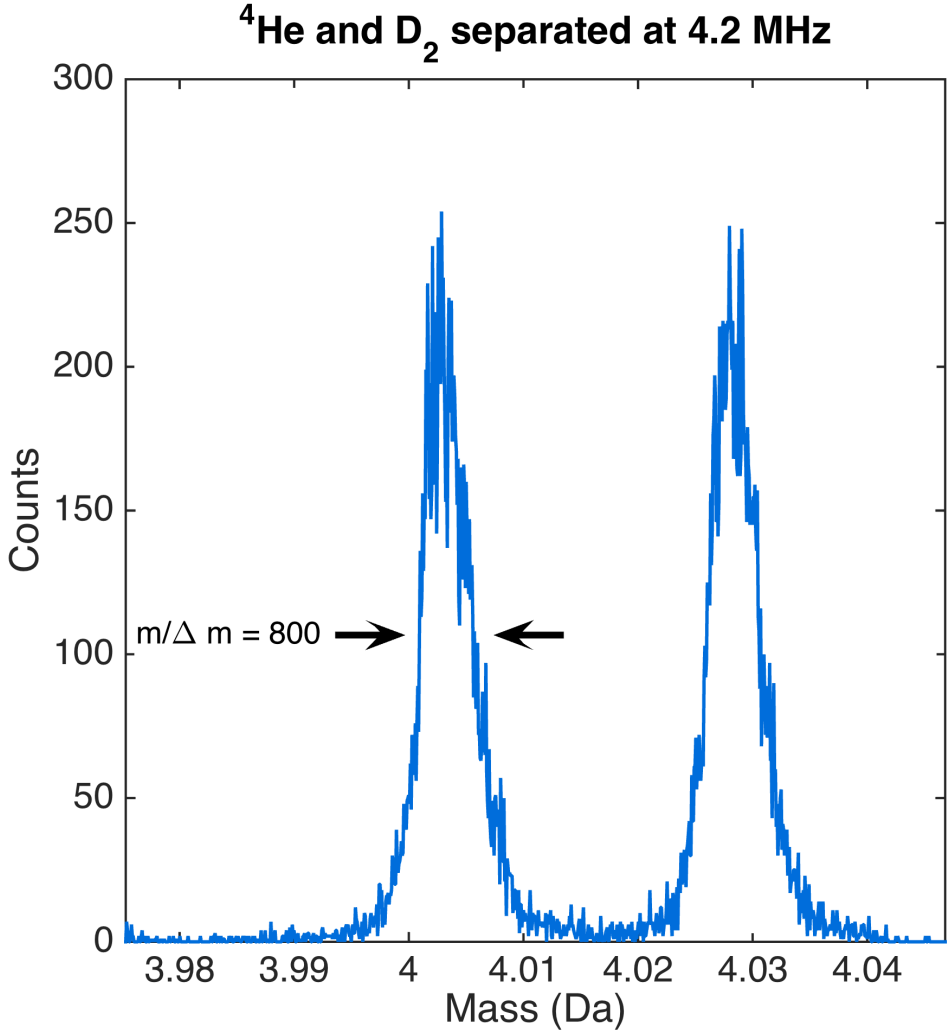

Figure 3.9: Figure showing the mass resolution of the QIT measured on a mixed ^{4}He-D_2 pure gas mixture introduced through a leak valve.

3.3.2 Ongoing work

We have two primary development targets that we are pursuing in parallel on the Caltech QIT: measuring Xe species to search for primordial variations in the solid Earth and measuring He species to demonstrate resolution of ^{3}He from ^{1}H^{2}H. The former does not require high resolution (achieving the resolution of about 600 required to resolve all significant interferences in the Xe mass range is equivalent to a resolution of only around 300 at mass 40), but it does require good sensitivity

and low noise. The latter is a much more significant mass resolution challenge, as achieving the same resolution of 600 at mass 3, which is necessary to separate ^{3}He from ^{1}H^{2}H, is equivalent to a resolution of 8,000 at mass 40. Because we cannot produce enough RF power to measure the Xe masses using the inductors necessary to achieve this resolution at mass 3, these development projects are proceeding with a suite of inductors that allow us to tune the circuit for the task at hand.

There are many avenues of potential improvement that we have not explored using the JPL QIT. For example, we have not fully explored the possibility of varying the trapping potential and the cooling potential (the RF drive potential after ionization ceases but before the ramp begins), which could improve cooling and therefore resolution without loss of sensitivity. We have not yet implemented a feedback loop on the Caltech QIT to continuously adjust the RF potential during trapping and during the ramp in response to small changes in the RLC circuit, but we have found that this provides a significant improvement in stability at JPL. In addition to these and many other unexplored paths for improvement, there are three main limitations that we have already identified that must be overcome during the next stage of development:

The sensitivity of the preamplifier to high frequency RF We have determined that we cannot produce, for example, enough power to reach mass 40 at 5 MHz with our current RF power amplifiers. However, we have not tried to push the boundaries of the capabilities of these amplifiers because the current limit on our ability to measure at high frequency and high power is the sensitivity of the Amptek A121

preamplifier and associated electronics to noise induced by the RF. At frequencies over 3 MHz, on both the Caltech and the JPL systems, we find that the upper mass limit is always determined by the onset of RF noise at a level that cannot be addressed by the discrimination setting on the preamplifier. However, we observe that the Burle 5900 Channeltron produces ample current pulses. The peaks are still visible above the noise until the amplifier is fully saturated by RF noise. Therefore, it should be possible to discriminate the noise from the signal, possibly just by introducing larger chokes or resistors to the signal line from the Channeltron or by otherwise attenuating the Channeltron signal, or by operating the Channeltron at lower saturation, or by better isolation the preamplifier.

The impedance match from the RF power amplifier to the RLC circuit We know that the impedance of the circuit increases as a function of frequency because parasitic impedance always increases with frequency, and we know that the DC resistance of the RLC circuit is usually a few Ω. We currently use a 50-Ω to 3-Ω impedance matching transformer on the E&I 2200L power amplifier, and no transformer on the smaller JPL amplifiers. The 2200L measured reflected power, so we can observe that as we increase frequency from below 1 MHz, the reflected power to forward power ratio measured by the amplifier increases from negligible to almost 1 by 3.8 MHz. This is consistent with the expectation that the impedance of the circuit increases to tens of Ω at high frequency. The impedance mismatch means that we cannot deliver the full capability of the amplifier to the circuit at high frequency, when it is most necessary, and also that there is wasted power that may

be contributing to the high noise levels that we observe at high frequency. This could potentially be addressed by a variable impedance transformer, which we can purchase or build easily.

The feedthroughs and connections for the RF power Most of the JPL instruments use solid conductor feedthroughs intended for DC high voltage for the RF connections between the electronics and the vacuum chamber. We use a large RF power feedthrough on the Caltech system, but we cannot water cool it due to the fact that it must terminate in vacuum at the ring electrode. In addition, we have no way to make connections to any of the three electrodes except through small tapped holes in each. Commercial QIT mass spectrometers typically employ welded blades that present a much larger surface area to the RF, and we know from observing the pressure on ion gauges and the mass spectrum that high power causes significant heating of the vacuum system in our instruments. This very likely contributes to the instability that we observe in the Q of the RLC circuit at high frequency, which limits the resolution that we can achieve, especially with long, low abundance measurements such as ^{3}He. A better design of the electrodes would permit a solid connection to be made with a similar surface area between the inductor, the vacuum feedthrough, and the ring electrode, and also between the end cap electrodes, the vacuum feedthroughs, and the return path to the RF power amplifier.

Additionally, we observe that the Q of various inductors on the Caltech QIT is much lower than we observed at JPL, by a factor of about 5. The reasons for this are not clear, but the primary difference between the systems is the choice of

feedthrough. It might be the case that the large block of alumina ceramic on the RF power feedthrough stifles the Q of the system, much as we have observed at JPL that alumina forms lower the Q of inductors.

3.4 Conclusions

The quadrupole ion trap shows great promise as a tool for measuring noble gases in static vacuum. Its mass resolution, scan speed, and signal/noise ratio easily exceed those of magnetic sector mass spectrometers. These strengths mean that it will find laboratory applications in the measurement of rare species and noble gas mixtures in which multiple elements or many isotopes must be recorded. It is also small and efficient, raising the possibility of portable applications beyond those on space missions, such as in underwater gliders or in volcano monitoring. The primary development targets for the QIT at Caltech are absolute sensitivity and electronic stability, as these are the properties that currently limit the widespread adoption of this technology. The progress we have made so far demonstrates the power and versatility of the QIT mass spectrometer.

References

Allen, J. S. (1939). “The Detection of Single Positive Ions, Electrons and Photons by a Secondary Electron Multiplier”. In: *Physical Review* 55.10, pp. 966–971.

Arnold, N. S., C. Hars, and H. L. C. Meuzelaar (1994). “Extended theoretical considerations for Mass resolution in the resonance ejection mode of quadrupole Ion Trap Mass Spectrometry”. In: *Journal of the American Society for Mass Spectrometry* 5.7, pp. 676–688.

Bainbridge, K. T. and E. B. Jordan (1936). “Mass Spectrum Analysis 1. The Mass Spectrograph. 2. The Existence of Isobars of Adjacent Elements”. In: *Physical Review* 50.4, pp. 282–296.

Barber, N. F. (1933). “Note on the shape of an electron beam bent in a magnetic field”. In: *Proc. Leeds Philos. Lit Soc., Sci. Sect.*

Baur, H. (1999). “A Noble-Gas Mass Spectrometer Compressor Source With two Orders of Magnitude Improvement in Sensitivity”. In: *Eos, Transactions American Geophysical Union*. American Geophysical Union Fall Meeting.

Biemann, K. et al. (1976). “Search for Organic and Volatile Inorganic Compounds in Two Surface Samples from the Chryse Planitia Region of Mars”. In: *Science* 194.4260, pp. 72–76.

Crowther, S. A., R. K. Mohapatra, G. Turner, D. J. Blagburn, K. Kehm, and J. D. Gilmour (2008). “Characteristics and applications of RELAX, an ultrasensitive resonance ionization mass spectrometer for xenon”. In: *Journal of Analytical Atomic Spectrometry* 23.7, pp. 938–947.

Darrach, M. R., A. Chutjian, et al. (2012). “Trace Chemical and Major Constituents Measurements of the International Space Station Atmosphere by the Vehicle Cabin Atmosphere Monitor”. In: *42nd International Conference on Environmental Systems*. Reston, Virigina: American Institute of Aeronautics and Astronautics.

Darrach, M., S. Madzunkov, and R. Schaefer (2015). “The Mass Analyzer for Real-time Investigation of Neutrals at Europa (MARINE)”. In: *2015 IEEE Aerospace Conference*.

Dawson, P. H. (1969). “A Simple Mass Spectrometer”. In: *Review of Scientific Instruments* 40.11, p. 1444.

Dempster, A. J. (1918). “A new Method of Positive Ray Analysis”. In: *Physical Review* 11.4, pp. 316–325.

Ezell, E. C. and L. N. Ezell (1984). “On Mars”. In: *On Mars: Exploration of the Red Planet. 1958-1978*. Washington, DC: NASA.

Farley, K. A., C. Malespin, P. Mahaffy, and J. P. Grotzinger (2014). “In Situ Radiometric and Exposure Age Dating of the Martian Surface”. In: *Science* 343.

Farley, K. (2000). “Helium diffusion from apatite: General behavior as illustrated by Durango fluorapatite”. In: *Journal of Geophysical Research* 105.B2, pp. 2903–2914.

Fischer, E. (1959). “Die dreidimensionale Stabilisierung von Ladungstragern in einem Vierpolfeld”. In: *Zeitschrift für Physik* 156.1, pp. 1–26.

Hoffman, J. H. (1972). “Lunar orbital mass spectrometer”. In: *International Journal of Mass Spectrometry and Ion Physics* 8.4, pp. 403–416.

Hoffman, J. H., R. C. Chaney, and H. Hammack (2008). “Phoenix Mars Mission—The Thermal Evolved Gas Analyzer”. In: *Journal of the American Society for Mass Spectrometry* 19.10, pp. 1377–1383.

Hoffman, J. H., T. P. Griffin, T. Limero, and C. R. Arkin (2010). "Space Applications of Mass Spectrometry". In: *Applied Mass Spectrometry Handbook*. Ed. by M. Lee.

Istomin, V. G. and K. V. Grechnev (1976). "Argon in the Martian atmosphere: Evidence from the Mars 6 descent module". In: *Icarus* 28.2, pp. 155–158.

James, J. T., T. F. Limero, H. J. Leano, J. F. Boyd, and P. A. Covington (1994). "Volatile organic contaminants found in the habitable environment of the Space Shuttle: STS-26 to STS-55." In: *Aviation, space, and environmental medicine* 65.9, pp. 851–857.

Lee, J. Y., K. Marti, J. P. Severinghaus, and K. Kawamura (2006). "A redetermination of the isotopic abundances of atmospheric Ar". In: *Geochimica et Cosmochimica Acta* 70, pp. 4507–4512.

Liebich, H. M., W. Bertsch, A. Zlatkis, and J. Schneider (1975). "Volatile organic components in the Skylab 4 spacecraft atmosphere." In: *Aviation, space, and environmental medicine* 46.8, pp. 1002–1007.

Madzunkov, S. M. and D. Nikolić (2014). "Accurate Xe isotope measurement using JPL ion trap." In: *Journal of the American Society for Mass Spectrometry* 25.11, pp. 1841–1852.

Mahaffy, P. R. et al. (2012). "The Sample Analysis at Mars Investigation and Instrument Suite". In: *Space Science Reviews* 170.1-4, pp. 401–478.

March, R. E. (2009). "Quadrupole ion traps". In: *Mass spectrometry reviews* 28.6, pp. 961–989.

Nier, A. O. and M. B. McElroy (1977). "Composition and structure of Mars' Upper atmosphere: Results from the neutral mass spectrometers on Viking 1 and 2". In: *Journal of Geophysical Research* 82.28, pp. 4341–4349.

Nier, A. O. (1936). "A Mass-Spectrographic Study of the Isotopes of Argon, Potassium, Rubidium, Zinc and Cadmium". In: *Physical Review* 50.11, pp. 1041–1045.

Orient, O. J. and A. Chutjian (2002). "A compact, high-resolution Paul ion trap mass spectrometer with electron-impact ionization". In: *Review of Scientific Instruments* 73.5, p. 2157.

Papanastassiou, D. A., G. J. Wasserburg, and D. S. Burnett (1970). "Rb-Sr ages of lunar rocks from the sea of tranquillity". In: *Earth and Planetary Science Letters* 8.1, pp. 1–19.

Paul, W. (1990). "Electromagnetic traps for charged and neutral particles". In: *Reviews of modern physics* 62, pp. 531–540.

Paul, W. and H. Steinwedel (1956). *Verfahren zur Trennung bzw. zum getrennten Nachweis von Ionen verschiedener spezifischer Ladung*. German Patent DE944900.

Paul, W. and H. Steinwedel (1953). “Ein neues Massenspektrometer ohne Magnetfeld”. In: *Zeitschrift für Naturforschung A* 8.7, pp. 448–450.

Ramisetty, R. (2015). “A new Time-Of-Flight Mass Spectrometer (TOF-MS) for noble gas analysis”. PhD thesis. Universitat Bern.

Reynolds, J. H. (1956). “High Sensitivity Mass Spectrometer for Noble Gas Analysis”. In: *Review of Scientific Instruments* 27.11, pp. 928–934.

Slepian, J. (1923). “Hot-cathode tube”.

Stafford, G. C., P. E. Kelley, J. E. P. Syka, W. E. Reynolds, and J. F. J. Todd (1984). “Recent improvements in and analytical applications of advanced ion trap technology”. In: *International Journal of Mass Spectrometry and Ion Processes* 60, pp. 85–98.

Thomson, J. J. (1913). “Bakerian Lecture: Rays of Positive Electricity”. In: *Proceedings of the Royal Society of London*, pp. 1–20.

Chapter 4

Insights Into the Age of the Mono Lake Excursion and Magmatic Crystal Residence Time from (U–Th)/He and ^{230}Th Dating of Volcanic Allanite

Abstract

We present new data for the age of the Mono Lake Excursion at its type locality. Using the (U–Th)/He system on allanite, we dated Wilson Creek Ash 15 (Lajoie, 1968) to 38.7 ± 1.2 ka (2 SE). The new age for this ash supports the hypothesis (Kent et al., 2002; Zimmerman, Hemming, Kent, et al., 2006) that the Mono Lake Excursion is coincident with, and probably the same event as, the Laschamp Geomagnetic Excursion (40.4 ± 2 ka), an event that shares similar magnetic characteristics with the excursion identified at Mono Lake. We also estimate an allanite magma residence time of slightly less than 30 ka based on ^{230}Th/^{238}U disequilibrium and the (U–Th)/He-based eruption age.

4.1 Introduction

Mono Lake is a closed-basin lake in the western Great Basin, east of the Sierra Nevada in California. The ancient lake sediments of the Mono Basin contain important regional climate records (Russell, 1889; Lajoie, 1968; Stine, 1987; Benson, Currey, et al., 1990; Stine, 1990b; Stine, 1990a; Bursik and Gillespie, 1993; Benson, Burdett, et al., 1997; Benson, Lund, et al., 1998; Davis, 1999; Reheis et al., 2002; Zimmerman, Hemming, Kent, et al., 2006; Graham and Hughes, 2007; Zim-

merman, Pearl, et al., 2011; Zimmerman, Hemming, Hemming, et al., 2011) that can be dated in a relative sense by correlation of the volcanic ashes that occur throughout the basin. The Upper Pleistocene Wilson Creek Formation (WCF), first mapped by Lajoie (1968), comprises unconsolidated lake sediments punctuated by eighteen rhyolitic ashes and one basaltic ash that have been numbered and bundled into marker sequences. These ashes can be identified with confidence simply based upon outcrop appearance and stratigraphic order.

While these ashes provide closely spaced relative age constraints for climate records from the last glacial period in the Mono Basin, absolute ages are difficult to obtain due to the youth of the ashes and geochemical complications in Mono Lake. Low in situ produced daughter product concentrations and uncertainty about initial compositions and secular equilibrium pose challenges for most radiometric dating systems in such juvenile materials. While ^{14}C dating is frequently used for materials younger than 50 ka, several unique problems such as a large and almost certainly time-varying dead carbon reservoir and extreme carbonate chemistry plague radiocarbon dating attempts in this hypersaline alkaline lake (Benson, Currey, et al., 1990; Kent et al., 2002; Zimmerman, Hemming, Kent, et al., 2006; Cassata et al., 2010). $^{40}Ar/^{39}Ar$ dating of several WCF ashes suffers from significant variability due to inheritance and high uncertainties in the results (Chen et al., 1996; Kent et al., 2002; Zimmerman, Hemming, Kent, et al., 2006; Cassata et al., 2010). In this work, we present new (U–Th)/He eruption age data for allanites from the ash associated with the prominent magnetic excursion known as the Mono Lake Excursion (Lid-

dicoat and Coe, 1979; Lund et al., 1988) at its type locality and also present U–Th disequilibrium data that bears on the allanite crystal residence time in the magma chamber.

4.2 Geologic Background

4.2.1 The age of Ash 15 in the Wilson Creek Formation

One of the most intriguing WCF ashes is Ash 15 (Lajoie, 1968), which bisects a geomagnetic excursion first identified by Denham and Cox (1971), who were in search of expressions of the Laschamp Excursion. Because the excursion appeared to lack the negative inclinations characteristic of the Laschamp Excursion, and because existing age estimates led them to think this excursion was too old to be the Laschamp, Denham and Cox (1971) concluded that the Laschamp Excursion was not present in the section, and that they had identified a previously unknown excursion. Liddicoat and Coe (1979) better characterized this event and named it the Mono Lake Excursion.

In the following decades, the age of the Laschamp Excursion was refined to 40.4 ± 2 ka (Guillou et al., 2004). Many authors now believe that the Mono Lake Excursion must be younger than this, at ~32–34 ka, based on a carbonate radiocarbon timescale and correlation to a contemporaneous geomagnetic excursion present in some marine records (Benson, Lund, et al., 1998; Benson, Liddicoat, et al., 2003; Laj et al., 2004; Cassata et al., 2010).

New dating efforts have substantially revised the timescale of the Wilson Creek Formation (Benson, Lund, et al., 1998; Kent et al., 2002; Benson, Liddicoat, et al.,

2003; Zimmerman, Hemming, Kent, et al., 2006; Cassata et al., 2010). Carbonate U–Th disequilibrium dating of cross cutting calcite indicates that the formation extends to at least 49 ka (Xianfeng Wang, unpublished ^{238}U-^{230}Th measurement, personal communication), and it almost certainly extends to greater than 60 ka (Kent et al., 2002; Zimmerman, Hemming, Kent, et al., 2006; Cassata et al., 2010). It is clear that the two geomagnetic excursions observed between 30 and 45 ka in some marine records (Laj et al., 2004) fall within the time span of the apparently continuous high-resolution sediment record at Mono Lake.

Liddicoat and Coe (1979) demonstrated the presence of negative inclinations in the event at Mono Lake, casting doubt on the original evidence that precluded the event in Mono Lake from being the Laschamp. One possibility is that the Mono Lake Excursion is in fact the Laschamp Excursion, as suggested by Kent et al. (2002) based on the constraints that radiocarbon ages represent minimum depositional ages and that the ^{40}Ar/^{39}Ar sanidine ages represent maximum depositional ages.

Zimmerman, Hemming, Kent, et al. (2006) created a timescale for the WCF based on a correlation of the paleomagnetic record in the sediments to the GLOPIS stack (Laj et al., 2004). In this timescale, Ash 15 falls at 39.8 ka, overlapping the Laschamp Excursion at its type locality. Ash 15 is about 20 cm above the paleointensity low in the Mono Lake record, which has an average sedimentation rate of ~20 cm/ka (Zimmerman, Hemming, Kent, et al., 2006). Models that place the excursion preserved in the Mono Lake sediments near 34 ka and fit the Laschamp to another feature in the paleointensity record either directly violate concordant

radiocarbon and $^{40}Ar/^{39}Ar$ ages higher in the core, imply large fluctuations in sedimentation rates that are not correlated with any known tectonic, volcanic, or climatic events (Zimmerman, Hemming, Kent, et al., 2006), or produce significant mismatch of the paleointensity patterns at the key interval of interest (Cassata et al., 2010). Attempts to constrain the entirety of the Wilson Creek Formation to the time period after the Laschamp (e.g., Model B in Cassata et al. 2010) are unable to produce a feasible paleomagnetic correlation and imply even larger fluctuations in sedimentation rate. Cassata et al. (2010) force the paleomagnetic intensity minimum in the Mono Lake record to correspond to a 34 ka minimum in the GLOPIS record and argue that the low sedimentation rates implied before 34 ka would not have captured the Laschamp. However this line of reasoning demands independent evidence for such a sedimentation rate change, which is currently lacking.

Even when excursions and reversals are well expressed globally, single paleomagnetic records are fragmented due to inconsistent sedimentation and may not preserve such short duration events (Coe et al., 2004). The difficulty of resolving short events in a single paleomagnetic record and the uncertainties in correlation pointed out by Cassata et al. (2010) demand a direct date for the excursion.

4.2.2 (U–Th)/He dating of juvenile materials

Dating of young volcanic samples using the (U–Th)/He system can be undertaken on uranium- and thorium-rich minerals that quantitatively retain helium, such as zircon, monazite, xenotime, sphene, allanite, and garnet. For example, Aciego et al. (2003) dated garnets from the 79 AD eruption of Mount Vesuvius, and Farley, Kohn,

et al. (2002) dated apatite and zircon from the 330 ka Rangitawa tephra. Davidson et al. (2004) demonstrated the application of the (U–Th)/He chronometer to young volcanic rocks that cannot be easily dated using the $^{40}Ar/^{39}Ar$ technique. Application of this method to samples with such young crystallization ages requires potentially uncertain uranium-thorium disequilibrium corrections that must be measured or modeled. Thus in many cases the precision of the radiocarbon and $^{40}Ar/^{39}Ar$ systems is superior. However, lack of appropriate material, contamination, inheritance, and other problems sometimes favor use of the (U–Th)/He technique. Ash 15, which cannot be reliably dated using more established techniques (Zimmerman, Hemming, Kent, et al., 2006; Cassata et al., 2010), is one such case.

Allanite ($(Ca,REE)_2Al_2Fe_2Si_3O_{12}OH$) is an epidote group mineral common in Ash 15. It typically carries high concentrations of thorium, in this case up to 1 wt. % (Table 4.1), making it an appealing choice for dating of very young samples. Previous (U–Th)/He dating of allanite is very limited: Wolf (1997) dated a sample from the Peninsular Ranges batholith and concluded this phase has a He closure temperature $> 100°C$. Ash 15 is an unwelded tephra deposit, indicating that pumice lapilli cooled to very low temperatures during ascent and fall, a geologically instantaneous event. The deposit was never deeply buried or heated, so the observation of Wolf (1997) is sufficient to ensure quantitative retention of He in the allanite beginning immediately after eruption and deposition.

4.2.3 Magmatic crystal residence time from ^{238}U-^{230}Th disequilibrium

Disequilibrium in the actinide decay chains at the time of eruption violates the assumption of secular equilibrium that underlies standard helium dating, and can lead to erroneous ages in young samples due to the different decay rates of different isotopes of U and Th (Farley, Kohn, et al., 2002). Isotopic disequilibrium must therefore be measured in order to date young samples. Because U and Th are retained after crystallization in minerals such as allanite (Vazquez and Reid, 2004) and zircon (e.g., Schmitt et al. 2003; Crowley et al. 2007), this disequilibrium can also be used as a crystallization chronometer. The ratio of the current excess of a given isotope that is out of equilibrium (^{230}Th in this study) to the initial excess at the time of crystallization, which can be inferred based on the observed partitioning of more stable isotopes of the same element, is a function of the time since crystallization. In conjunction with an eruption chronometer such as a (U–Th)/He age, this allows the calculation of a residence time in the magma for the crystal.

4.3 (U–Th)/He and ^{230}Th Dating Methods

4.3.1 Sampling and Allanite Separation

We collected Ash 15 at the South Shore outcrop (37°59′11″N, 118°54′44″W) on the southeast shore of modern Mono Lake. After removing the ~50 cm weathered layer of the outcrop, we removed clean samples of the ash with a spackling knife. We took the sample from the uppermost coarse layer of the 24 cm unconsolidated ash bed, which has distinctive layering (Figure 4.1. We washed the sample in a 63

μm sieve and processed the coarse fraction first through lithium heteropolytungstate (ρ = 2.85) and then methylene iodide (ρ = 3.32). We then removed ferromagnetic minerals from the high density fraction with a hand magnet and hand picked the remaining material for allanite. We selected allanite grains for large size, physical integrity, and the presence of glass adhering to the edges of the crystals. Figure 4.2 shows a representative grain, which is approximately 450 x 275 μm. Because allanite is almost opaque, it is not possible to avoid inclusion-bearing crystals, but the large amounts of U and Th present in the allanite suggest that He ingrowth in inclusions is unimportant.

Figure 4.1: Ash 15 at the South Shore outcrop (37°59'11"N, 118°54'44"W) after the outer weather layer was removed, shortly before sampling. The sampling location is the second layer from the top of the ash, which is the uppermost coarse layer.

The selected allanite grains are predominantly anhedral to subhedral. Grains

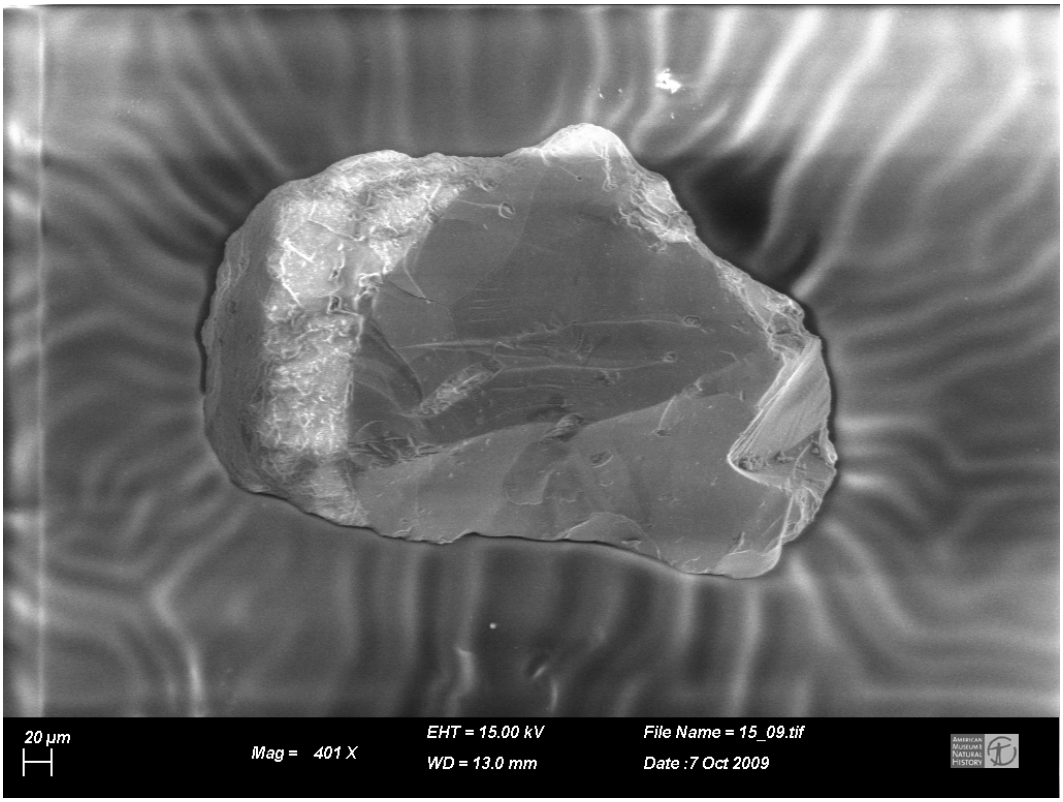

Figure 4.2: SEM image of a representative allanite grain from this study showing characteristic volcanic glass adhered to the anhedral crystal.

are also quite fragile: pressure applied with picking forceps causes grains to shatter and/or spall off adhering glass. From these observations we infer a high degree of physical preservation of the original crystal form for the grains we selected for analysis.

We analyzed a small number of grains using the American Museum of Natural History ESEM-EDX facility to ensure accurate identification of allanite. One of the eight studied grains, which in hindsight had an unusually elongate morphology, was amphibole. The seven remaining grains shared a highly unusual qualitative chemical composition, rich in Y, Th, and REE and characteristic of allanite (Figure 4.3). The presence of the thorium peak was encouraging, as the detection limit for

this technique is on the order of 1000 ppm.

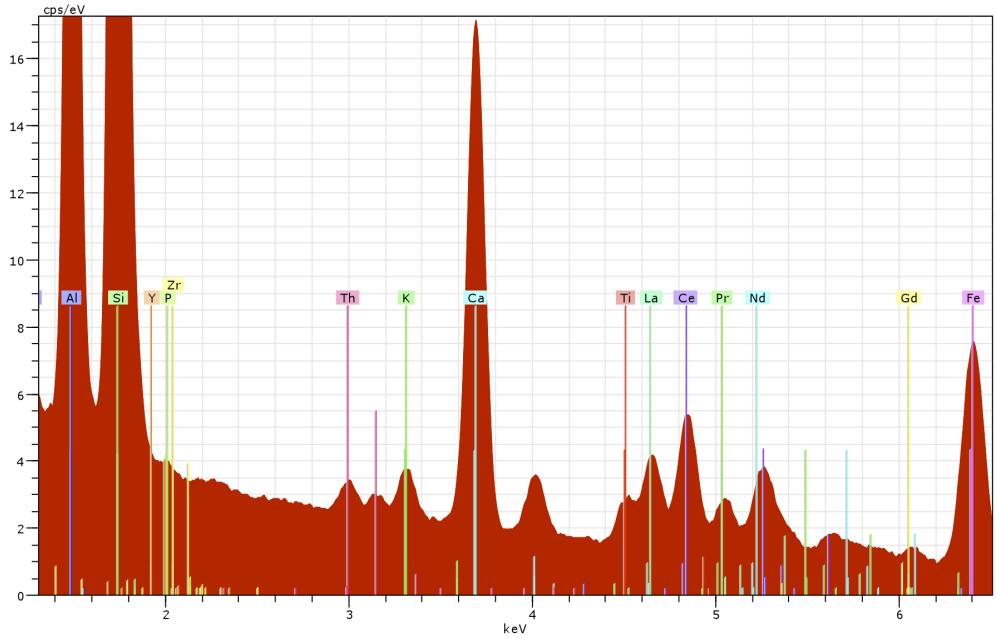

Figure 4.3: Example ESEM-EDX spectrum of allanite from Ash 15. This method was not calibrated for quantitative analysis, but the detection limit is on the order of 1000 ppm. Numerous REEs, as well as Th and Y, are visible in the spectrum of this REE epidote-group mineral, which resembles the allanite-(La) endmember (Orlandi and Pasero, 2006).

4.3.2 (U–Th)/He Analysis

We chose grains for (U–Th)/He analysis from the set of allanites analyzed by EDX and from similar grains from the same mineral separate. We encapsulated grains in HF-leached platinum tubes and then laser degassed them for ^{4}He measurement by isotope dilution (House and Farley, 2000). After degassing we removed samples from the tubes into PTFE microvials, where we dissolved them in concentrated 2:1 HF:HNO_3, dried them, and then brought them up in HNO_3. An accurately measured small aliquot of each solution was taken from each sample, diluted due to the large thorium concentrations, and then measured for thorium and uranium

by isotope dilution on a quadrupole ICP-MS with a collision cell to remove PtAr isobars in the U and Th mass spectrum. The analytical precision on these techniques yields formal (U–Th)/He age uncertainties of < 2%.

Thorium isotope ratios were measured on a separate aliquot of several solutions using routine multicollector ICP-MS methods (e.g., Robinson et al., 2005). Procedural blanks were 300–600 pmol/g for U and 200–2500 pmol/g for Th. The analytical precision for each analysis was < 0.5% and the standard deviation of the population thorium isotope ratio was 3%.

(U–Th)/He age determinations are typically made assuming that the uranium series daughters are in secular equilibrium. For samples that have undergone recent chemical fractionation (like Ash 15) this assumption is not likely to be valid. In such samples it is necessary to consider disequilibrium of ^{230}Th in the radium series (^{238}U-^{206}Pb) decay chain (Farley, Kohn, et al., 2002). Given the very high Th/U in allanite we expect it to crystallize with a large ^{230}Th excess. Indeed the dated allanites had Th/U ratios of up to ~200 compared to 3.05 ± 0.082 (1σ) for shards of glass in the ash that we assume represent the magmatic source of the allanite. Such strong chemical fractionation of uranium from thorium implies a large excess (>50 fold) in the initial ^{230}Th/^{238}U activity ratio. ^{226}Ra ($t_{1/2}$ = 1,601 a) disequilibrium may also occur, but its effect on the age is likely to be small due to the short half-life of this isotope. The actinium series (^{235}U-^{207}Pb) decay chain has one intermediate daughter with a significant lifetime (^{231}Pa, $t_{1/2}$ = 32,760 a). Because ^{235}U is ~138 times less abundant than ^{238}U, we expect the effect of this disequilibrium to be

much less important than ^{230}Th. The thorium series (^{232}Th-^{208}Pb) decay chain has no long-lived intermediate daughters. Radium and protactinium disequilibria are unlikely to affect the reported ages outside of error and so we ignore them here. The contribution of ^{147}Sm is also ignored——allanite typically contains about 3000 ppm Sm (e.g., Chesner and Ettlinger 1989; McFarlane and McCulloch 2007, an amount which would contribute ~0.2% extra helium to crystals with actinide concentrations as high as those in the Ash 15 allanites.

Accounting for excess ^{230}Th separately results in the following ingrowth equation:

$$^{4}\text{He} = 8\ ^{238}\text{U}\ (\exp[\lambda_{238}t] - 1) + 7(^{238}U/137.88)(\exp[\lambda_{235}t] - 1) + 6^{232}\text{Th}\left[\frac{^{230}\text{Th} - ^{230}\text{Th}_{\text{supp}}}{^{232}\text{Th}}(\exp[\lambda_{230}t] - 1) + (\exp[\lambda_{232}t] - 1)\right] \quad (1)$$

where ^{4}He, ^{238}U, ^{232}Th, and ^{230}Th are the current number of atoms of each isotope, $^{230}\text{Th}_{\text{supp}}$ is the supported ^{230}Th assuming secular equilibrium with ^{238}U, λ_i is the decay constant of isotope i in decays per years, and t is time in years.

To solve this equation we measured ^{230}Th/^{232}Th directly on five allanite grains and use the population ^{230}Th/^{232}Th ratio to calculate a ^{230}Th concentration for each grain based on the single-grain ^{232}Th measurements. The ^{230}Th excess was calculated by subtracting ^{230}Th supported by the decay of ^{238}U from the following equation:

$$^{230}\text{Th}_{\text{supp}} = \frac{\lambda_{238}}{\lambda_{230}}{}^{238}\text{U} \quad (2)$$

The choice of using the population average or single grain isotope ratio for each

of the five grains analyzed for ^{230}Th does not affect their ages within 1σ analytical error. These measurements also allowed us to calculate ^{230}Th excess disequilibrium ages for each of the five grains selected for ^{230}Th analysis.

As with all (U–Th)/He measurements on small grains, a correction must be applied for the ejection of energetic alpha particles from the crystal (Farley, Wolf, et al., 1996), but this correction is small and imparts only minor uncertainty for crystals as large as the allanite grains in this study. As described above, we believe that the anhedral allanite grains we analyzed were not broken during sampling. Our reasoning does not exclude the possibility that grains were euhedral in the magma chamber and attained their current form during a violent eruption. However, potential abrasion during the eruptive event at zero helium retention is irrelevant for the alpha ejection correction.

Alpha ejection corrections were calculated according to the technique proposed by Farley, Wolf, et al. (1996) using Equation 3.

$$F_T = 1 - S / 4 \cdot A / V \quad (3)$$

where F_T is the fraction of the total helium retained, S is the average stopping distance of the alpha particles in allanite, A is the surface area of the crystal, and V is the volume of the crystal. Surface area and volume were calculated as though the crystals are scalene ellipsoids, using the following equations.

$$V= (4/3) \cdot \pi \cdot a \cdot b \cdot c \quad (4)$$

where a, b, and c are the three orthogonal axes measured for each crystal using

an optical microscope. For surface area,

$$A = 4\pi \frac{a^p b^p + a^p c^p + b^p c^p}{3}^{(1/2)} \quad (5)$$

where p=1.6075 (Michon, 2011). This approximation is perfectly accurate for a sphere and is always accurate to within 1.061%. Errors in measurement and the geometric model are likely larger than errors associated with this mathematical approximation.

The value of S = 20.1 μm (the average stopping distance of alpha particles in allanite) was obtained using SRIM (Ziegler et al., 1985) with the alpha particle energy set to the average of alpha particles in the thorium series and radium series beginning with ^{230}Th, the composition of the crystal defined as the IMA endmember allanite-(La), and the density set to 3.93 g/cm^3 (Orlandi and Pasero, 2006). While Ash 15 allanite is actually allanite-(Ce), with a La/Ce ratio slightly less than one (Figure 4.3), the REE composition of allanite-(La) more closely matches that of Ash 15 allanite than other reported endmembers. The density chosen is high within the range reported for allanite, and slight variations in composition and density do not change the calculated helium ages outside analytical error.

Results of the α ejection computations are shown in Table 4.1. Almost all grains have F_T values of ~0.9, i.e., only about 10% of the alpha particles have been ejected.

4.3.3 ^{230}Th ages of Ash 15 allanite

We measured five specimens of glass to obtain an initial Th/U ratio of the allanite host magma of 3.05 ± 0.082 (1σ SD), which we assume to be in secular

equilibrium, as observed in glasses in the Mono Craters (Taddeucci et al., 1968; Pickett and Murrell, 1997). This allowed us to use the ^{230}Th excess for each allanite analyzed for thorium isotopes to calculate a disequilibrium age according to the following set of equations.

First, Equation 2 is used to calculate the amount of 230Th supported by ^{238}U at secular equilibrium. This value, along with the ^{230}Th concentration derived as described in Equation 1, is used to calculate the "excess" ^{230}Th:

$$^{230}\mathrm{Th}_{\mathrm{excess}} = ^{230}\mathrm{Th} - ^{230}\mathrm{Th}_{\mathrm{supp}} \tag{6}$$

After this calculation, the age is calculated using a standard age equation (Equation 8) for ^{238}Th-^{230}Th disequilibrium, with the initial ^{230}Th excess calculated according to Equation 7. Equation 7 assumes that ^{232}Th and ^{230}Th are fractionated into the allanite to to the same degree relative to ^{238}U, and makes use of the fact that the Th/U ratio is effectively constant over the time period of interest due to the very high ^{232}Th/^{230}Th ratio and long half life of ^{232}Th.

$$^{230}\mathrm{Th}_{\mathrm{excess}} = \frac{\frac{\mathrm{Th}}{\mathrm{U}}_{\mathrm{allanite}}}{\frac{\mathrm{Th}}{\mathrm{U}}_{\mathrm{glass}}}{}^{230}\mathrm{Th}_{\mathrm{supp}} \tag{7}$$

$$\mathrm{Age} = \frac{-1}{\lambda_{230}} \ln\left[\frac{^{230}\mathrm{Th}_{\mathrm{excess}}}{^{230}\mathrm{Th}^{\mathrm{initial}}_{\mathrm{excess}}}\right] \tag{8}$$

We report individual disequilibrium age errors of 10%, which exceeds analytical precisions of $< 2\%$ on U and Th and $\sim 3\%$ on ^{232}Th/^{230}Th and reflects the distribution and small size of the age population. The difference between the ^{230}Th crystallization age and the (U–Th)/He eruption age is the magma residence time of the crystal.

4.4 Results

4.4.1 Ash 15 eruption age

We analyzed 18 allanite grains for (U–Th)/He and five of these for ^{230}Th. The (U–Th)/He analyses yielded a mean age of 38.7 ± 1.2 ka (2 SE). (U–Th)/He data are summarized in Table 4.1. The ^{230}Th contribution is not a correction—it is the actual contribution of the parent obtained by measuring ^{232}Th/^{230}Th ratios for a subset of the allanite—so it is included in the calculated ages. The reported age is the apparent age after correction for alpha ejection.

Of the twenty grains selected for dating, one shattered after helium analysis, two gave no helium signal and were likely amphibole rather than allanite, and one (grain 4) gave an anomalously old helium age (3.5σ outlier). Relative to its calculated mass (by visual measurement of grain dimensions) and its measured mass (by microbalance), which are in good agreement, the anomalously old grain produced a typical concentration of helium but low uranium and thorium, so we suspect that part of this grain was lost during transfer between the helium and the uranium-thorium analyses, probably during removal from the platinum tube. We removed this age from population calculations; inclusion increases the central tendency of the age population by just over 1000 years and more than doubles the standard deviation.

4.4.2 Allanite magma residence time

Four grains measured for ^{230}Th excess had Th/U ratios ranging from 144 to 193 and a population average ^{232}Th/^{230}Th ratio of 323000 ± 10000 (2σ SD). The calculated ^{230}Th excess ages form a population with an age of 66.0 ± 3.3 ka (2σ SD).

Disequilibrium data are summarized in Table 4.2. One grain gave an anomalous Th/U ratio and anomalous Th and U concentrations during thorium isotope analysis, suggesting an error in sample dissolution or dilution, so we discard this result even though the thorium isotope ratio was consistent with the other grains. The calculated supported ^{230}Th for each grain is two orders of magnitude lower than the initial ^{230}Th excess. The ^{230}Th excess in each crystal has declined by between 45% and 47% relative to the initial value we predict from the long-lived Th and U isotopes in the coexisting glass, indicating excellent agreement among replicates and decay for approximately one half-life of ^{230}Th.

A fortuitous byproduct of the need to measure ^{230}Th is that we can calculate the residence time in the magma for the allanite crystals. To make this calculation, we assume that, while helium behaves as an open system in the magma chamber, the uranium-thorium system is closed in allanite after crystallization. Other researchers have argued that this is a reasonable assumption for other minerals (e.g., Reid, Coath, et al. 1997; Scheibner et al. 2008) based on diffusion measurements of U and Th that demonstrate geologically insignificant diffusion rates in silicate minerals (Cherniak et al., 1997; Cherniak, 2010), and Vazquez and Reid (2004) demonstrated that allanite in a rhyolitic magma retains U and Th and that the ^{238}U-^{230}Th system records crystallization within the magma chamber. While U and Th transport may occur in highly radiation-damaged crystals (Geisler et al., 2002), this is only a concern for samples much older than the allanite in this study. The difference between the disequilibrium age and the (U–Th)/He age suggests a magmatic crystal

residence time of about 30 ka for Ash 15 allanite (Figure 4.4), which is consistent with short residence times observed for this phase in rhyolitic domes of the nearby Coso volcanic field (Simon, Vazquez, et al., 2009).

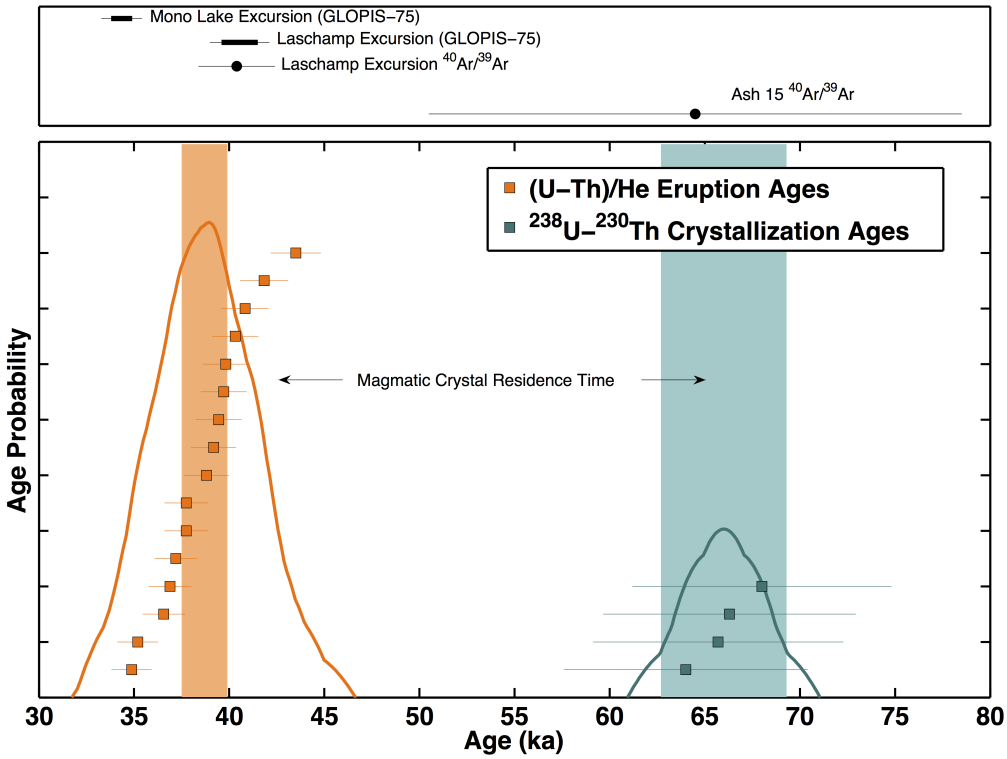

Figure 4.4: (U–Th)/He eruption ages and ^{238}U-^{230}Th crystallization ages for the allanite grains from Wilson Creek Formation Ash 15. The global paleomagnetic record dates for the Mono Lake Excursion and the Laschamp Excursion (GLOPIS-75; Laj et al. 2004) and the volcanic ^{40}Ar/^{39}Ar sanidine date for the Laschamp Excursion (40.4 ka; Guillou et al. 2004) are shown along with the mean age of sanidine from Ash 15 (Kent et al., 2002) and the ~30 ka magmatic crystal residence time implied by the (U–Th)/He and ^{238}U-^{230}Th ages. The lightly shaded boxes represent the mean age and reported error for each age population.

The fact that the disequilibrium age is older than the (U–Th)/He age underscores that they record different phenomena: the disequilibrium age corresponds with the time elapsed since the crystal grew in the magma chamber, while the (U–Th)/He age indicates elapsed time since He accumulation began, i.e., upon eruption and

cooling.

4.5 Discussion and Conclusions

The (U–Th)/He depositional age of 38.7 ± 1.2 ka obtained on Ash 15 allanite provides a good constraint on the age of the geomagnetic excursion bisected by the ash. Our result is consistent with both the Zimmerman, Hemming, Kent, et al. (2006) age model that pins Ash 15 at 39.8 ka, and with the age of the Laschamp at its type locality, 40.4 ± 2 ka (Guillou et al., 2004). Ash 15 is located about 20 cm (~1 ka) above the paleointensity minimum (Zimmerman, Hemming, Kent, et al., 2006), so the implied age of the excursion is even closer to the Laschamp type locality than the Ash 15 allanite age. With the addition of this new age constraint the Mono Lake Excursion at its type locality shares a similar structure, timescale, and age with the Laschamp. Since only one excursion is recorded in the Wilson Creek Formation, it seems most parsimonious to conclude that the Ash 15 excursion is indeed a record of the Laschamp. Ironically, the so-called Mono Lake Event observed in marine records (Laj et al., 2004) is apparently either absent or only weakly expressed in Mono Lake sediments.

Alternative techniques have yielded unreliable ages due to difficulties with the radiocarbon system and a dispersed and apparently unreasonable old $^{40}Ar/^{39}Ar$ sanidine population (Kent et al., 2002; Zimmerman, Hemming, Kent, et al., 2006; Cassata et al., 2010). While the challenges of radiocarbon dating in exotic and contaminated systems near the upper age limit of the radiocarbon system are well recognized (e.g., Pigati et al. 2007), the failure of the $^{40}Ar/^{39}Ar$ sanidine method

is more difficult to explain. The problem in the case of WCF Ash 15 is apparently either "excess argon," a poorly understood phenomenon, or simply inheritance of older sanidine from the country rock. While we emphasize that it may be a coincidence, the central tendency of our ^{230}Th excess ages, 66.0 ± 3.3 ka, overlaps with that of the ^{40}Ar/^{39}Ar sanidine population, 64.5 ± 13 ka (Kent et al., 2002). If sanidine crystallized around the same time as allanite, the ^{40}Ar/^{39}Ar sanidine ages may represent retention of argon in sanidine in the magma chamber. This finding potentially supports recent evidence of argon retention in minerals in a magma chamber by Hora et al. (2010), although in a mineral that these authors found to be devoid of pre-eruptive argon. This discrepancy may indicate different pre-eruptive P-T conditions in this magmatic system, a difference in magmatic argon pressure, or simply the greater sensitivity of the (U–Th)/He system to detecting excess argon in sanidine.

The calculated ^{230}Th excess ages form a population with an age of 66.0 ± 3.3 ka (2σ SD). Given the eruption age of 38.7 ± 1.2 ka, this suggests a magma residence time for these allanites of slightly less than 30 ka. In addition to the small sample size, we note that the apparent frequency of eruptions in this system may restrict the distribution of crystallization ages in a given ash. The ability to calculate a crystal residence time on the basis of a (U–Th)/He age and a ^{238}Th-^{230}Th crystallization age for the same mineral complements other methods that provide a measure of crystal residence times (Reid, Coath, et al., 1997; Brown and Fletcher, 1999; Reid and Coath, 2000; Miller and Wooden, 2004; Simon, Renne, et al., 2008). Combining

(U–Th)/He dating and ^{238}U-^{230}Th disequilibrium dating on single crystals of the same mineral is especially valuable for crystal residence time calculations in young magmatic systems for which U-Pb dating is not feasible but in which other methods are most likely to achieve the sensitivity necessary to detect residence times of less than 100 kyr.

Acknowledgements

We thank Gary Hemming and Guleed Ali for help with sampling and logistics, Lindsey Hedges and Adam Subhas for help with chemistry and analysis, and Becky Rudolph for assistance with the SEM. This research was supported by the Columbia Climate Center and the Comer Foundation, and by the National Science Foundation through a Graduate Research Fellowship to S. E. Cox.

Methods Note: Allanite Dissolution

The mineral allanite dissolves readily in boiling acid. After laser degassing, samples were removed from platinum tubes and placed in PTFE microvials for dissolution. We used a 2:1 mixture of concentrated reagent-grade HF:HNO_3 to dissolve the minerals on a hot plate set to ~150°C. Allanite went into solution almost immediately. We boiled the solution until dry, at which point a yellow oxide deposit remained in the bottom of the vial. We brought this deposit up in concentrated ultra high purity HNO_3 and briefly heated on a ~80°C hot plate to ensure complete dissolution. Solutions were then diluted to a 5% HNO_3 with Milli-Q ultrapure water for spiking and dilution.

References

Aciego, S., B. Kennedy, D. DePaolo, J. Christensen, and I. Hutcheon (2003). "U–Th/He age of phenocrystic garnet from the 79 AD eruption of Mt. Vesuvius". In: *Earth and Planetary Science Letters* 219, pp. 209–219.

Benson, L., J. Burdett, S. Lund, and M. Kashgarian (1997). "Nearly synchronous climate change in the Northern Hemisphere during the last glacial termination". In: *Nature*.

Benson, L., D. Currey, R. Dorn, K. Lajoie, C. Oviatt, S. Robinson, G. Smith, and S. Stine (1990). "Chronology of expansion and contraction of four great Basin lake systems during the past 35,000 years". In: *Palaeogeography, Palaeoclimatology, Palaeoecology* 78.3-4, pp. 241–286.

Benson, L., J. Liddicoat, J. Smoot, A. Sarna-Wojcicki, R. Negrini, and S. Lund (2003). "Age of the Mono Lake excursion and associated tephra". In: *Quaternary Science Reviews* 22.2-4, pp. 135–140.

Benson, L., S. Lund, J. Burdett, M. Kashgarian, T. Rose, J. Smoot, and M. Schwartz (1998). "Correlation of Late-Pleistocene Lake-Level Oscillations in Mono Lake, California, with North Atlantic Climate Events". In: *Quaternary Research* 49, pp. 1–10.

Brown, S. and I. Fletcher (1999). "SHRIMP U-Pb dating of the preeruption growth history of zircons from the 340 ka Whakamaru Ignimbrite, New Zealand: Evidence for> 250 ky magma residence times". In: *Geology* 27.11, pp. 1035–1038.

Bursik, M. and A. Gillespie (1993). "Late Pleistocene Glaciation of Mono Basin, California". In: *Quaternary Research* 39.1, pp. 24–35.

Cassata, W. S., B. S. Singer, J. C. Liddicoat, and R. S. Coe (2010). "Reconciling discrepant chronologies for the geomagnetic excursion in the Mono Basin, California: Insights from new 40Ar/39Ar dating experiments and a revised relative paleointensity correlation". In: *Quaternary Geochronology* 5.5, pp. 533–543.

Chen, Y., P. Smith, N. Evensen, D. York, and K. Lajoie (1996). "The Edge of Time: Dating Young Volcanic Ash Layers with the 40Ar-39Ar Laser Probe". In: *Science* 274.5290, pp. 1176–1178.

Cherniak, D. J., J. M. Hanchar, and E. B. Watson (1997). "Diffusion of tetravalent cations in zircon". In: *Contributions to Mineralogy and Petrology* 127.4, pp. 383–390.

Cherniak, D. (2010). "Diffusion in minerals: an overview of published experimental diffusion data". In: *Reviews in Mineralogy and . . .*

Chesner, C. A. and A. D. Ettlinger (1989). "Composition of volcanic allanite from the Toba Tuffs, Sumatra, Indonesia". In: *American Mineralogist* 74.7-8, pp. 750–758.

Coe, R., B. Singer, M. Pringle, and X. Zhao (2004). "Matuyama–Brunhes reversal and Kamikatsura event on Maui: paleomagnetic directions, 40Ar/39Ar ages and implications". In: *Earth and Planetary Science Letters* 222.2, pp. 667–684.

Crowley, J. L., B. Schoene, and S. A. Bowring (2007). "U-Pb dating of zircon in the Bishop Tuff at the millennial scale". In: *Geology* 35.12, p. 1123.

Davidson, J., J. Hassanzadeh, R. Berzins, D. F. Stockli, B. Bashukooh, B. Turrin, and A. Pandamouz (2004). "The geology of Damavand volcano, Alborz Mountains, northern Iran". In: *Geological Society of America Bulletin* 116.1, p. 16.

Davis, O. (1999). "Pollen Analysis of a Late-Glacial and Holocene Sediment Core from Mono Lake, Mono County, California". In: *Quaternary Research* 52, pp. 243–249.

Denham, C. R. and A. Cox (1971). "Evidence that the Laschamp polarity event did not occur 13300–30400 years ago". In: *Earth and Planetary Science Letters* 13.1, pp. 181–190.

Farley, K., B. Kohn, and B. Pillans (2002). "The effects of secular disequilibrium on (U–Th)/He systematics and dating of Quaternary volcanic zircon and apatite". In: *Earth and Planetary Science Letters* 201.1, pp. 117–125.

Farley, K., R. Wolf, and L. Silver (1996). "The effects of long alpha-stopping distances on (U-Th)/He ages". In: *Geochimica et Cosmochimica Acta* 60.21, pp. 4223–4229.

Geisler, T., R. Pidgeon, W. Van Bronswijk, and R. Kurtz (2002). "Transport of uranium, thorium, and lead in metamict zircon under low-temperature hydrothermal conditions". In: *Chemical Geology* 191, pp. 141–154.

Graham, N. E. and M. K. Hughes (2007). "Reconstructing the Mediaeval low stands of Mono Lake, Sierra Nevada, California, USA". In: *The Holocene* 17.8, pp. 1197–1210.

Guillou, H., B. S. Singer, C. Laj, C. Kissel, S. Scaillet, and B. R. Jicha (2004). "On the age of the Laschamp geomagnetic excursion". In: *Earth and Planetary Science Letters* 227.3-4, pp. 331–343.

Hora, J., B. Singer, B. Jicha, and B. Beard (2010). "Volcanic biotite-sanidine 40Ar/39Ar age discordances reflect Ar partitioning and pre-eruption closure in biotite". In: . . .

House, M. and K. Farley (2000). "Helium chronometry of apatite and titanite using Nd-YAG laser heating". In: *Earth and Planetary Science Letters* 183.3-4, pp. 365–368.

Kent, D. V., S. R. Hemming, and B. D. Turrin (2002). "Laschamp Excursion at Mono Lake?" In: *Earth and Planetary Science Letters* 197.3-4, pp. 151–164.

Laj, C., C. Kissel, and J. Beer (2004). “High resolution global paleointensity stack since 75 kyr (GLOPIS-75) calibrated to absolute values”. In: *Geophysical monograph* 145, pp. 255–265.

Lajoie, K. (1968). “Late Quaternary stratigraphy and geologic history of Mono Basin, Eastern California”. PhD thesis. University of California.

Liddicoat, J. and R. Coe (1979). “Mono Lake geomagnetic excursion”. In: *Journal of Geophysical Research* 84, pp. 261–271.

Lund, S. P., J. C. Liddicoat, K. R. Lajoie, T. L. Henyey, and S. W. Robinson (1988). “Paleomagnetic evidence for long-term (10 4year) Memory and periodic behavior in the Earth’s core dynamo process”. In: *Geophysical Research Letters* 15.10, pp. 1101–1104.

McFarlane, C. and M. T. McCulloch (2007). “Coupling of in-situ Sm–Nd systematics and U–Pb dating of monazite and allanite with applications to crustal evolution studies”. In: *Chemical Geology* 245, pp. 45–60.

Miller, J. and J. Wooden (2004). “Residence, resorption and recycling of zircons in Devils Kitchen rhyolite, Coso volcanic field, California”. In: *Journal of Petrology*.

Orlandi, P. and M. Pasero (2006). “Allanite-(La) from Buca della Vena mine, Apuan Alps, Italy, an epidote-group mineral”. In: *Canadian mineralogist*.

Pickett, D. A. and M. T. Murrell (1997). “Observations of 231Pa/235U disequilibrium in volcanic rocks”. In: *Earth and Planetary Science Letters* 148, pp. 259–271.

Pigati, J., J. Quade, J. Wilson, A. Jull, and N. Lifton (2007). “Development of low-background vacuum extraction and graphitization systems for 14C dating of old (40-60 ka) samples”. In: *Quaternary international*.

Reheis, M., S. Stine, and A. Sarna-Wojcicki (2002). “Drainage reversals in Mono Basin during the late Pliocene and Pleistocene”. In: *Geological Society of . . .*

Reid, M. R., C. D. Coath, T. Mark Harrison, and K. D. McKeegan (1997). “Prolonged residence times for the youngest rhyolites associated with Long Valley Caldera:230Th—238U ion microprobe dating of young zircons”. In: *Earth and Planetary Science Letters* 150.1-2, pp. 27–39.

Reid, M. and C. Coath (2000). “In situ U-Pb ages of zircons from the Bishop Tuff: No evidence for long crystal residence times”. In: *Geology* 28.5, pp. 443–446.

Russell, I. (1889). *Russell: Quaternary history of Mono Valley, California - Google Scholar*.

Scheibner, B., A. Heumann, and G. Wörner (2008). “Crustal residence times of explosive phonolite magmas: U-Th ages of magmatic Ca-Garnets of Mt. Somma-Vesuvius (Italy)”. In: *Earth and Planetary Science Letters*.

Schmitt, A., M. Grove, T. Harrison, and O. Lovera (2003). “The Geysers - Cobb Mountain Magma System, California (Part 1): U-Pb zircon ages of volcanic rocks, conditions of zircon crystallization and magma residence times”. In: *Geochimica et Cosmochimica Acta* 67, pp. 3423–3442.

Simon, J., P. Renne, and R. Mundil (2008). “Implications of pre-eruptive magmatic histories of zircons for U–Pb geochronology of silicic extrusions”. In: *Earth and Planetary Science Letters* 266, pp. 182–194.

Simon, J. I., J. A. Vazquez, P. R. Renne, A. K. Schmitt, C. R. Bacon, and M. R. Reid (2009). “Accessory mineral U–Th–Pb ages and 40Ar/39Ar eruption chronology, and their bearing on rhyolitic magma evolution in the Pleistocene Coso volcanic field, California”. In: *Contributions to Mineralogy and Petrology* 158.4, pp. 421–446.

Stine, S. (1990a). “Late holocene fluctuations of Mono Lake, eastern California”. In: *Palaeogeography, Palaeoclimatology, Palaeoecology* 78.3-4, pp. 333–381.

— (1990b). “Past climate at Mono Lake”. In: *Nature* 345.6274, pp. 391–391.

Stine, S. (1987). “Mono Lake; the past 4,000 years”. PhD thesis. University of California, Berkeley.

Taddeucci, A., W. S. Broecker, and D. L. Thurber (1968). “230Th dating of volcanic rocks”. In: *Earth and Planetary Science Letters* 3, pp. 338–342.

Vazquez, J. A. and M. R. Reid (2004). “Probing the accumulation history of the voluminous Toba magma.” In: *Science* 305.5686, pp. 991–994.

Wolf, R. (1997). “The Development of the (U-Th)/He Thermochronometer”. PhD thesis. California Institute of Technology.

Zimmerman, S. R. H., S. R. Hemming, N. G. Hemming, P. B. Tomascak, and C. Pearl (2011). “High-resolution chemostratigraphic record of late Pleistocene lake-level variability, Mono Lake, California”. In: *Geological Society of America Bulletin* 123.11-12, pp. 2320–2334.

Zimmerman, S., S. Hemming, D. Kent, and S. Searle (2006). “Revised chronology for late Pleistocene Mono Lake sediments based on paleointensity correlation to the global reference curve”. In: *Earth and Planetary Science Letters* 252.1-2, pp. 94–106.

Zimmerman, S. R. H., C. Pearl, S. R. Hemming, K. Tamulonis, N. G. Hemming, and S. Y. Searle (2011). “Freshwater control of ice-rafted debris in the last glacial period at Mono Lake, California, USA”. In: *Quaternary Research* 76.2, pp. 264–271.

Grain	Calculated mass mg	U ppm	Th ppm	^{232}Th/^{230}Th subpopulation average	He 10^{-10} moles/g	FT (α-ejection correction)		Helium Age (ka)	Helium Age error (ka)
1	0.056	46	6600	323000	5.06	0.89		39.8	1.2
2	0.153	42	6600	323000	5.23	0.93		39.2	1.2
3	0.092	43	7700	323000	5.35	0.91		35.2	1.1
4	0.058	32	5700	323000	6.49	0.90			
5	0.062	48	7700	323000	5.66	0.90		37.7	1.1
6	0.101	39	7400	323000	5.78	0.91		39.5	1.2
7	0.099	65	12000	323000	8.02	0.91		34.9	1.1
8	0.043	25	4900	323000	3.80	0.89		40.3	1.2
9	0.057	52	9900	323000	7.10	0.90		36.9	1.1
10	0.061	45	7500	323000	6.20	0.90		41.8	1.3
11	0.050	43	7800	323000	5.49	0.89		36.6	1.1
12	0.043	60	9600	323000	8.09	0.88		43.5	1.3
13	0.039	39	6700	323000	5.27	0.88		40.8	1.2
14	0.043	42	7400	323000	5.67	0.89		39.7	1.2
15	0.075	25	4800	323000	3.47	0.90		37.2	1.1
16	0.041	44	6800	323000	4.94	0.88		37.7	1.1
17	0.060	33	5700	323000	4.30	0.90		38.8	1.2
							Average	38.7	
							SE (2σ)	1.2	

Table 4.1: (U–Th)/He data and calculated helium eruption ages. The ^{232}Th/^{230}Th shown is the average of n=4 grains selected from the main population for thorium isotopic analysis. The 2σ standard deviation of the four samples was 3%.

Grain	$^{230}Th/^{238}U$ activity ratio	$^{230}Th/^{238}U$ activity ratio error	$^{232}Th/^{238}U$ activity ratio	$^{232}Th/^{238}U$ activity ratio error		Diseq. Age (ka)	Diseq. Age error (ka)
1	38	0.11	65	0.10		65.7	6.6
8	35	0.14	61	0.14		68.0	6.8
11	34	0.094	59	0.083		66.3	6.6
13	34	0.13	58	0.11		64.0	6.4
					Average	66.0	
					SD (2σ)	3.3	

Table 4.2: ^{230}Th excess data and calculated disequilibrium crystallization ages.